UNIVERSITA' DEGLI STUDI DI NAPOLI

FEDERICO II

FACOLTA' DI SCIENZE MATEMATICHE, FISICHE E NATURALI

DOTTORATO DI RICERCA

IN

FISICA FONDAMENTALE ED APPLICATA

XXIII CICLO

Zhuoyi Huang

Galaxy Cluster Weak Lensing: Simulation and Detection

COORDINATORE

Prof. Raffaele Velotta

RELATORE   **CORRELATORE**

Prof. Massimo Capaccioli   **Dr. Mario Radovich**

Abstract

We investigated the detection of galaxy clusters with their weak gravitational lensing effect. Galaxy clusters are the most massive gravitationally bound systems in the Universe, and their abundance and evolution provide important information about the structure formation in the cosmological context. Weak gravitational lensing makes use of the distortion of the background galaxy images to probe the matter distribution of the clusters. In this work, we present three methods for the weak lensing study of galaxies clusters. We first developed a program ExAM, which automatically and efficiently masks image defects contaminating the shape measurement of galaxies. The output of the program can be used to remove the problematic detections of galaxy in the image. We then present a catalog-space simulation of cluster weak lensing, SHUFF, featuring the configurable intrinsic properties of galaxies, multiple triaxial cluster halos as lenses, and realizations of cosmological density perturbation field as a source of shear noise. It takes a catalog of unlensed galaxies, applies the multiple lens plane lensing effects, and outputs a lensed galaxies catalog, which can either be used to produce image of galaxies for the shape measurement calibration, or be taken as the input of cluster detection based on the galaxy ellipticities. We also developed a program for cluster detection, LENSFILTER, implementing the optimal filtering techniques suggested by Maturi et.al. (2004). We generalize the techniques for detection of specific clusters with configurable galaxies redshift distribution and noise properties. The filtering detection is first applied to the SHUFF simulation, for an investigation of limit of cluster detection with weak lensing, and further applied to the CFHTLS data with comparison to cluster detection from X-ray observations.

Contents

Chapter 1

Introduction

In this thesis work, we will investigate the detection of galaxy clusters with their weak gravitational lensing effect. Galaxy clusters are the most massive gravitationally bound systems in the Universe, and their abundance and evolution provide important information about the structure formation in the cosmological context. Weak gravitational lensing makes use of the distortion of the background galaxy images to probe the matter distribution of the clusters. As our investigation involves general background about cosmology, lensing theory, technical weak lensing methods like shape measurement and PSF correction, and weak lensing observation and data properties, in this chapter we introduce all these preliminaries which will be intensively used later.

1.1 Cosmological standard model

In this section, we will introduce the main aspects in standard cosmological model, *i.e.* the homogeneous and isotropic cosmological background. Our aim here is to cover the necessary materials that will be extensively used in the following sections, rather than to be complete in every detail. We refer the readers to excellent textbooks, such as Kolb & Turner (1990), Peacock (1999), Padmanabhan (1993), Peebles (1993), Liddle & Lyth (2000), Dodelson (2003), for more details about the theory of cosmology.

1.1.1 Homogeneous universe

In General relativity, the space-time is described as a four-dimensional manifold with its metric tensor $g_{\mu\nu}$ considered as a dynamical field. The dynamics of the metric tensor is governed by the *Einstein's field equations* (Einstein 1915), which relates the geometry of the space-time, Einstein tensor $G_{\mu\nu}$, to the matter contained in the space-time, the stress-energy tensor $T_{\mu\nu}$,

$$G_{\mu\nu} = \frac{8\pi G}{c^2} T_{\mu\nu} + \Lambda g_{\mu\nu} .\qquad(1.1)$$

Here Λ is called *cosmological constant*, and the last term proportional to the metric $g_{\mu\nu}$ was originally introduced by Einstein to balance the contraction due to the matter and allow for a static universe. However, cosmological observations in the last decades strongly suggest that a positive cosmological constant can be a candidate accounting for the current accelerating expansion of our universe.

There are two fundamental postulates in the standard cosmological background model,

1. *when averaged over sufficiently large scales, the observable properties of the Universe are isotropic, i.e. independent of direction;*

2. *our position in the Universe is by no means preferred to any other.*

If the Universe is isotropic for an observer at any point, it is also homogeneous. Thus the two assumptions above can be rephrased as, the Universe is spatially homogeneous and isotropic around every point. This is usually called generalized *cosmological principle*, and has been tested with various large scale observations such as Cosmic Background Radiation (hereafter CMB), faint galaxy distribution, etc.

In the four dimenional space-time, the interval $\mathrm{d}s$ between to events with coordinates $\mathrm{d}x^\mu$ is related to the metric tensor by $\mathrm{d}s^2 = g_{\mu\nu}\,\mathrm{d}x^\mu\,\mathrm{d}x^\nu$. From the cosmological principle, the line element of the metric, of our background universe can be directly formulated as,

$$\mathrm{d}s^2 = c^2\mathrm{d}t^2 - a^2(t)\big[\mathrm{d}\chi^2 + S_K^2(\chi)(\mathrm{d}\theta^2 + \sin^2\theta\mathrm{d}\varphi^2)\big] \ , \tag{1.2}$$

where t is the cosmic time, $a(t)$ is the scale factor normalized to $a(t_0) = 1$ and χ is the comoving radial coordinate and θ, φ is the angular coordinates on the unit sphere. Thus the metric element $g_{00} = c^2$ so that for a comoving observer at fixed spatial coordinate, the cosmic time is just the proper time measured by the observer. Due to the isotropy, the space-time component of the metric vanishes $g_{0i} = 0^*$, which prefers no specific direction in the space-time. Isotropy also requires that the sptial metric g_{ij} is only a function of time, $a(t)$, and follows spherical sptial symmetry with respect to any point as origin. However, the principle allows for a curved spatial hypersurface in four dimensional space-time. Thus the radial function $S_K(\chi)$ is either trigonometric, linear or hyperbolic function of w, correponding to a sptially closed $(K > 0)$, flat $(K = 0)$ and open $(K < 0)$ universe, respectively,

$$S_K(\chi) = \begin{cases} \sin(\sqrt{K}\,\chi)/\sqrt{K} & (K > 0) \\ \chi & (K = 0) \\ \sinh(\sqrt{-K}\,\chi)/\sqrt{-K} & (K < 0) \end{cases} . \tag{1.3}$$

Note that the comoving radius χ, radial function $S_K(\chi)$ and the curvature of space K have the dimension of the length. The metric in Eq.(1.2), which reveals the homogeneity and isotropy of the background universe, is often called *Robertson-Walker* (hereafter RW) *metric*.

The evolution of the RW metric and the spatial curvature is determined by the Einstein field equations. The symmetry in the metric implies that the stress-energy tensor $T_{\mu\nu}$ is in the form of that of a homogenous perfect fluid, with density $\rho(t)$ and pressure $p(t)$ as functions of time only. Substituting the RW metric into the Einstein field equations of a perfect fluid gives two independent dynamic equations for the evolution of the scale factor $a(t)$,

$$\left(\frac{\dot{a}}{a}\right)^2 = \frac{8\pi G}{3}\rho - \frac{Kc^2}{a^2} + \frac{\Lambda}{3} \tag{1.4}$$

$$\frac{\ddot{a}}{a} = -\frac{4}{3}\pi G\left(\rho + \frac{3p}{c^2}\right) + \frac{\Lambda}{3} \ . \tag{1.5}$$

The first equation, Eq.(1.4), which relates the expansion of the universe to the energy density of the components it contains, is called *Friedmann's equation* (Friedman 1922, 1924). While the second equation Eq.(1.5), is analogous to Newtonian gravity except that in General Relativity the pressure acts for a source of gravity and the cosmological constant acts as a replusive source. These two differential equations for $a(t)$ of first and second order can be combined to yield the *adiabatic equation*,

$$\frac{\mathrm{d}}{\mathrm{d}t}\left(a^3\rho c^2\right) + p\frac{\mathrm{d}}{\mathrm{d}t}a^3 = 0 \ , \tag{1.6}$$

---

*In this chapter, the greek indices run over 0,1,2,3 and Latin indices run over spatial indices 1,2,3.

which states the change of internal energy equals the pressure work, *i.e.* the first law of thermodynamics in the cosmological context. The RW metric with the scale factor following the Friedmann's equation Eq.(1.4) and adiabatic equation Eq.(1.6) is further called *Friedmann-Lemaître-Robertson-Walker* (hereafter FLRW) *metric*.

Given the Friedmann equation Eq.(1.4), the universe can either constract ($\dot{a} < 0$) or expand ($\dot{a} > 0$). Thus a light emitted at t_e with wavelength λ_e will be observed at t_0 with wavelength λ_0, *i.e.* blue- or redshifted according to the amount that Universe contracted or expanded,

$$\frac{\lambda_0}{\lambda_e} = \frac{a(t_0)}{a(t_e)} := 1 + z \, , \tag{1.7}$$

where in the last step, the *redshift z* is defined. The observations of the redshift of distance galaxies, performed by Edwin Hubble during the 1920s, confirmed the expansion of the universe. The recession velocity of the galaxy is found to be proportional to its proper distance $v = H(t_0)D$, which is called teh *Hubble's law*, and the *Hubble parameter* is defined as,

$$H(t) := \frac{\dot{a}}{a} \, . \tag{1.8}$$

The value of Hubble parameter today $H_0 = H(t_0)$ is called the *Hubble constant*, which is commonly expressed as $H_0 = 100 \, h$ km s^{-1} Mpc^{-1}, with dimensionless parameter h; current observations give the best estimate of $h \approx 0.714$ (Komatsu et al. 2010). As the Hubble parameter has the dimension of inverse of time, H_0^{-1} is called *Hubble time* and it gives the time scale of the expansion of the universe, $H_0^{-1} \approx 9.78 \, h^{-1}$ Gyr. The length that light travels during this time scale is called *Hubble radius*, $c/H_0 \approx 3 \, h^{-1}$ Gpc.

The evolution of the scale factor $a(t)$ and thus the Hubble parameter $H(t)$, can not be decided with the Friedmann equation and adiabatic equation alone, as it also involves the time dependence of the density $\rho(t)$ and pressure $p(t)$ of the matter components in the universe. The additional independent equation comes from the relation between the density and pressure $p = p(\rho)$ of the matter component, which is called *equation of state* (hereafter EoS). In general, the matter components may not have a simple form of EoS. However, during the most period in its history, the Universe is dominated by the matter components whose EoS take the limiting form $p = p(\rho)$.

In the non-relativistic limit, the thermal velocity of the matter particle is far less than the speed of light, *i.e.* $p \ll \rho c^2$, so that the pressure is negligible in the adiabatic equation. With $p = 0$, the density of this kind of matter component evloves as $\rho_m \propto a^{-3}$, and is called 'dust', or simply 'matter'. Note its mass density decrease as the proper volume expands $\rho_m \propto V^{-1}$.

In the relativistic limit, the thermal velocity of the matter particle is as the same order to the speed of light, or is exact c for massless particle like photon, and the EoS reads $p = \rho/3$. Then its density can be shown to evolve as $\rho_r \propto a^{-4}$, and it is called 'radiation'. The number density of the particles decreases in the same way as for dust particles, while additionally its energy decreases as a^{-1} due to the redshift effect as the proper volume expands.

If the mean density of matter and radiation today are ρ_m^0 and ρ_r^0, respectively, then we have their evolution as a function of redshift,

$$\rho_m(z) = \rho_m^0 (1+z)^3 \, , \tag{1.9}$$
$$\rho_r(z) = \rho_r^0 (1+z)^4 \, . \tag{1.10}$$

With the EoS found for matter and radiation, and with the definition of Hubble parameter, the Friedmann equation Eq.(1.4) can be written as

$$H^2(z) = \frac{8\pi G}{3} \left[\rho_m^0 (1+z)^3 + \rho_r^0 (1+z)^4 \right] - Kc^2 (1+z)^2 + \frac{\Lambda}{3} \, . \tag{1.11}$$

For convenience, the density of matter and radiation are usually expressed as a fraction of the *critical density* of the universe ρ_{cr}^0,

$$\rho_{cr}^0 = \frac{3H_0^2}{8\pi G} \approx 1.88 \times 10^{-29} h^2 \mathrm{g\,cm}^{-3} \approx 2.77 \times 10^{11} h^2 M_\odot \mathrm{Mpc}^{-3} \,, \tag{1.12}$$

and the dimensionless density of matter and radiation measured today read,

$$\Omega_m^0 = \frac{\rho_m^0}{\rho_{cr}^0} \,, \quad \Omega_r^0 = \frac{\rho_r^0}{\rho_{cr}^0} \,. \tag{1.13}$$

Analogously, we can define the dimensionless "density" contributed by the curvature of the universe, and by the cosmological parameter as,

$$\Omega_K^0 = -\frac{Kc^2}{H_0^2} \,, \quad \Omega_\Lambda^0 = \frac{\Lambda}{3H_0^2} \,. \tag{1.14}$$

Finally the Friedmann equation Eq.(1.11) takes the form $H(z) = H_0 \, E(z)$, where

$$E(z) = \sqrt{\Omega_r^0(1+z)^4 + \Omega_m^0(1+z)^3 + \Omega_K^0(1+z)^2 + \Omega_\Lambda^0} \,. \tag{1.15}$$

Since $H(z=0) = H_0$, and $E(z=0) = 1$, we find the density of the curvature is related to the others by $\Omega_K^0 = 1 - \Omega_r^0 - \Omega_m^0 - \Omega_\Lambda^0 = 1 - \Omega_{tot}^0$. Therefore, the spatially closed, flat and open universe corresponds to the total density of all the components is over-critical ($\Omega_{tot}^0 > 1$), critical ($\Omega_{tot}^0 = 1$) or sub-critical ($\Omega_{tot}^0 < 1$), respectively. The current (dimensionless) density of all the components are well constrained by the recent observations. In this work, we adopt the following cosmological parameters $\Omega_m^0 = 0.262$, $\Omega_\Lambda^0 = 0.738$, and $\Omega_k^0 = 0$ from WMAP7 results (Komatsu et al. 2010).

With the expansion of the Universe described, now we are ready to define the time, distance and volume in the Universe. We use redshift z to indicate the time when the Universe is $1/(1+z)$ smaller than the one today ($z = 1$).

The *proper time* measured by a observer between the Universe is at the redshift z_2 and at z_1 ($z_1 < z_2$) is,

$$t_{prop}(z_1, z_2) = \int_{z_2}^{z_1} \mathrm{d}t = \int_{z_2}^{z_1} \frac{\mathrm{d}a(z)}{a(z)H(z)} = \frac{1}{H_0} \int_{z_1}^{z_2} \frac{\mathrm{d}z}{(1+z)E(z)} \,. \tag{1.16}$$

Hence the *proper distance* that a light ray travels from a source at z_2 to the observer at z_1 is,

$$D_{prop}(z_1, z_2) = c\,t_{prop} = \frac{c}{H_0} \int_{z_1}^{z_2} \frac{\mathrm{d}z}{(1+z)E(z)} \,. \tag{1.17}$$

The *comoving distance* is the distance that a light ray travels, on the same spatial hypersurface $t = t_0$, between a source at z_2 to the observer at z_1. Since light follows geodesics $\mathrm{d}s = 0$, $\mathrm{d}\chi = c\,\mathrm{d}t/a$, and hence,

$$D_{com}(z_1, z_2) = \chi(z_1, z_2) = \int_{z_2}^{z_1} \mathrm{d}\chi = \frac{c}{H_0} \int_{z_1}^{z_2} \frac{\mathrm{d}z}{E(z)} = \frac{c}{H_0} w(z_1, z_2) \,, \tag{1.18}$$

where in the last step we defined the dimensionless distance $w(z_1, z_2)$.

The *angular diameter distance* is the distance between the source at z_2 with proper physical cross section $\mathrm{d}\mathbf{A}$ and the observer for whom the source subtends a solid angle $\mathrm{d}\boldsymbol{\omega}$. Hence,

$$D_{ang}(z_1, z_2) = \left(\frac{\mathrm{d}\mathbf{A}}{\mathrm{d}\boldsymbol{\omega}}\right)^2 = \frac{1}{1+z_2}\frac{c}{H_0} f_K\big[w(z_1, z_2)\big] \,, \tag{1.19}$$

where we the defined dimensionless geometric function $f_K(w)$ as a function of dimensionless distance w as,

$$f_K(w) = \begin{cases} \sin(\sqrt{-\Omega_K}\,w)/\sqrt{-\Omega_K} & (K > 0) \\ w & (K = 0) \\ \sinh(\sqrt{\Omega_K}\,w)/\sqrt{\Omega_K} & (K < 0) \end{cases} . \qquad (1.20)$$

and it is related to the geometric function $S_K(\chi)$ in the RW metric Eq.(1.2) by $S_K(\chi) = (c/H_0)f_K(w)$.

The *luminosity distance* is the distance between the source at z_2 with intrinsic luminosity L and the observer at z_1 who receives the flux S. Taking into account the redshift of photons by a_1/a_2, the streching of arrival time by a_1/a_2 and the dilution of area by $(a_1/a_2)^2$, it reads,

$$D_{\text{lum}}(z_1, z_2) = \sqrt{\frac{L}{4\pi S}} = \frac{1 + z_2}{(1 + z_1)^2} \frac{c}{H_0} f_K\big[w(z_1, z_2)\big] . \qquad (1.21)$$

Finally, for an observer at redshift $z = 0$, the proper and comoving volume elements in a redshift slice between z and $z + \mathrm{d}z$, with solid angle $\boldsymbol{\omega}$, can be calculated as,

$$\mathrm{d}V_{\text{prop}} = \boldsymbol{\omega}\, D_{\text{ang}}^2(z)\, \mathrm{d}D_{\text{prop}} , \qquad (1.22)$$

$$\mathrm{d}V_{\text{com}} = (1 + z)^3\, \mathrm{d}V_{\text{prop}} . \qquad (1.23)$$

Thus, the proper number density of sources (*e.g.* galaxies or dark matter halos of galaxy cluster) is $n = \mathrm{d}N/\mathrm{d}V_{\text{prop}}$.

1.2 Properties of gravitational lenses

According to the General Relativity, light propagation follows the null-geodesics of the space-time metrics. The presence of mass distribution perturbs the metrics hence deflects the light trajectory. This deflection results in the distortion of the images of distant galaxies, which gives the possibility to study the mass distribution of different objects across the universe via such distortion, or *gravitational lensing* effect.

To understand the physics of gravitational lensing, let us start from the progragation of two thin light bundles in the universe. From a local observer, two light rays are emitted into directions, slightly different in a transverse angle $\boldsymbol{\theta}$, lying in the plane perpendicular to the light propagation ($|\boldsymbol{\theta}| \ll 1$).

In a homogeneous universe, the comoving separation vector $\mathbf{x}$ at comoving distance w from the observer is related to transverse separation angle $\boldsymbol{\theta}$ by $\mathbf{x}(\boldsymbol{\theta}, w) = f(w)\,\boldsymbol{\theta}$, which is just definition of *comoving* angular diameter distance $f(w)$. This relation is also the solution to the equation of geodesic deviation in comoving space,

$$\frac{\mathrm{d}^2\mathbf{x}}{\mathrm{d}\,w^2} + K\,\mathbf{x} = 0 , \qquad (1.24)$$

where $K = (c/H_0)^{-2}(\Omega_{\text{m}}^0 + \Omega_{\Lambda}^0 - 1)$ is the spatial curvature of the universe (cf. the case distinction of $f(w)$ in curvature K).

When the small inhomogeneity is present, assuming its peculiar Newtonian potential small ($\Phi \ll c^2$) and localized, the perturbed metric can be approximated by first post-Newtonian order of the Minkowski metric,

$$ds^2 = \left(1 + \frac{2\Phi}{c^2}\right) c^2 dt^2 + \left(1 - \frac{2\Phi}{c^2}\right) a^2(t)[dw^2 + f^2(w)d\omega^2] , \qquad (1.25)$$

and the *rhs* of the comoving separation evolution equation (1.24) contains a term due to the difference in the transverse comoving gradient of peculiar potential between the light rays,

$$\frac{\mathrm{d}^2\mathbf{x}}{\mathrm{d}\,w^2} + K\,\mathbf{x} = -\frac{2}{c^2}\Delta\left(\nabla_{\mathbf{x}}^{\perp}\Phi[\mathbf{x}(\boldsymbol{\theta},w),w]\right)\ . \tag{1.26}$$

The solution to Eq.(1.26) can be obtained with the method of Green's function (Schneider et al. 1998),

$$\mathbf{x}(\boldsymbol{\theta},w) = f(w)\,\boldsymbol{\theta} - \frac{2}{c^2}\int_0^w \mathrm{d}w' f(w-w')\Delta\left(\nabla_{\mathbf{x}}^{\perp}\Phi[\mathbf{x}(\boldsymbol{\theta},w'),w']\right)\ . \tag{1.27}$$

Since without the local perturbation potential Φ, the original position of the galaxy would be seen at $\boldsymbol{\beta} = \mathbf{x}/f(w)$, dividing Eq.(1.27) by $f(w)$ on both sides just reveals the mapping between the (perturbed) image position $\boldsymbol{\theta}$ and (unperturbed) source position $\boldsymbol{\beta}$,

$$\boldsymbol{\beta} = \boldsymbol{\theta} - \frac{2}{c^2}\int_0^w \mathrm{d}w'\frac{f(w-w')}{f(w)}\Delta\left(\nabla_{\mathbf{x}}^{\perp}\Phi[\mathbf{x}(\boldsymbol{\theta},w'),w']\right) = \boldsymbol{\theta} - \boldsymbol{\alpha}\ , \tag{1.28}$$

where in the last step *deflection angle* $\boldsymbol{\alpha}$ is defined. Eq.(1.28) is called *lens equation*. Upto the linear order, which we will always assume throughout this thesis, the mapping between image and source can be described by a *Jacobian matrix* $\mathbf{A}(\boldsymbol{\theta},w) := \partial\boldsymbol{\beta}/\partial\boldsymbol{\theta}$, which is related to perturbation potential by solving the lens equation (1.28),

$$A_{ij}(\boldsymbol{\theta},w) = \delta_{ij} - \frac{2}{c^2}\int_0^w \mathrm{d}w'\frac{f(w-w')f(w')}{f(w)}\,\Phi_{,ij}(\boldsymbol{\theta},w')\ , \tag{1.29}$$

where $i,j = 1,2$ refer to two angular bases $\{\theta_1,\theta_2\}$ lying in the perpendicular plane located at the observer[†].

To illustrate how the Jacobian matrix (1.29) fully describes the distortion of an image, as far as local linearized mapping $\boldsymbol{\beta} = \mathbf{A}\,\boldsymbol{\theta}$ is concerned, we can define a two dimensional *deflection potential* ψ as,

$$\psi(\boldsymbol{\theta},w) = \frac{2}{c^2}\int_0^w \mathrm{d}w'\frac{f(w-w')}{f(w)f(w')}\,\Phi(\boldsymbol{\theta},w')\ , \tag{1.31}$$

and further define the *convergence* κ and the complex *shear* $\gamma = |\gamma|\mathrm{e}^{2\mathrm{i}\varphi} = \gamma_1 + \mathrm{i}\gamma_2$ as,

$$\kappa = \frac{1}{2}(\psi_{,11} + \psi_{,22}) \tag{1.32}$$

$$\gamma = \frac{1}{2}(\psi_{,11} - \psi_{,22}) + \mathrm{i}\,\psi_{,12}\ . \tag{1.33}$$

Note in two dimensional case, Newtonian equation $\nabla_{\boldsymbol{\theta}}\psi = \boldsymbol{\alpha}$ and Poisson equation $\nabla_{\boldsymbol{\theta}}^2\psi = 2\kappa$ also hold[‡]. Thus, the Jacobian matrix can be simplified into a sum of a diagonal part, which

---

[†]Here the Born approximation of A_{ij} is applied, with $A_{ij} = \delta_{ij}$ and $\mathbf{x} = f(w)\,\boldsymbol{\theta}$, to the *rhs* of the followng the exact equation,

$$A_{ij}(\boldsymbol{\theta},w) = \delta_{ij} - \frac{2}{c^2}\int_0^w \mathrm{d}w'\frac{f(w-w')f(w')}{f(w)}\,\Phi_{,ik}[\mathbf{x}(\boldsymbol{\theta},w'),w']A_{kj}(\boldsymbol{\theta},w'). \tag{1.30}$$

[‡]Unless otherwisely specified, 2d gradient, wrt to angular bases, is denoted with $\nabla_{\boldsymbol{\theta}}$, while the 3d case denoted with $\nabla_{\mathbf{x}}$ or $\nabla_{\mathbf{r}}$, corresponding to differentiation wrt comoving, or proper coordinates, respectively.

changes the size of an image according to κ, and a traceless symmetric part, which changes the shape according to γ,

$$\mathbf{A}(\boldsymbol{\theta}) = \left(\delta_{ij} - \psi_{,ij}\right) = (1 - \kappa) - \begin{pmatrix} \gamma_1 & \gamma_2 \\ \gamma_2 & -\gamma_1 \end{pmatrix} = (1 - \kappa) \begin{pmatrix} 1 - g_1 & -g_2 \\ -g_2 & 1 + g_1 \end{pmatrix} . \tag{1.34}$$

In the last step, the *reduced shear* $g = \gamma/(1 - \kappa)$ is defined. The eigenvalue of the Jacobian matrix is $\lambda_{1,2} = (1 - \kappa) \pm |\gamma| = (1 - \kappa)(1 \pm |g|)$, which shows that, when $\kappa \neq 0$, a circular object will be enlarged by the inverse of the trace $(\mathrm{Tr}\,\mathbf{A})^{-1} = (\lambda_1 + \lambda_2)^{-1} = (1 - \kappa)^{-1}$, while when $|\gamma| \neq 0$, such an object will be stretched into a ellipse, with the ratio of eigenvalues λ_1/λ_2 as axial ratio (Fig.1.1).
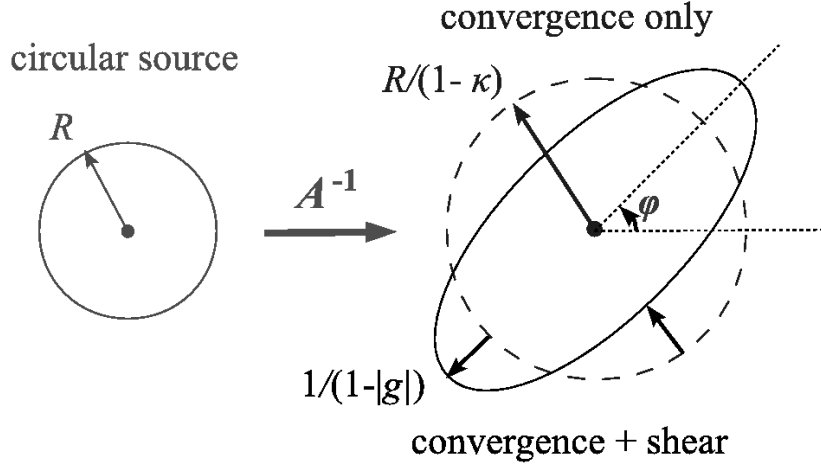

Figure 1.1: The illustration of convergence and shear, applied on a circular object with radius R. The convergence amplifies the circle with radius $R/(1 - \kappa)$, while the shear further streches the circle into an ellipse, with major and minor axis $R/[(1 - \kappa)(1 \pm |g|)]$, and the angle of streching φ.

Since the light deflection in gravitational lensing involves no emission or absorption of photons, the surface brightness of the source object is conserved,

$$I(\boldsymbol{\theta}) = I^{\mathrm{s}}[\boldsymbol{\beta}(\boldsymbol{\theta})] . \tag{1.35}$$

Therefore the ratio between the integrated flux of the image and source, is just the ratio of the subtended solid angle between them, which is called *magnification* μ,

$$\mu = \frac{\omega}{\omega^{\mathrm{s}}} = \frac{1}{\det \mathbf{A}} = \frac{1}{\lambda_1 \lambda_2} = \frac{1}{(1 - \kappa)^2 - |\gamma|^2} = \frac{1}{(1 - \kappa)^2(1 - |g|^2)} . \tag{1.36}$$

Note that $\det \mathbf{A} = 0$ corresponds to infinity magnification, which defines the *critical curves* on the lens plane, where $\kappa(\boldsymbol{\theta}) = 1$ or $|g|(\boldsymbol{\theta}) = 1$. The mapping of these curves on the source plane are called *caustics*. Close and within the critical curves, where $\kappa \geq 1$, substantially distorted multiple images, *e.g.* giant luminous arcs, can be seen, when the sources are closed to the caustics, and the effect is called the *strong lensing*. However, this topic will not be covered by this thesis, and in the following, we will always work with the *weak lensing* regions where $\kappa < 1$ and $|g| < 1$.

We have seen that, given the mass distribution of different objects in the universe, from their 3d gravitational potential, we can construct the 2d deflection potential, and derive all the lens

properties. In the following subsections, we will study different objects as lens, especially the isolated distributed objects, such as galaxy clusters, and the continueous distributed matters, the cosmological density perturbation.

1.2.1   Isolated mass distribution

Massive objects such as stars, galaxies, clusters of galaxies,and black holes, can serve as isolated gravitational lenses. For these objects, if the density profile $\rho(\mathbf{r})$ is known, its peculiar potential can be derived from 3d Poisson equation,

$$\nabla_{\mathbf{r}}^2 \Phi = 4\pi G \rho(\mathbf{r}) \; . \tag{1.37}$$

Apply the 2d Laplacian $\nabla_{\boldsymbol{\theta}}$ to deflection potential in Eq.(1.31), the convergence can be related to the density profile of the lens by,

$$
\begin{aligned}
\kappa \;=\; \frac{1}{2}\nabla_{\boldsymbol{\theta}}^2 \psi \;&=\; \frac{1}{c^2}\int_0^w \mathrm{d}w' \frac{f(w-w')f(w')}{f(w)} a^2(w')\nabla_{\mathbf{r}}^2 \Phi \\
&=\; \frac{4\pi G}{c^2}\frac{D_{\mathrm{ds}}D_{\mathrm{d}}}{D_{\mathrm{s}}}\int_0^{r(w)} \mathrm{d}r\, \rho(r) \; ,
\end{aligned}
\tag{1.38}
$$

where D_{d} , D_{ds} , D_{s} are the *proper* angular diameter distance between observer-lens, lens-source and observer-lens, respectively, and r is the light-of-sight proper distance[§]. If we define the *surface mass density* $\Sigma(\boldsymbol{\theta}) = \int \rho(\boldsymbol{\theta}, r)\mathrm{d}r$ and *critical surface mass density* Σ_{cr} as,

$$\Sigma_{\mathrm{cr}} = \frac{c^2}{4\pi G}\frac{1}{D_{\mathrm{d}}}\frac{D_{\mathrm{s}}}{D_{\mathrm{ds}}} \approx 1.66 \times 10^{15}\frac{M_{\odot}}{\mathrm{Mpc}^2}\left(\frac{D_{\mathrm{d}}}{1\mathrm{Gpc}}\right)^{-1}\left(\frac{D_{\mathrm{s}}}{D_{\mathrm{ds}}}\right) \; , \tag{1.39}$$

the dimensionless convergence κ is the projected mass density scaled by critical surface density $\kappa(\boldsymbol{\theta}) = \Sigma(\boldsymbol{\theta})/\Sigma_{\mathrm{cr}}$. Since Σ_{cr} is related to the angular diameter distances, or "lensing configuration", between the observer, lens and source, we can see that, for a certain configuration, the lens itself should be massive enough to produce significant lensing effect. On the other hand, for the same lens at certain distance D_{d}, the further the source is, the stronger the lensing effect (as $D_{\mathrm{ds}}/D_{\mathrm{s}}$ increases), while for the same sources at certain distance D_{s}, the lensing effect is optimized only for lenses located at certain distance (that maximize $D_{\mathrm{d}} \cdot D_{\mathrm{ds}}$). These simple inferences are not trivial, as for a survey with lensing effects, the former suggests a survey deep enough to enhance the sampling of stronger lensing signals from background galaxies, while the latter suggests that with certain depth of survey, only lenses at certain redshift ranges are prefered to be detected. We will come back to these consideration later.

For convenience of specifying the lensing strength, we can define the *lens efficiency* as a function of source redshift,

$$Z(z_{\mathrm{s}}) = C\frac{D_{\mathrm{ds}}(z_{\mathrm{d}}, z_{\mathrm{s}})}{D_{\mathrm{s}}(z_{\mathrm{s}})}H(z - z_{\mathrm{d}}), \tag{1.40}$$

where $H(z)$ is the Heaviside function which gives zero weight to the sources in front of the lens, and normalization factor C can be chosen such that $Z(z_{\mathrm{s}} \to \infty) = 1$. Hence in case when the sources are distributed in redshift with $n_z(z)$, rather than located on a single source plane, we can replace $D_{\mathrm{ds}}/D_{\mathrm{s}}$ in definition of critical surface mass density Eq.(1.39), with a weighted average $\langle D_{\mathrm{ds}}/D_{\mathrm{s}}\rangle$, *i.e.*

$$\langle Z \rangle = \int_{z_{\mathrm{d}}}^{z_{\mathrm{h}}} \mathrm{d}z'\, n_z(z')Z(z) \; , \tag{1.41}$$

[§]Note in the second step, $\partial_{x_3}^2$ along light-of-sight is added to form a 3d proper Laplacian, since its contribution along the integration averages out.

where $z_{\rm h}$ is the redshift of the horizon. Note from Eq.(1.41) that an effective source redshift $z_{\rm s}^{\rm eff}$ can be found, so that $Z(z_{\rm s}^{\rm eff}) = \langle Z(z) \rangle$.

From Eq.(1.38), we can derive analytically the lens properties for some simple spherical symmetric lens models from their density profiles $\rho(r)$. For non-symmetric lenses, such as triaxial-ellipsoid models with some density profile, the lens properties like convergence and shear generally can not be derived in an analytical form, and numerical method is usually involved, as will be shown in Chapter 3.

We first take a few lines to illustrate some properties of axial-symmetric lens. In the polar coordinate (θ, φ), with origin at the lens center, we have the 2d Gauss theorem,

$$\int_0^\theta {\rm d}^2\theta \nabla \cdot \nabla \psi = \theta \oint {\rm d}\varphi \, \nabla \psi \cdot \mathbf{n} \, , \tag{1.42}$$

with integration on the *lhs* over a circle with radius θ, and $\mathbf{n}$ the outward nomral vector on the circle. Note $\nabla^2 \psi = 2\kappa$ and $\nabla \psi \cdot \mathbf{n} = \psi_{,\theta} = \alpha_{\rm r}$. and Eq.(1.42) is just the integral version of $2\kappa = \nabla \cdot \alpha_{\rm r}$, where $\alpha_{\rm r}$ is the radial deflection angle. Since the potential is axial-symmetric $\psi = \psi(\theta)$, Eq.(1.42) simplifies to

$$4\pi \int {\rm d}\theta' \, \theta' \, \kappa(\theta') = 2\pi\theta \, \partial_\theta \psi(\theta) \, . \tag{1.43}$$

If we define mean surface density within the circle θ as $\bar\kappa(\theta) = (2/\theta^2) \int_0^\theta {\rm d}\theta'\theta'\kappa(\theta')$, and note that for points on axis $\varphi = 0$, $\psi_{,\theta\theta} = \kappa + \gamma_1 = \kappa - \gamma_{\rm t}$, we find Eq.(1.43) and its derivative *w.r.t.* to θ just give

$$\alpha_{\rm r}(\theta) = \theta \, \bar\kappa(\theta) \, , \tag{1.44}$$
$$\gamma_{\rm t}(\theta) = \bar\kappa(\theta) - \kappa(\theta) \, . \tag{1.45}$$

Note this result is independent of φ, hence valid for all points in (θ, φ), as expected from the axial symmetry of the lens. Finally, we note from the determinant of Jacobian matrix,

$$\det \mathbf{A} = (1-\kappa)^2 - |\gamma|^2 = (1-\bar\kappa)(1+\bar\kappa-2\kappa) \, , \tag{1.46}$$

that for axial-symmetric lenses, there are two types of critical curves corresponding to $\bar\kappa = 1$ (*tangential critical curves*), and $1 + \bar\kappa = 2\kappa$ (*radial critical curves*).

- The singular isothermal sphere model (hereafter SIS), is a virialized self-gravitating system of "particles", such as galaxies in the cluster, or stars in a galaxy, with 1d velocity dispersion σ_v in Maxwellian distribution at all radii. The density profile of SIS, mass and the project surface mass density read

$$\rho(r) = \frac{\sigma_v^2}{2\pi G} \frac{1}{r^2} \, , \quad M(r) = \frac{2\sigma_v^2}{G} r \, , \quad \Sigma(\theta) = \frac{\sigma_v^2}{2\,GD_{\rm d}} \frac{1}{\theta} \, . \tag{1.47}$$

  With Eq.(1.38) and Eq.(1.45) the following lens properties can be derived,

$$\kappa(\theta) = \gamma_{\rm t}(\theta) = \frac{\theta_{\rm E}}{2\theta} \, , \quad \bar\kappa(\theta) = \frac{\theta_{\rm E}}{\theta} \, , \quad \alpha_{\rm r}(\theta) = \theta_{\rm E} \, , \tag{1.48}$$

  where $\theta_{\rm E}$ is the Einstein radius,

$$\theta_{\rm E} = 4\pi \frac{D_{\rm ds}}{D_{\rm s}} \left(\frac{\sigma_v}{c}\right)^2 \approx 1.4'' \left(\frac{\sigma_v}{220\,{\rm km/s}}\right)^2 \left(\frac{D_{\rm ds}}{D_{\rm s}}\right) \, . \tag{1.49}$$

Note for the SIS, the deflection angle is the same, equal to the Einstein radius θ_{E}, for all positions except the center, and the circle with Einstein radius around the center defines the tangential critical curve. There is no radial critical curve for the SIS.

The SIS density profile has only one parameter, the velocity dispersion σ_v, independent of the cosmological context, and is commonly used in modeling the virialized objects, such as galaxies or galaxy clusters. But it diverges as $\rho \sim r^{-2}$ when $r \to 0$, and its total mass diverges when $r \to \infty$.

- Navarro-Frenk-White model (hereafter NFW), is a typical density profile for dark matter halos, as a fitting result from the numerical simulations (Navarro et al. 1997). The NFW density profile is parameterized as

$$\rho(r) = \frac{\delta_c \rho_c(z)}{(r/r_s)(1 + r/r_s)^2} \, , \tag{1.50}$$

with two parameters, the density contrast δ_c and the scale radius r_s. Compared to SIS, NFW profile is shallower near the center $\rho \sim r^{-1}$, and steeper in the outer regions $\rho \sim r^{-3}$, with the transition scale r_s. The virial radius r_{200} of the NFW halo is defined to be the radius within which the mean density of the halo is 200 times of the density of the background universe $\rho_c(z) = 3H^2(z)/(8\pi G)$, and the ratio of virial radius and scale radius is defined as concentration parameter $c = r_{200}/r_s$. With the definition of r_{200}, the density contrast δ_c is a function of concentration parameter,

$$\delta_c = \frac{200}{3} \frac{c^3}{\ln(1+c) - c/(1+c)} \, , \tag{1.51}$$

so that when integrated, the profile yields the virial mass $M_{200} = 200\rho_c(z)4\pi r_{200}^3/3$. So practically speaking, the model is implicitly parameterized with (M_{200}, c), rather than (δ_c, r_s).

The lens properties of a NFW halo is discussed in many works (e.g. Bartelmann 1996; Golse & Kneib 2002), and the convergence $\kappa(x)$ and tangential shear $\gamma_{\mathrm{t}}(x)$ are calculated to be,

$$\kappa(x) = \kappa_s f(x)/2, \quad \bar{\kappa}(x) = \kappa_s h(x), \quad \gamma_{\mathrm{t}} = \kappa_s [h(x) - f(x)/2] \, , \tag{1.52}$$

where $x = R/r_{\mathrm{s}} = D_{\mathrm{d}}\theta/r_{\mathrm{s}}$, the characterisic convergence $\kappa_s = 4\, r_s\, \delta_c\, \rho_c/\Sigma_c$, and

$$f(x) = \begin{cases} \frac{1}{x^2-1}\left[1 - \frac{2}{\sqrt{1-x^2}}\operatorname{arctanh}\sqrt{\frac{1-x}{1+x}}\right] & x < 1 \\ \frac{1}{3} & x = 1 \\ \frac{1}{x^2-1}\left[1 - \frac{2}{\sqrt{x^2-1}}\arctan\sqrt{\frac{x-1}{1+x}}\right] & x > 1 \end{cases} \tag{1.53}$$

$$h(x) = \begin{cases} \frac{1}{x^2}\left[\ln(\frac{x}{2}) + \frac{2}{\sqrt{1-x^2}}\operatorname{arctanh}\sqrt{\frac{1-x}{1+x}}\right] & x < 1 \\ 1 + \ln(\frac{1}{2}) & x = 1 \\ \frac{1}{x^2}\left[\ln(\frac{x}{2}) + \frac{2}{\sqrt{x^2-1}}\arctan\sqrt{\frac{x-1}{1+x}}\right] & x > 1 \end{cases} \, . \tag{1.54}$$

Note the convergence and shear diverge logrithmically as $r \to 0$.

In order to properly fit the density profile with different simulations, the slope of orignal NFW model is generalized to

$$\rho(r) = \frac{\delta_c \rho_c}{(r/r_s)^\alpha (1 + r/r_s)^{3-\alpha}}, \quad (1 \le \alpha \le 1.5) \, . \tag{1.55}$$

But the convergence and shear can only be calculated numerically. In addition, the concentration parameter is found to depend on redshift and virial mass, so called mass-concentration relation. For example, the relation can be parameterized as,

$$c_{\text{vir}} = \frac{c_0}{1+z} \left(\frac{M_{\text{vir}}}{M_*(z=0)} \right)^\alpha \tag{1.56}$$

with $c \sim 10$, and $\alpha \sim -0.2$ (Bullock et al. 2001; Comerford & Natarajan 2007). Further variation is introduced, where the virial density contrast is chosen from a fitting formula, (Bryan & Norman 1998), instead of 200,

$$\Delta_{\text{vir}}(z) = \frac{18\pi^2 + 82x - 39x^2}{1+x}, \ . \tag{1.57}$$

where $x = \Omega_{\text{m}}^0(z) - 1$.

1.2.2 Continuous mass distribution

Besides the isolated massive objects as we mentioned in the last subsection, the cosmological density perturbation is another type of lens, which is continuously distributed across the universe and successively deflects the light from the distant galaxies, so called *cosmic shear*. The growth of density perturbations at different scale is described by the theory of structure formation given the cosmological model. Thus, the study of the cosmic shear reflects the properties of the large-scale structure in the cosmic matter field, and can be used to constrain the cosmology.

To formulate the cosmic shear, we assume that the density perturbations are localized, *i.e.* the scale of the peculiar potential of interest is much smaller than the curvature of the universe, and weak, *i.e.* the peculiar motion of particles due to the perturbation is much smaller than the speed of light, so that they can be described by Newtonian gravity, and follow the 3d Poisson equation in comoving coordinates,

$$\nabla_{\mathbf{x}}^2 \Phi = 4\pi G a^2 \bar{\rho}\, \delta \ , \tag{1.58}$$

where the density contrast δ is defined as $\rho = (1+\delta)\bar{\rho}$, and $\bar{\rho} = 3H^2/(8\pi G)$ is the mean density of the univese. In the matter dominated era, $\bar{\rho}(a) = \bar{\rho}_0\, \Omega_{\text{m}}^0\, a^{-3}$, so that the 3d Poisson reads,

$$\nabla_{\mathbf{x}}^2 \Phi = \frac{3H_0^2 \Omega_{\text{m}}^0}{2\,a} \delta \ . \tag{1.59}$$

With the peculiar potential related to the density contrast, as we did in Eq.(1.38) for isolated lens, we can apply a 2d Laplacian on Eq.(1.31) and obtain the integrated convergence for source at comoving distance w,

$$\kappa(\boldsymbol{\theta}, w) = \frac{3H_0^2 \Omega_{\text{m}}^0}{2\,c^2} \int_0^w \mathrm{d}w' \frac{f(w-w')f(w')}{f(w)} \frac{\delta(\boldsymbol{\theta}, w')}{a(w')} \ . \tag{1.60}$$

If the redshift distribution of source galaxies is $n_z(z)\,\mathrm{d}z = n_w(w)\,\mathrm{d}w$, the effective convergence can be obtained by integrating over the source distribution,

$$\begin{aligned} \kappa(\boldsymbol{\theta}) &= \int_0^{w_{\text{h}}} \mathrm{d}w\, n_w(w)\, \kappa(\boldsymbol{\theta}, w) \\ &= \frac{3H_0^2 \Omega_{\text{m}}^0}{2\,c^2} \int_0^{w_{\text{h}}} \mathrm{d}w\, g(w) f(w) \frac{\delta(\boldsymbol{\theta}, w)}{a(w)} \ , \end{aligned} \tag{1.61}$$

where w_{h} is the comoving horizon distance. In the last step of Eq.(1.61), the integral in Eq.(1.60) is re-arranged so that the weighting function $q(w)$ reads,

$$g(w) = \int_{w}^{w_{\mathrm{h}}} \mathrm{d}\, w' n_w(w') \frac{f(w-w')}{f(w')} \; , \tag{1.62}$$

which is, for the lens at comoving distance w, the lens efficiency $D_{\mathrm{ds}}/D_{\mathrm{s}}$ weighted over the *background* source redshift distribtion, in analogous to Eq.(1.41).

Since the density perturbation field $\delta(\mathbf{x})$ is a specific realization of a random field, the theory of structure formation can only give statistical properties of the field, rather than predict exactly what we see at different positions in our universe. Thus, cosmic shear can only be studied in a statistical approach, *i.e.* through the power spectrum of the density perturbations, the "lenses", and the correlation of the distortions of galaxies, the "sources".

To project the 3d density power spectrum to 2d, we can make use of the Limber's equation (Limber 1953), which states that, for a quantity $g(\boldsymbol{\theta})$ that is an integrated random density field $\delta(\boldsymbol{\theta}, w)$ through projection,

$$q(\boldsymbol{\theta}) = \int \mathrm{d}w' g(w') \delta(\boldsymbol{\theta}, w') \; , \tag{1.63}$$

the 2d correlation function between these two variables $q_1(\boldsymbol{\theta}_1)$ and $q_2(\boldsymbol{\theta}_2)$, with $\Delta\theta = |\boldsymbol{\theta}_1 - \boldsymbol{\theta}_2|$, can be related to the correlation function of the 3d random field by

$$\begin{aligned} C_{12}(\Delta\theta) &= \langle q_1(\boldsymbol{\theta}_1) q_2(\boldsymbol{\theta}_2) \rangle \\ &= \int \mathrm{d}w\, g_1(w) g_2(w) \int \mathrm{d}(\Delta w) C_{\delta\delta}(\sqrt{(f(w)\Delta\theta)^2 + (\Delta w)^2}, w) \; . \end{aligned} \tag{1.64}$$

An alternative form of Limber's equation is obtained in Fourier space (Kaiser 1992, 1998),

$$P_{12}(\ell) = \int \mathrm{d}w \frac{g_1(w) g_2(w)}{f^2(w)} P_{\delta}\left(\frac{\ell}{f(w)}, w\right) \; , \tag{1.65}$$

where $1/\ell$ is the angular scale of 2d power spectrum P_{12}, while $f(w)/\ell$ is the length scale of 3d power density spectrum P_{δ}.

A comparison between Eq.(1.61) and (1.65) directly yields the 2d power spectrum of cosmic shear convergence,

$$P_{\kappa,12}^{GG}(\ell) = \int_{0}^{w_{\mathrm{h}}} \mathrm{d}w \frac{W_1(w) W_2(w)}{f^2(w)} P_{\delta}(k(w), w) \; , \tag{1.66}$$

where $k(w) = \ell/f(w)$ and the weight function $W_i(w)$ is of the form,

$$W_i(w) = \frac{3 H_0^2 \Omega_{\mathrm{m}}^0}{2\, c^2} \frac{f(w)}{a(w)} \int_{w}^{w_{\mathrm{h}}} \mathrm{d}\, w' n_i(w') \frac{f(w-w')}{f(w')} \; , \tag{1.67}$$

in which $i = 1, 2$. The upper index GG in Eq.(1.66) stands for the correlation between gravitational and gravitational shear, to be distinguished from the intrinsic-intrinsic shear corrletion term II and cross correlation between them GI, which will be covered later.

1.3 Properties of the sources of lensing

Distant galaxies are the sources of gravitational lensing. In this section, we will take a brief look at the properties of these distance galaxies, their intrinsic shape, intrinsic alignment, redshift distribution, how to statistically estimate the lens properties from their shapes, and the practical shape measurement in the observation data.

1.3.1   Properties of source galaxies

Distance galaxies behind the foreground lenses would be ideal tracers of the gravitaional shear of lenses if they were intrinsicaly circular and located at infinity distance. However, in the real world, this is not the case.

Galaxies are distributed in the redshift, According to their type, the number density of galaxies can be derived from their luminosity function, evolving with redshift (Schechter et al. 1997; Efstathiou et al. 1988; Marzke et al. 1994a,b). Alternatively, without the specification in the type of galaxy, the redshift distribution of distant galaxies can also be described in the form derived from the fitting to observations (e.g. Smail et al. 1995),

$$p(z)z = \frac{\beta}{z_0^3 \, \Gamma(3/\beta)} \, z^2 \, \exp\left[-\left(\frac{z}{z_0}\right)^\beta\right] z \;, \tag{1.68}$$

in which the $\beta = 1.5$ and the median redshift of the distribution $z_m = 1.5 \, z_0$. The shear signal sampled from the galaxies with distribution, is different from that sampled from the galaxies at infinity distance, by a factor $\langle D_{\rm ds}/D_{\rm s}\rangle < 1$, averaged over the redshift distribution. Thus, the significance of lensing effect is limited by the depth of observation.

Besides, to the first order, galaxies are elliptical and randomly oriented. Their ellipticity $|\varepsilon| = \sqrt{\varepsilon_1^2 + \varepsilon_2^2}$ can be described by the axial ratio between the minor and major axes $r = b/a$ by,

$$|\varepsilon| = \frac{1-r}{1+r} \;. \tag{1.69}$$

The distribution of ε is found in good approximation to be described by a Gaussian function,

$$p_\varepsilon(\varepsilon_1, \varepsilon_2)\mathrm{d}\varepsilon_1\mathrm{d}\varepsilon_2 = \frac{\exp(-|\varepsilon|^2/\sigma_\varepsilon^2)}{\pi\sigma_\varepsilon^2\,[1 - \exp(-1/\sigma_\varepsilon^2)]} \, \mathrm{d}\varepsilon_1\mathrm{d}\varepsilon_2 \;, \tag{1.70}$$

with the intrinsic ellipticity dispersion $\sigma_\epsilon \approx 0.3$ (e.g. Miralda-Escude 1991b; Tyson & Seitzer 1988; Brainerd et al. 1996). The intrinsic ellipticity of galaxies introduces noise into the gravitational shear, which needs to be averaged out with large samples of galaxies.

Moreover, the intrinsic ellipticity of galaxies are found to be correlated with the underlying gravitational tidal field (Hirata & Seljak 2004), resulting an effect called intrinsic alignment (hereafter IA). In the linear model of IA, the intrinsic shear is defined as,

$$\gamma^I = -\frac{C_1}{4\pi G}(\nabla_x^2 - \nabla_y^2, 2\nabla_x\nabla_y)\Psi_P \tag{1.71}$$

where Ψ_P is the potential of primodial gravitational linear perturbation field, and is related to the potential at redshift z by $\Psi_P = \Psi(z)/\bar{D}$. Here $\bar{D}$ is the scaled growth factor $\bar{D} = (1+z)D(z)$, with

$$D(z) = \frac{5\Omega_m^0}{2}E(z)\int_z^\infty \frac{(1+z)\,\mathrm{d}z}{E(z)^3} \;. \tag{1.72}$$

Making use of the 3d Poisson equation in comoving space $\nabla^2\Psi(z) = 4\pi G\rho_m(z)\delta(z)a^2(z)$, the effective convergence for intrinsic shear reads,

$$\kappa_{\rm eff}^I(z) = -\frac{C_1}{4\pi G}\nabla^2\Psi_P = -\frac{C\bar{\rho}_0\,\Omega_m}{D(z)}\delta(z) \;. \tag{1.73}$$

where the intrinsic shear amplitude is found to be $C\bar{\rho}_0 \approx 0.0134$ (Joachimi & Schneider 2009; Bridle & King 2007). Note that the minus sign in equation above is due to the reason that in linear IA model, intrinsic shear stretchs galaxies radially towards the mass concentration, as a

result of gravitational tidal force. Analogously to the case of cosmic shear Eq.(1.66), one can derive the power spectra of intrinsic shear and the correlation between CS and IA as,

$$P_\ell^{II}(\alpha\beta) = \int_0^\infty \mathrm{d}\chi \, \frac{n_\alpha(\chi)\,n_\beta(\chi)}{f_K^2(\chi)} \, P_{\tilde\gamma}(k(\chi);\chi) \tag{1.74}$$

$$P_\ell^{GI}(\alpha\beta) = \int_0^\infty \mathrm{d}\chi \, \frac{W_\alpha(\chi)\,n_\beta(\chi) + n_\alpha(\chi)\,W_\beta(\chi)}{f_K^2(\chi)} \, P_{\delta\tilde\gamma}(k(\chi);\chi) \tag{1.75}$$

where the 3d power spectra $P_{\tilde\gamma}(k(\chi);\chi)$ and $P_{\delta\tilde\gamma}(k(\chi);\chi)$ is related to the density power spectra by,

$$P_{\tilde\gamma^I}(k,z) = \left[\frac{C\bar\rho_m(z)}{(1+z)^3 D(z)}\right]^2 P_\delta(k,z) = \left[\frac{C\bar\rho_0\,\Omega_m}{D(z)}\right]^2 P_\delta(k,z)\,, \tag{1.76}$$

$$P_{\delta\tilde\gamma^I}(k,z) = -\frac{C\bar\rho_m(z)}{(1+z)^3 D(z)}\, P_\delta(k,z) = -\frac{C\bar\rho_0\,\Omega_m}{D(z)} P_\delta(k,z)\,. \tag{1.77}$$

We will use this formulism to simulate the IA effect in cluster weak lensing simulation (see Chapter 3 for details).

1.3.2   Galaxy shape in the image and its relation with shear

Generally, galaxy shapes are not perfectly elliptical in the astronomical image, *e.g.* their intrinsical morphology is irregular, or they are embedded in the noisy background, or they get pixelated in the CCD images. Nevertheless, we still want to estimate their shape in term of ellipticity, which is the parameter that gravitational shear can affect. Thus the shape of galaxies in the image can be estimated from the 2nd moments of their surface brightness $I(\theta)$ in the image (Blandford et al. 1991),

$$Q_{ij} = \frac{\int I(\theta)\theta_i\theta_j \mathrm{d}^2\theta}{\int I(\theta)\mathrm{d}^2\theta} \tag{1.78}$$

from which we can define their size ω and complex ellipticity ε with,

$$\omega = \sqrt{Q_{11}\,Q_{22} - Q_{12}^2} = ab\,, \tag{1.79}$$

$$\varepsilon = \frac{Q_{11} - Q_{22} + 2\,\mathrm{i}\,Q_{12}}{Q_{11} + Q_{22} + 2\omega} = \frac{a-b}{a+b}\,\mathrm{e}^{2\mathrm{i}\theta}\,, \tag{1.80}$$

and a, b are the major, minor axis length of an equivalent ellipse, and θ is its position angle.

The relation between the ellipticity thus defined and the gravitational shear can be derived from the transformation of the brightness moments with the Jacobian matrix. The conservation of surface brightness in lensing Eq.(1.35) requires,

$$Q_0 = \mathcal{A}\,Q\,\mathcal{A}^T\,. \tag{1.81}$$

With the definition of ellipticity, and expressing the Jacobian matrix in terms of the convergence and shear Eq.(1.34), the ellipticity and size transforms by (Seitz & Schneider 1997),

$$\varepsilon = \frac{\varepsilon_0 + g}{1 + g^*\,\varepsilon_0} \quad \varepsilon_0 = \frac{\varepsilon - g}{1 - g^*\,\varepsilon} \quad (|g| \leq 1) \tag{1.82}$$

$$\varepsilon = \frac{1 + g\,\varepsilon_0^*}{e_0^* + g^*} \quad \varepsilon_0 = \frac{1 - g\,\varepsilon^*}{e^* - g^*} \quad (|g| > 1) \tag{1.83}$$

$$\frac{\omega}{\omega_0} = \frac{1}{(1-\kappa)^2\,(1-|g|^2)} \quad (|g| \leq 1)\,. \tag{1.84}$$

In case of weak lensing, $\kappa \ll 1$ and $|g| \ll 1$, $\varepsilon \approx \varepsilon_0 + g$. Assuming that the intrinsic ellipticity averages out $\langle \varepsilon_0 \rangle = 0$, we find that the observed ellipticity on average gives an unbiased estimation of shear $\gamma \approx g \approx \langle \varepsilon \rangle$. This result justifies the possibility to estimate the weak gravitational shear from the measurement of galaxies shapes.

1.3.3 The practical measurement of shape

We have seen that, in the weak lensing, the ensemble average of source ellipticities is an unbiased estimate of the gravitational shear, thus depending on the strength of shear in study, the accuracy of the measurement of source shape, or ellipticities, is crucial to the physical properties of lenses.

There are two main practical difficulties in the shape measurement in the real observation data.

First, there is no noise-free data. Besides the flux from the galaxy that is the essential signal from which we are measuring the shape, there are also the photon counts from the sky background, and the shot-noise, usually approximated as Poisson noise, from both galaxy and sky background, and finally, the read-out noise, which is modeled as Gaussian noise. With these noise, the shape of galaxies we measured is never the original noise-free shape, before they are detected with CCD, especially when the galaxies are faint, extended, with low Signal-to-Noise (S/N) ratio. As we have shown that usually we use surface brightness moments to derive the ellipticity of a galaxy, the error of shape due to the noise, not only propagates into the 2nd brightness moment, the shape, but also be present in the 1st moments, which contaminates the measurement of the brightness center.

Second, even if there is no noise, which never happens in the real life, the shape of galaxy we measured is still not the original shape we are actually interested in. Like any optical system, the aperture size and features of the astronomical telescope limits the amount of incoming light, and result in a Point-Spread-Function (hereafter PSF) in the image. For a circular aperture, the PSF is in Airy pattern. With modern technology, the size of these PSFs can be reduced to the subpixel level, so in practice these isotropic PSFs never affects the shape measurement. Further complication arises when additional optic aberrations in the optics system changes the pupil phase, hence the Optical-Transfer-Function, or there are tracking or jittering modes during the observation, either of which introduces an anisotropic PSF kernel. If these instrumental biases in the shape measurement can be reduced or at least controlled within an acceptable level, for ground based telescope, an uncontrollable PSF comes from the turbulence of atmosphere seeing, which is on average isotropic, with common seeing size around $1''$ or larger, and with spatial pattern within the Field-of-View (FoV) changing with time. The images of galaxies in the real data, are the original ones convolved with an anisotropic PSF at the position of image, hence their shapes are biased differently. For faint distance galaxies, whose size is comparable or smaller than seeing size, their shapes are dominated by the PSF.

What is contained in the real data, is the PSF convolved objects contaminated by the noises, and within the process of image reduction, these two effects are usually correlated with each other. Thus, for faint distant galaxies with low S/N ratio, in order to separate the noise contamination in the shape from the PSF effects is not easy and one may has to assume the brightness profile of the galaxies before the measurement. For these galaxies, which contain important information of the weak lensing shear from the galaxy clusters, the shape measurement is usually very noisy.

Within the current thesis aiming for the study of weak lensing by galaxy clusters, we use oned of the working methods for PSF correlation and shape measurement, called KSB method, as we will introduce in the following.

The principle of KSB method

To model and correct for the PSF, Kaiser et al. (1995) and further work in Luppino & Kaiser (1997) suggest an approximation method, hereafter KSB method. It assumes that the gravitational shear g and anisotropic kernel of the PSF q are both small so that the change in the ellipticity can be approximated by the 1st order linearization, *i.e.* $\varepsilon' = \varepsilon + P^q \, q + P^g \, g$, where tensor P is the response of ellipticity to the anistropy, dubbed polarizability. The aim is to calculate these polarizabilities from the observables, calibrate the PSF anisotropy q with circular objects (stars) in the field, and average over the image ellipticities to give an estimator of shear $\langle g \rangle = \langle (\varepsilon' - P^q q)/P^g \rangle$, assuming the intrinsic ellipticities of galaxies average out.

In the following, we will define the intrinsic (not sheared) surface brightness profile and ellipticity as $I^{\rm s}$ and $\varepsilon^{\rm s}$, and accordingly the observed ones as $I^{\rm o}$ and $\varepsilon^{\rm o}$. Note here we denote the following definition for two components of complex ellipticity,

$$\varepsilon_1 = \frac{Q_{11} - Q_{22}}{Q_{11} + Q_{22}}, \quad \varepsilon_2 = \frac{2 \, Q_{12}}{Q_{11} + Q_{22}} \; . \tag{1.85}$$

Firstly, before convolved with the anisotropic PSF, the intrinsic ellipticity $\varepsilon^{\rm s}$ with surface brightness profile $I^{\rm s}$ is sheared by the *pre-seeing* gravitational shear g, with *pre-seeing shear polarizability* P^g, and then convolved by an isotropic PSF kernel o. We denote this operation and change in ellipticity by,

$$I^{\rm iso} = o \otimes S_\gamma(I^{\rm s}) \quad \Longrightarrow \quad \varepsilon^{\rm iso} = \varepsilon_0 + P^g \gamma \; . \tag{1.86}$$

The pre-seeing shear polarizability P^g can not be directly measured. But we can commute the convolution with shear operation by

$$I_1 = o \otimes S_\gamma(I_0) = S_\gamma[S_\gamma^{-1}(o) \otimes I_0] = S_\gamma[\, p \otimes I_0] \; . \tag{1.87}$$

In other words, applying the pre-seeing shear followed by the convolution of an isotropic PSF is equivalent to smear the original image with a *anit-shear pseudo* anistoropic kernel p first, and then apply the *post-seeing* shear,

$$I_0' = p \otimes I_0 \quad \Longrightarrow \quad \varepsilon_0' = \varepsilon_0 + P^{\rm sm} p \; , \tag{1.88}$$

$$I_1 = S_\gamma(I_0') \quad \Longrightarrow \quad \varepsilon_1 = \varepsilon_0' + P^{\rm sh} \gamma \; . \tag{1.89}$$

Thus, the pre-seeing shear polarizability P^g is re-written in terms of anti-shear smearing polarizability $P^{\rm sm}$ and post-seeing shear polarizability $P^{\rm sh}$,

$$\varepsilon_1 = \varepsilon_0 + P^{\rm sm} p + P^{\rm sh} \gamma \; . \tag{1.90}$$

The advantage of this change of variables is that $P^{\rm sm}$ and $P^{\rm sh}$ are directly measurable from the stars, simply for the reasons that stars are intrinsically circular and not sheared by gravitational lensing, hence their anti-shear polarizability compensates the post-seeing shear polarizability by

$$0 = 0 \; + P_*^{\rm sm} p + P_*^{\rm sh} \gamma \; . \tag{1.91}$$

Inserting Eq.(1.91) into Eq.(1.90) directly yields

$$\varepsilon_1 = \varepsilon_0 + P^g \gamma \quad \text{and} \quad P^g = P^{\rm sh} - P^{\rm sm} \frac{P_*^{\rm sh}}{P_*^{\rm sm}} \; . \tag{1.92}$$

Secondly, consider the post-seeing sheared ellipticity is further modified by an anisotropic PSF before observed, with kernel q and *smear polarizability* $P^{\rm sm}$,

$$I = q \otimes I_1 \quad \Longrightarrow \quad \varepsilon = \varepsilon_1 + P^{\rm sm} q \; . \tag{1.93}$$

Again making use of the stars which are intrinsically circular,

$$e_* = 0 + P_*^{\mathrm{sm}} q \tag{1.94}$$

we can express the anisotropy of PSF in terms of the ellipticities of stars, and obtain

$$\varepsilon = \varepsilon_1 + \varepsilon_* \frac{P^{\mathrm{sm}}}{P_*^{\mathrm{sm}}} \ . \tag{1.95}$$

Finally combining two steps Eq.(1.92) and Eq.(1.95), we arrive at the relation between intrinsic unsheared ellipticity and observed ellipticity through KSB method,

$$\varepsilon = \varepsilon_0 + \frac{P^{\mathrm{sm}}}{P_*^{\mathrm{sm}}} \varepsilon_* + (P^{\mathrm{sh}} - P^{\mathrm{sm}} \frac{P_*^{\mathrm{sh}}}{P_*^{\mathrm{sm}}}) \gamma \ . \tag{1.96}$$

As we mentioned in the beginning of the subsection, the raw measurement of shape in terms of quadrupole brightness moments is noisy, in practical calculation of this moments, a weight function $W(\theta)$, centered at the centroid of the image, is usually introduced to reduce the noise in the measurement, *i.e.*

$$Q_{ij} = \frac{\int \mathrm{d}^2\theta W(\boldsymbol{\theta}) I(\boldsymbol{\theta}) (\theta_i - \bar{\theta}_i)(\theta_j - \bar{\theta}_j)}{\int \mathrm{d}^2\theta W(\boldsymbol{\theta}) I(\boldsymbol{\theta})} \ . \tag{1.97}$$

The weight function is commonly chosen with a Gaussian profile, with width as the "typical" size[¶] of the galaxy r_{obj}, $W(\theta) \sim \exp[-\theta^2/(2\,r_{\mathrm{obj}}^2)]$. With the quadropole moments thus defined, the detail expression of P^{sm} and P^{sh} are shown (Hoekstra et al. 1998) to be as the following,

$$
\begin{aligned}
P_{\alpha\beta}^{\mathrm{sh}} &= X_{\alpha\beta}^{\mathrm{sh}} - e_\alpha e_\beta^{\mathrm{sh}} \\
X_{\alpha\beta}^{\mathrm{sh}} &= \frac{2}{Q_{11}+Q_{22}} \int \mathrm{d}^2\theta\, I(\theta) \left[(W\eta^2) + W' \begin{pmatrix} \eta_1^2 & \eta_1\eta_2 \\ \eta_1\eta_2 & \eta_2^2 \end{pmatrix} \right] \\
e_\alpha^{\mathrm{sh}} &= \frac{2}{Q_{11}+Q_{22}} \int \mathrm{d}^2\theta\, I(\theta) (W + W'\eta^2) \begin{pmatrix} \eta_1 \\ \eta_2 \end{pmatrix} \\
\\
P_{\alpha\beta}^{\mathrm{sm}} &= X_{\alpha\beta}^{\mathrm{sm}} - e_\alpha e_\beta^{\mathrm{sm}} \\
X_{\alpha\beta}^{\mathrm{sm}} &= \frac{1}{Q_{11}+Q_{22}} \int \mathrm{d}^2\theta\, I(\theta) \left[(W + 2W'\eta^2) + W'' \begin{pmatrix} \eta_1^2 & \eta_1\eta_2 \\ \eta_1\eta_2 & \eta_2^2 \end{pmatrix} \right] \\
e_\alpha^{\mathrm{sm}} &= \frac{1}{Q_{11}+Q_{22}} \int \mathrm{d}^2\theta\, I(\theta) (2W' + W''\eta^2) \begin{pmatrix} \eta_1 \\ \eta_2 \end{pmatrix}
\end{aligned}
\tag{1.98}
$$

where

$$
\begin{aligned}
\eta^2 &= \theta_1^2 + \theta_2^2 \\
\eta_1 &= \theta_1^2 - \theta_2^2 \\
\eta_2 &= 2\,\theta_1\,\theta_2 \ .
\end{aligned}
\tag{1.99}
$$

[¶]Without the knowledge of the surface brightness profile of the galaxy, the size is usually roughly chosen as the FWHM of the measured brightess profile, above some theshold above the background noise level. But this is just a rough guess of the size of galaxy, and for faint galaxies, the underestimate of the size of galaxies and hence the size of weight function, may bias the shape measurement and PSF correction.

Hoekstra et al. (2000) further derived the error estimation of ellipticities from the raw measurement,

$$
\begin{aligned}
\langle \Delta e_1^2 \rangle &= \frac{1}{(Q_{11} + Q_{22})^2} \left[(1 - e_1)^2 \langle \Delta Q_{11}^2 \rangle + (1 + e_1)^2 \langle \Delta Q_{22}^2 \rangle \right. \\
&\qquad \left. -2(1 - e_1^2) \langle \Delta Q_{12}^2 \rangle \right] \\
\langle \Delta e_2^2 \rangle &= \frac{1}{(Q_{11} + Q_{22})^2} \left[e_2^2 (\langle \Delta Q_{11}^2 \rangle + \langle \Delta Q_{22}^2 \rangle) + (4 + 2e_2^2) \langle \Delta Q_{12}^2 \rangle \right. \\
&\qquad \left. -4e_2 (\langle \Delta Q_{11} \Delta Q_{12} \rangle + \langle \Delta Q_{22} \Delta Q_{12} \rangle) \right]
\end{aligned}
$$

$$(1.100)$$
$$(1.101)$$

where the correlation between errors in the moments read

$$
\langle \Delta Q_{11}^2 \rangle = \frac{3\pi}{4} \sigma_{\mathrm{bg}}^2 \sigma_{\mathrm{obj}}^6 + \int \mathrm{d}^2 x \, I(x) \, W^2(x) \, x^4 \tag{1.102}
$$

$$
\langle \Delta Q_{22}^2 \rangle = \frac{3\pi}{4} \sigma_{\mathrm{bg}}^2 \sigma_{\mathrm{obj}}^6 + \int \mathrm{d}^2 x \, I(x) \, W^2(x) \, y^4 \tag{1.103}
$$

$$
\langle \Delta Q_{12}^2 \rangle = \frac{\pi}{4} \sigma_{\mathrm{bg}}^2 \sigma_{\mathrm{obj}}^6 + \int \mathrm{d}^2 x \, I(x) \, W^2(x) \, x^2 \, y^2 \tag{1.104}
$$

$$
\langle \Delta Q_{11} Q_{22} \rangle = \langle \Delta Q_{12}^2 \rangle
$$

$$
\langle \Delta Q_{11} Q_{12} \rangle = 0 + \int \mathrm{d}^2 x \, I(x) \, W^2(x) \, x^3 \, y \tag{1.105}
$$

$$
\langle \Delta Q_{22} Q_{12} \rangle = 0 + \int \mathrm{d}^2 x \, I(x) \, W^2(x) \, x \, y^3 \tag{1.106}
$$

in which the zero average of Gaussian background noise $\sigma_o b$ and Poisson shot noise $\sqrt{I(x)}$ is assumed.

The application of KSB method in practice

In this thesis work, the shape measurement and PSF correction is done with the improved KSB method, LENSR, developed by M. Radovich. Here we will briefly show how the PSF corrected galaxy ellipticity is obtained with LENSR, as a application of the principle introduced above.

We start with the raw shape measurement in the image. The galaxy ellipticity calculation is done by using a window function in order to suppress the outer, noisy part of a galaxy: the function is usually chosen to be Gaussian with size θ. The size of the window function is commonly taken as the radius containing 50% of the total flux of the galaxy (as given by e.g. the FLUX_RADIUS parameter in SEXTRACTOR). In LENSR, we proceed as follows. We define a set of bins with θ varying between 2 and 10 pixels (sources with smaller and larger sizes are rejected in our analysis), and a step of 0.5 pixel. For each bin we compute e_{obs}, P^{sh} and P^{sm}, and the ellipticity signal to noise ratio defined by Eq. 16 in Erben et al. (2005):

$$
\mathrm{SNe}(\theta) = \frac{\int I(\theta) W(|\theta|) d^2\theta}{\sigma_{\mathrm{sky}} \sqrt{\int W^2(|\theta|) d^2\theta}}. \tag{1.107}
$$

The optimal size of the window function, θ_{max}, is then defined as the value that maximizes SNe. Fig. 1.2 shows the typical trend of SNe, which was normalized for display purposes, as a function of θ. It can be seen (Fig. 1.3) that, on average, there is a constant offset between θ_{max} and FLUX_RADIUS. Below SNe ~ 5, FLUX_RADIUS starts to decrease: this provides an estimate of limit on SNe, below which the shape measurement is not meaningful any more.
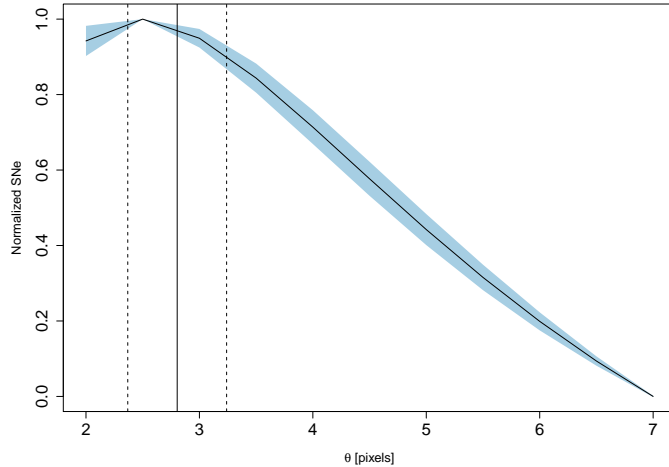
Figure 1.2: SNe is displayed as a function of the window function size, θ, used to measure ellipticities. For display purposes, galaxies were selected to have the same value of $\theta_{\max}$, and SNe was normalized so that min(SNe)=0, max(SNe)=1. The vertical lines indicate the average (solid) and standard deviation (dashed) of FLUX_RADIUS for the same galaxies.

The terms p and q, derived from stars, must be evaluated at each galaxy position: this is usually done fitting them by a polynomial (see e.g. Radovich et al. 2008), whose order must be chosen to fit the observed trend, without overfitting. The usage of the window function introduces a calibration factor, which is compensated by the P^γ term. This implies that stellar terms must be computed and fitted with the same value of θ used for each galaxy (Hoekstra et al. 1998). An alternative approach, not based on a constant order polynomial, is given e.g. by Generalized Additive Models: we found that the implementation in R (function GAM in the mgcv library) provides good results. Fig. 1.4 shows fitting and residuals of the anisotropic PSF component. The values of the fitted terms p and q at the positions of the galaxies are predicted by GAM, that also provides an estimate of the standard errors of the predictions, Δp and Δq. From error propagation, the uncertainty on e_{iso} was computed as:

$$\Delta e_{\mathrm{iso}}^2 = (\Delta e_{\mathrm{aniso}}/P^\gamma)^2 + (e_{\mathrm{aniso}} P^{\gamma-2} \Delta P^\gamma)^2, \tag{1.108}$$

where $(\Delta e_{\mathrm{aniso}})^2 = (\Delta e_{\mathrm{obs}})^2 + (P^{\mathrm{sm}} \Delta p)^2$ and $(\Delta P^\gamma)^2 = (P^{\mathrm{sm}} \Delta q)^2$; uncertainties on the measured values of P^{sm} and P^{sh} were not considered.

For each galaxy, a weight is defined as:

$$w = \frac{1}{\Delta e_0^2 + \Delta e_{\mathrm{iso}}^2}, \tag{1.109}$$

where $\Delta e_0 \sim 0.3$ is the typical intrinsic rms of galaxy ellipticities.

Stars and galaxies were separated in the magnitude (MAG_AUTO) vs. size plot. Instead of using e.g. FLUX_RADIUS as the estimator of size, we used the quantity δ=MU_MAX-MAG_AUTO, where MU_MAX is the peak surface brightness above background. Saturated stars were found in the locus of sources with constant MU_MAX; in the δ vs. MAG_AUTO plot, stars are identified as sources in the vertical branch. Sources with δ lower than stars were classified as spurious detections. In addition, we rejected those sources for which δ is $\sim 2\sigma$ larger than the median value. This is to exclude from the sample of stars used to compute the PSF correction terms, those sources for which the shape measurement may be wrong due to close blended sources, noise, etc.
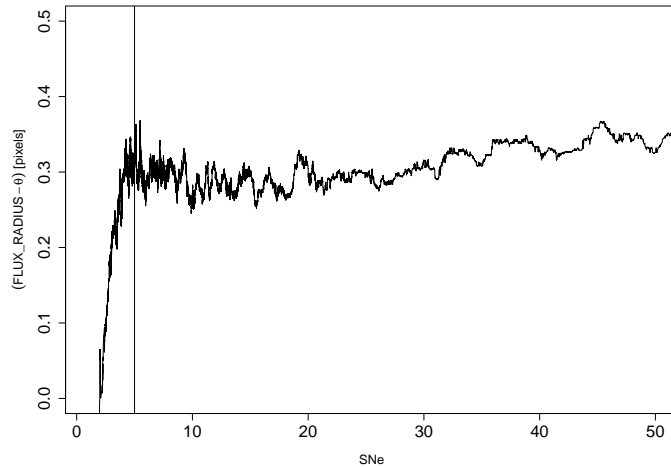
Figure 1.3: Running median of FLUX_RADIUS-$\theta_{\max}$ as a function of SNe. The vertical line shows the limit chosen for the selection of background galaxies.

We further excluded those galaxies with $w < 1$ or SNe < 5, for which the ellipticity measurement is not meaningful.

In the case of faint galaxies used for the weak lensing analysis, the ellipticity is underestimated due to noise. Such effect is not included in the P^γ term, which can be only computed on stars with high signal to noise ratio. Schrabback et al. (2010) proposed the following paramerization for such bias, as a function of the signal to noise:

$$m = \frac{e_k - e_m}{e_m} = a * (\text{SNe})^b, \tag{1.110}$$

where e_m and e_k are the ellipticities before and after the correction respectively. Such parameters were derived using the STEP1 (Heymans et al. 2006a) and STEP2 (Massey et al. 2007a) simulations, where both PSF and shear are constant for each simulated image. We obtain $a = -0.1$ and $b = -0.45$, which corresponds to a bias m changing from $\sim 5\%$ for SNe $=5$ to $< 2\%$ for SNe > 50. After such correction was applied, we computed again the average shear from the STEP1 and STEP2 simulations, and obtained a typical bias of $\sim 3\%$ for SNe $= 5$.

1.4   Observational requirements for weak lensing

In this section, we will list a number of observational conditions required by weak lensing study, and relevant aspects of some telescopes and weak lensing surveys.

In weak lensing, since the shear we want to measure is estimated from the average of galaxy ellipticities, while galaxies are not intrinsically circular, large samples of galaxies in the image are required to average out the intrinsic ellipticity dispersion. Given the field of view, large number of galaxies indicates high number density of galaxy which can be obtained with the deep exposure of the field. However, this depth can not be achieved with a single exposure since during long integration time, the foreground bright stars and galaxies will saturate. Thus, for the observation with weak lensing, a lot of short exposures are required, and later during the image reduction stage, they can be stacked to increase the S/N ratio of the faint objects, and to give the desired exposure depth.

Besides, the weak lensing shear of different objects extends into different area in the sky. For galaxy cluster, depending on its mass and redshift, the weak lensing shear of order $|\gamma| \sim 0.01$
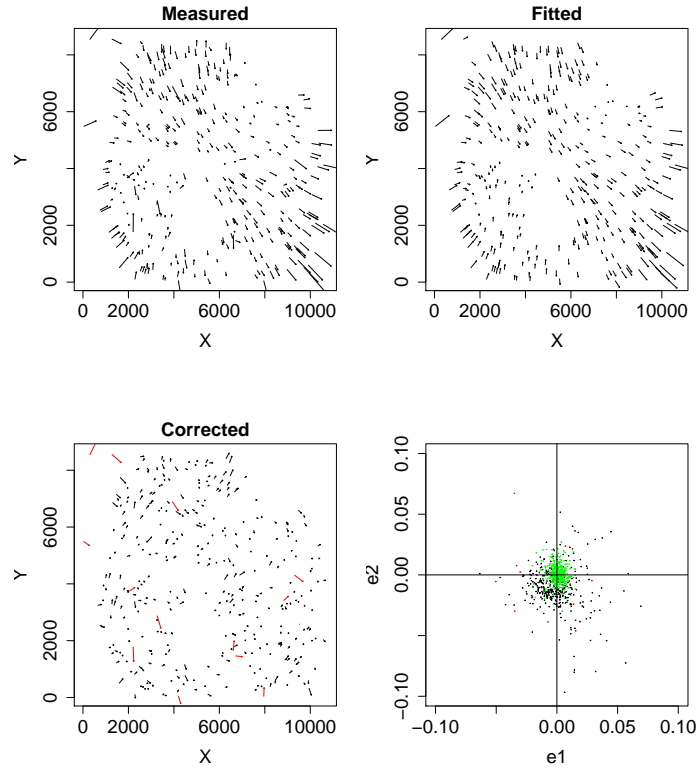
Figure 1.4: Example of PSF anisotropy correction (Huang et al. 2010): the first three panels show the ellipticity pattern (measured, fitted and residuals; X and Y are in pixels). In the last panel, black dots are the measured values, green dots are after the correction. Values rejected during fitting are marked in red.

can extend out to $10 \sim 30$ arcmin from the cluster center. As a comparison, the strong lensing effect such as giant arcs appears in a region only few arcmin around the cluster center. Thus, for a good sampling of cluster shear and collect sufficient number of background lensed galaxies, telescopes with large diameter mirror and hence big collective area, mounted with wide field CCD camera are usually used for weak lensing observation. For example, the field of view of MegaCAM camera mounted on 3.6-meter Canada-France-Hawaii-Telescope (hereafter CFHT) is $60' \times 60'$, while for the 8-meter Subaru telescope, its camera SuprimeCAM has a $34' \times 27'$ field of view.

Moreover, as the distant galaxies carrying the shear signal are usually faint, only a small fraction of their brightness profile is above the background. For the shape measurement of these galaxies, large pixel scale of the CCD can introduce the pixelation problem which prevents the accurate measurement of the shape. Thus, for weak lensing observation, the CCD pixel scale is usually very small, *e.g.* $0.168''$ for MegaCAM, and $0.2''$ for SuprimeCAM. In oder to reach the large field of view with this pixel scale, wide field cameras are usually equipped with an array of CCDs, or mosaic, *e.g.* 9×4 mosaic in case of MegaCAM, and 5×2 mosaic in case of SuprimeCAM. For a multi-CCD array, the tuning of flat field *w.r.t.* the focus plane is demanding. While in case of data, the management and reduction of wide field images usually

require specific pipelines.

The observational condition is also another important factor in the weak lensing image quality. For ground-based observations, the atmospheric seeing smears the objects in the image, which substantially affects the shape measurement of the faint background galaxies. Thus, a good seeing condition, with sub-arcsec FWHM of seeing size, is generally required in weak lensing observations.

As we will used the data observed with CFHT telescope, especially from the CFHT Legacy Survey (hereafter CFHTLS), here we will briefly introduce the survey.

CFHTLS[||] is a large project carried out with CFHT telescope during 2003 and 2009 for scientific topics ranging from solar system to extragalactic astrophysics. It consists of a 4 Deep fields, each with 1 deg^2, and 4 wide fields, covering 170 deg^2 area, c.f. Fig.1.5. The Deep

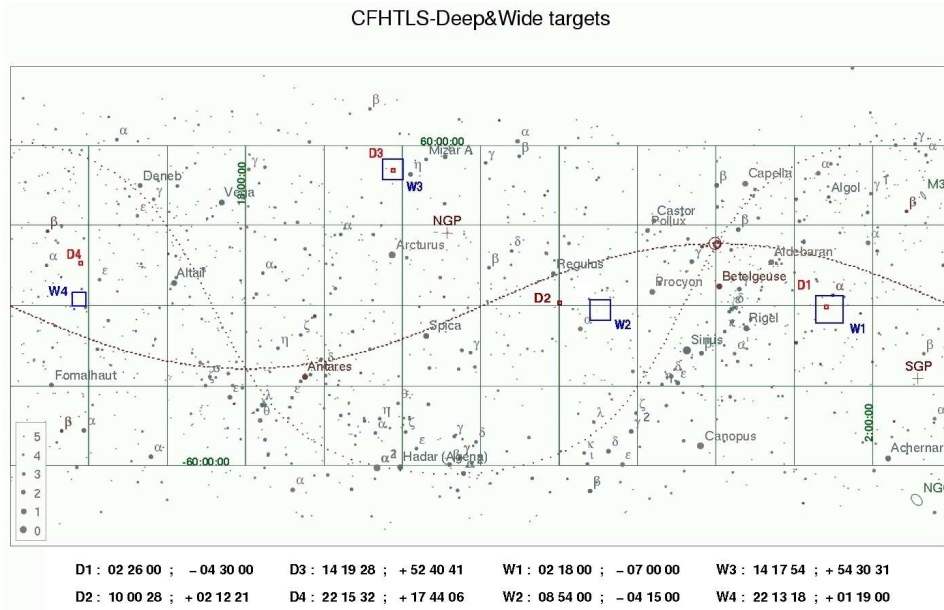| D1 : 02 26 00 ; −04 30 00 | D3 : 14 19 28 ; +52 40 41 | W1 : 02 18 00 ; −07 00 00 | W3 : 14 17 54 ; +54 30 31 |
| D2 : 10 00 28 ; +02 12 21 | D4 : 22 15 32 ; +17 44 06 | W2 : 08 54 00 ; −04 15 00 | W4 : 22 13 18 ; +01 19 00 |

Figure 1.5: Four Deep and four wide fields in CFHTLS survey.

fields are observed mainly aiming at the study of dark energy with type Ia Supernova, galaxy distribution and evolution, and weak lensing of galaxies clusters. The Wide fields are designed mainly for the study of large scale structture and matter distribution with cosmic shear, and also for the galaxy cluster study with the galaxy morphology and photometric properties. Both Deep and Wide fields are observed in 5 bands, namely $u*, g', r', i', z'$. The depth of Deep is $r' = 28$ while for Wide is on average $i' = 24.5$, which corresponds to a median photometric redshift of 1.0 and 0.5, for Deep and Wide, respectively. The survey has been observed totally 2300 hours over 5 years (450 nights), and the integration time for the Deep fields is about 40-60 hours/image, while 40-60 minutes/image for Wide fields. The raw data is pre-processing and calibrated with CFHT Elixir pipeline[**], and the image reduction is done by Terapix[††]. The stacked image for all the fields are stored at the Canadian Astronomy Data Center (CADC)[‡‡], and are publicly available subjective to a release period.

In the following works, we will discuss the image defect masking and weak lensing cluster detection method, which are both applied to CFHTLS data.

[||]http://www.cfht.hawaii.edu/Science/CFHTLS/
[**]http://www.cfht.hawaii.edu/Science/CFHTLS-DATA
[††]http://terapix.iap.fr/
[‡‡]http://cadcwww.dao.nrc.ca/cfht/cfhtls_info.html

Chapter 2

The Extraction Auto Masking

Real astronomical images contain not only the objects of scientific interest to be detected and measured, but also objects that are contaminated by image defects, due to the observation mishaps or other objects in the image. The problematic objects as well as the sources of defect should be excluded from the further analysis. Such a cleaning job can be done either in the image space, by looking for the problems by eye and manually masking them, or in the catalogue space, by filtering with criteria the catalogue of detections extracted from the image by some software. However, when there is a large number of spectacular image defects and spurious objects, but it is hard to find some simple criteria for catalogue filtering, addition work on extraction masking becomes non-trivial. This chapter is dedicated to this topic and the masking program ExAM, I developed to make life easier. This chapter is organized as follows. In Section 2.1, the need for masking will be explained, especially for the lensing images. Then in Section 2.2, some basics of image detection and measurement implemented in SExtractor will be introduced, which will be extensively used in the ExAM program. The detail illustration of the masking method is in Section 2.4. Finally, as an example, the application to the real data will be shown in Section **??**.

2.1   The need for masking

Weak gravitational lensing relies on the shape measurement of faint distant galaxies. Due to the weak shear signal and the low S/N of available sources, wide field images with deep exposures are generally required to give sufficient statistics. As a result, such images usually contain a large number of sources. For instance, in the deep images in CFHT Legacy Survey[*], with 40-50 hours of exposure time in r band, the number density of galaxies is about $40/\mathrm{arcmin}^2$.

In wide field images with typical FoV around $0.5 \sim 1$ square degree, the occurrence of bright stars, *e.g.* mag< 13 is not avoidable, as shown in Fig. 2.1[†]. During long integration time of observation aiming at imaging the distant galaxies, some of these bright stars will surely saturate, which results in two main images defects.

First, it is conspicuous that near some brightest saturated stars, there are reflection halos, with the center offset from that of the star, and in an annulus shape, with perceivable features of shadows of the secondary mirror and struts supporting the prime focus cage, thus also dubbed as "donuts", *c.f.* Fig.2.2a and Fig.2.2b[‡]. The diameter of the reflection halo is usually large, related to the mirror size and setup of optics, for the reason that will be clear soon,

---

[*]See Chapter 1 for general introduction of the survey

[†]Image source: `http://www.cfht.hawaii.edu/Instruments/Imaging/MegaPrime/tfmmegaprime.html`.

[‡]The pinhole image source: `http://www.cfht.hawaii.edu/Instruments/Imaging/Megacam/pinhole.html`.
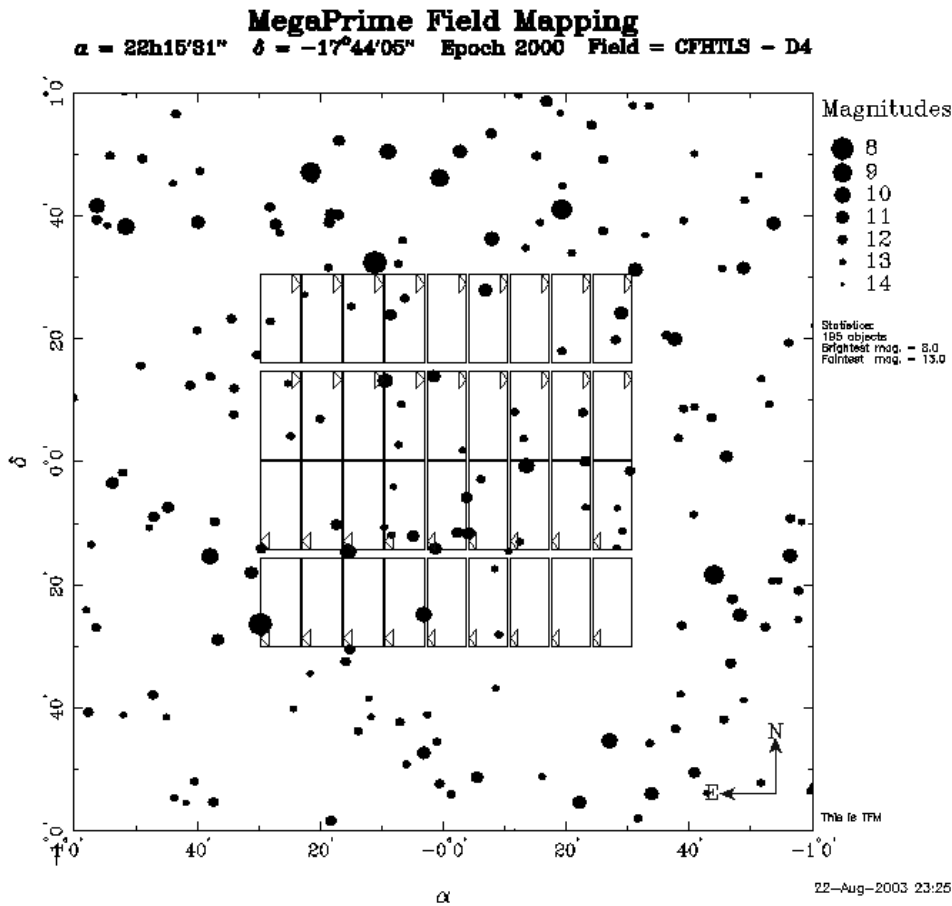
Figure 2.1: The map of stars brighter than mag=14, around CFHT-D4 field, generated with MegaPrime Field Mapping tool. The grid in the central part of the image shows the layout of MegaCAM CCD mosaic.

and they seriously degrade the background estimation of all the galaxies enclosed, of which the measurements are of course not reliable. Since in KSB method, the shape measurement relies on the brightness moments of the galaxies, the warp in the background and artificial light coming into the galaxy profile directly limits the accuracy of shape measurement. Therefore these contaminated galaxies are useless for further analysis, and must be masked out.

Second, more saturated stars, which may not be surrounded by the reflective halos, are centered on crosswise bright diffraction spikes mirroring the feature of supporting struts, Fig.2.2c. This effects, which may be the visual appearance pursued by amateur astronomers, are annoying defects since they are brighter than the reflection halos, quite common for most of the bright stars, and are essentially the leak of flux from the saturated star, onto the neighbouring faint objects of interests, in an uncontrollable way. Thus, these bright stars with spikes, together with their neighbours affected, should be excluded from analysis. Note that these common defects are not a problem only for shape measurement of galaxies in gravitational lensing study, but are quite general for any scientific imaging analysis.

The image defects masking seems an easy job, as long as there are not many of them in each image, and can be achieved manually. This is exactly the situation before the idea of automatic masking comes up. However, in images with high number density of galaxies, such as those for lensing study, it becomes tedious to open each image with hundreds or thousands Mega-Bytes in the image display software ds9 (Joye & Mandel 2003), adjust contrast in order
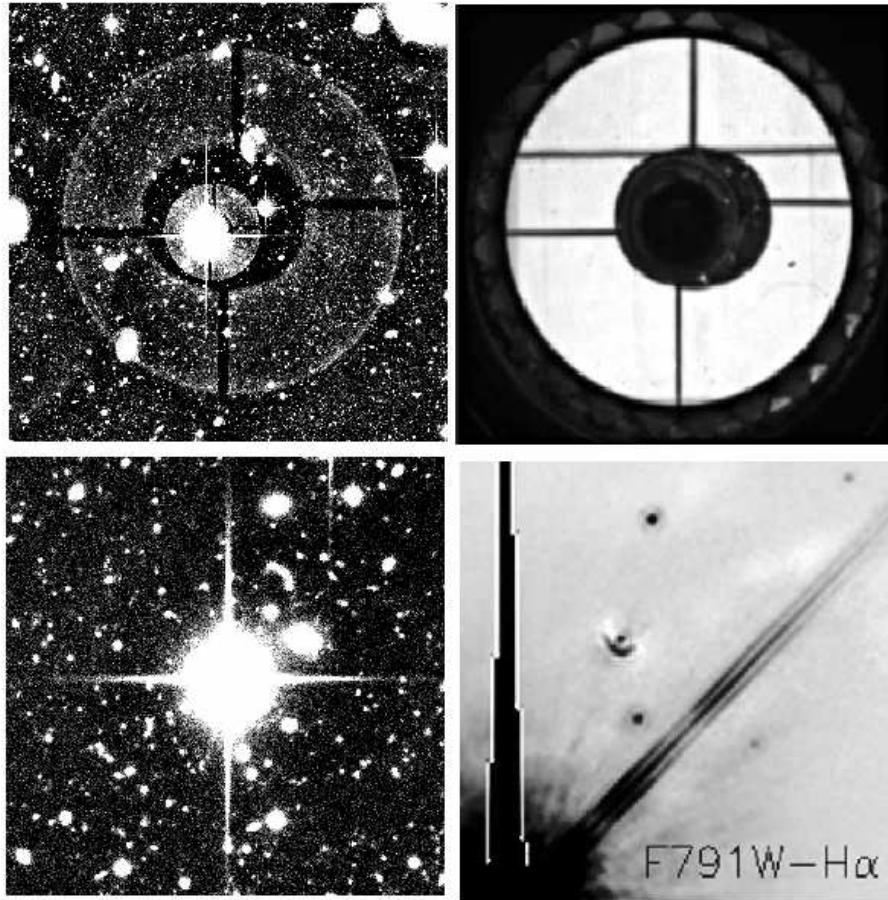
Figure 2.2: (a) *top-left:* Example of reflection halo in CHFTLS-D1 field. (b) *top-right:* Features of obstruction in CFHT MegaCAM field, obtained by imaging with standard filter replaced by pinhole masks. (c) *bottom-left:* Example of diffraction spike in CHFTLS-D1 field. (d) *bottom-right:* The detail of spikes near a star inside M8, observed by HST WFPC2 camera with F791W-Hα filter.

to find about ten reflection halos, and draw fit regions for thousands of saturated stars with spikes. For the latter, an lazier way could be to mask all the "spiky" stars with big circles, at the cost of a great loss of galaxies not affected by spikes. For the surveys such as CFHTLS or upcoming VST-KIDS, manually masking hundreds or even thousands of exposures would pose a serious demand on time and man-power.

At the same stage of source cleaning, another issue is the source classification of star and galaxy (hereafter S/G classification). For gravitational lensing, this is a crucial step, due to the idea of correcting the PSF of galaxies with point like stellar objects. Usually, stars and galaxies are separated in catalogue space, by selecting the stellar locus in the radius magnitude diagram, either manually or with some automated algorithms. Regarding the fact that the image defects we mentioned above are also related to the selection of stars in the image, the S/G classification with some algorithm can actually be done together with the masking. This is indeed the initial motivation in EXAM to automate the masking process. The rest of the work is just to find the proper selection or filtering criteria for saturated stars in the catalogue space.

2.2   The physical origins of spikes and halos

Before we investigate the method to mask the diffraction spikes and reflection halos, it is helpful to understand the origins of some common defects. This additional discussion provides a quick identification of the physical cause of image defects. It also shows that some observational mishaps are hard to fix through image reduction, and thus masking is a practical workaround to trade off the defects.

Diffraction spikes

Modern astronomical telescopes are almost all reflecting telescopes, which form images from reflections between one or combinations of curved mirrors. This design folds the light path and allows for objectives, here primary mirror, with very large diameter, collecting more light from large area. But most of the reflectors have either a secondary mirror or detection facilities, and struts supporting them, near the focal point of the concave primary mirror, which partially obstruct in coming light. Usually the struts are made thin enough to reduce the loss from their obstruction. The light diffracts when passing these thin lines of obstacle, and formed the light patterns in direction of struts, as "spikes". Fig.2.2d shows the diffraction pattern in a spike, in upper-right direction, near a star in M8, observed by HST WFPC2 camera with F791W-Hα filter[*]. The spikes, consisting of the light "bled" from the saturated star, is so bright that its radial airy pattern due to aperture diffraction, limited by the mirror of telescope, is also enhanced.

Due to the diffraction nature of the spikes, their thickness, length and intensity are not only related to the physical thickness of the struts, the brightness of the stars, but also the wavelength of the incoming light. Thus, for the same bright saturated star, the spikes may appear differently in images observed in different filters, and the modeling and correction for these diffraction patterns are not easy. Therefore, it is a optimal choice to just mask them.

Reflection halos

In the telescope, after the incoming light is reflected and successively corrected by a series of lens, *e.g.* the wide field corrector, and before it finally hits the CCD, it still has to pass some surfaces of different facilities. Typical example of these facilities can be the filter, dewar window of cryogenic chamber, and the coverslip of CCD, each with different thickness. Though these surfaces are usually coated with anti-reflective materials, the reflection of light from very bright sources between these surfaces is still unavoidable. Here we take the prime focus system in MegaPrime mounted on CFHT, as an example, illustrated in Fig.2.3. The optic setup of MegaPrime is shown on the right side of Fig.2.3. From the zoomed detail of the prime focus cage in the middle, we can see that a light reflected from the primary mirror successively passes the lens 1-4 of the wide field corrector, image stabilizing plate, the optic filter plate, the cryovessel window, and finally reaches the CCD surface. Along this path, part of light is reflected by multiple surfaces, and due to the distance between them, the reflected light from a inclined incoming light, will be offset away from the center. Of course, such reflected light is out of focus, therefore a blurred feature of the obstruction is finally perceived as donuts.

There are several properties of the reflection halos.

- It is achromatic, as only reflection is involved, and the same feature will be present in observations with different filters.

- The physical diameter of halo in the image, is closely related to the additional distance light travels between the reflection surfaces thus the optics setup, and focal ratio of the

---

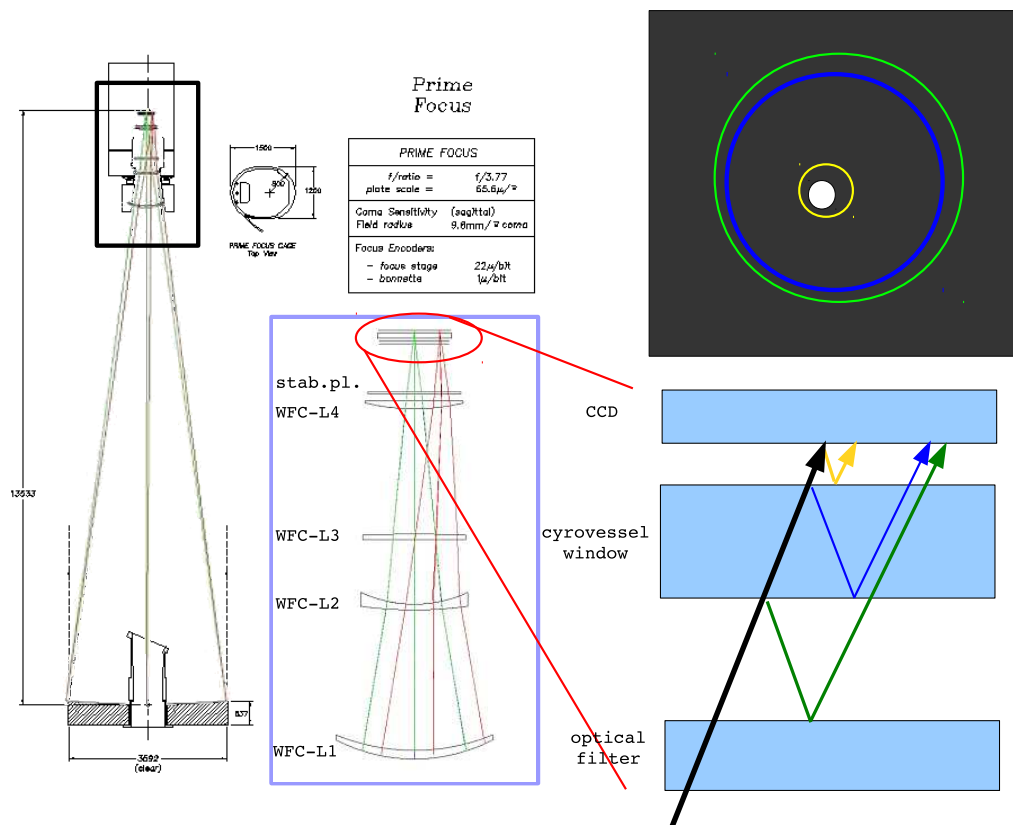[*]Image source: `http://antwrp.gsfc.nasa.gov/apod/ap010415.html`

Figure 2.3: *Left*: The prime focus setup of CFHT-MegaPrime. *Right*: The illustration of halos generated by multiple reflections of light between different surfaces in MegaPrime prime focus cage.

primary mirror. Generally, the closer the distance is, the smaller the halo.

- The brightness of halo is related to the source brightness and reflectivities of the surface, hence it also varies between optic systems.

- The offset of halo *w.r.t.* the center of star depends on how the reflecting surface or CCD is tilted. So the direction of offset and its center in the FoV can be different in different optic designs, like Prime-focus/Cassegrain, *e.g.* CFHT and Ritchey-Chrétien/Cassegrain, *e.g.* MPG/ESO-2.2m.

- Due to the vignetting effect, the detail features of reflection halos can vary across the field of CCDs, *e.g.* Fig.2.4 *.

In short, given the exposure depth required by the scientific goal, the bright reflection halos brought by very bright stars in the field, can not be easily fixed.

2.3   Introduction to SEXTRACTOR

The principle of automasking program ExAM is to filter the detection from the image with some criteria in the catalog space, and adopt the measurement of objects for the masking

---

*Image source: http://www.cfht.hawaii.edu/Instruments/Imaging/Megacam/pinhole.html.
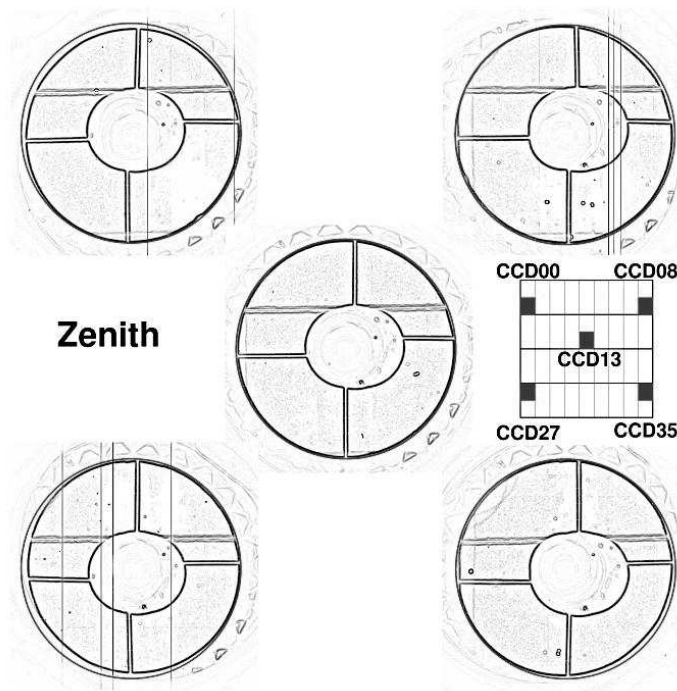
Figure 2.4: Vignetting effect in the 4 corners of the mosaic versus central position, for CFHT-MegaPrime.

profile. ExAM relies on SExtractor (Bertin & Arnouts 1996) for the extraction of objects in the image, and their relevant measurements. Thus, in order to understand why and how ExAM adopts the SExtractor results, in this section, we introduce the detection and measurement in SExtractor in detail. In the following, the keywords in SExtractor are in sans serif font while those in ExAM are in `typewriter` font, so that they can be distinguished from each other.

Suppose we are looking for mountains on isolated islands in the sea, with a 3d map which contains only the information of surfaces of both the objects, here the mountains and islands, and the background, the sea. The first problem to solve is to decide the sea level, which should be localized, since the fluctuation is changing from position to position. Next, how to distinguish between the small islands, and large fluctuations in the sea. And finally, after we identify the island above the sea, how to identify different mountain peaks on the island.

Astronomical image detection in the FITS data is quite similar to the mountain searching problem. An image in FITS format contains the flux of light at position on grids, or pixels. The photons from the luminous sky result in the background in the image, which is noisy, like the fluctuation in the sea, and may contains non-uniform spatial pattern, due to the bright objects or the instrument effects. Objects in the images are connected below or above the background, corresponding to islands or mountains on the island. As the background is noisy, *filtering* is usually applied to smooth the background in detection of "islands", or *segmentation*, and contrast criteria, or *thresholding*, is applied to separate the peaks of objects, a process called *deblending*. Then further measurements, like flux, center position and shape etc., are done for detected objects. These steps are actually the workflow of SExtractor on the input image, and finally generate of object catalogue, as output, with all the measurements. Below we illustrate some of the steps which are important to the measurements that will be used in ExAM.

Background estimation

The reflection halo estimation in ExAM depends on the local background estimation at the positions of galaxy. SEXTRACTOR background estimation is done by covering the image with a mesh grid, with mesh size controlled by BACK_SIZE, and taking the background value in each mesh, as a combination[§] of mean and median of the 3σ clipped histogram of pixel values in the mesh. The background mesh size should be chosen properly, as if it is too small, the mesh background is dominated by the influence from the bright sources, while if it is too big, it is insensitive to the local variance of background. Optionally, a median filter, with size controlled by BACK_FILTERSIZE in unit of number of meshes, can be applied to background mesh map, (and also the rms background map, see below,) to suppress the local overestimation of some mesh due to the enclosed bright objects or artifacts such as the reflection halos. Then the background map, together with an RMS-background-map, as an estimate of noise variance in the mesh, are bicubic-spline-interpolated between the meshes. Either map can be an output FITS image, when CHECKIMAGE_TYPE is set to BACKGROUND, or BACKGROUND_RMS. The low resolution maps before the interpolation can also be checked with CHECKIMAGE_TYPE is set to MINIBACKGROUND, or MINIBACK_RMS. Finally, the background map is subtracted in the input image before further analysis, with BACK_DEFAULT set to AUTO, and the RMS background map can be used as weight map (see below).

Filtering prior detection

Due to the background noise, some faint objects may not be detected or some detections may be purely noise. While the former may affect the detection of very faint stars at the S/N level where S/G is hard to separate, the latter may introduce fake detection as faint stars. For the difference in the power spectrum of the noise and the object, filter convolution can be applied, or optionally only to pixels with value within or above some threshold specified by FILTER_THRESH, to improve the accurate detectability, triggered with a boolean option FILTER[¶]. In topological aspects, filtering takes off-image pixel as zero, and assumed bad pixels interpreted. The simple filters for SEXTRACTOR are square digital ones, whose kernel is provided in an ASCII file passed to FILTER_NAME. Note the filtering only (directly) affects the detection and isophotal parameters, such as barycenter and object boundary, which we will extensively use for masking. The other detail measurement of profile and shape are nearly untouched. The result of filtering can be output as a FITS image, when CHECKIMAGE_TYPE is set to FILTERED.

Thresholding segmentation

The segmentation in SEXTRACTOR is done by thresholding pixels in the background subtracted, *filtered* image, and defining a group with pixels "8-connected" as a detection. The threshold value, controlled by DETECT_THRESH, is defined in unit of the standard deviation of background of image *before* filtering. Alternatively, one can use minimum number of pixels above threshold, controlled by DETECT_MINAREA, as further correction to detection constraint, and keep in mind that raising threshold while keeping proper a minimum area setting is a way more direct to reduce noise detection. Choosing a proper threshold value is crucial to obtain real detections. A low threshold may introduce lots of spurious detections, and for real detections, it may include the noisy background pixels into the isophot region, which is

---

[§]The combination is, Mode $= 2.5 \times$ Median $- 1.5 \times$ Mean, for crowded field, and Mode $=$ Mean otherwisely.

[¶]Note that the simple digital filters used in SEXTRACTOR may have some problems, such as, not preferred for detection of low surface brightness galaxies, reducing the contrast in blended objects in crowded fields, and possibly mismatching spatial varying PSFs. However, in current issue of masking, we are mainly interested in the detection of stellar objects, and their separation from galaxies, thus none of these problems matter.

used to determine if a star takes spikes in ExAM. Regarding the fact that in masking, we are interested in bright stars with high S/N, high thresholding in SEXTRACTOR is usually assumed for ExAM.

Multi-thresholds deblending

Overlapped or attached objects on one detection, or "island", are further separated with multi-threshold deblending, in SEXTRACTOR. In brief, the method cuts the flux profile of a parent object above background threshold, or cuts "mountains" on an "island" in altitude, into DEBLEND_NTHRESH levels of isophot, exponentially spaced for CCD images, as DE-TECT_TYPE set to CCD. From peak to root, above each level, if the total flux ratio of a sub-branch to the parent exceeds a contrast threshold, defined in DEBLEND_MINCONT, it is registered as a new single object, otherwise, the amount of flux in these pixels are assigned to one of the most contributed neighbour. It is obvious that if the contrast threshold is too large, blended objects remain the same, while if it is too small, single object may be break into crumbling fake objects, which in case of masking, may decompose a saturated star with spikes into bright core and pieces of bright spikes. For purpose of a careful check, CHECKIMAGE_TYPE can be set to SEGMENTATION, OBJECT, or -OBJECT, corresponding to a segmentation image with object ID as pixel value, original image with only objects, or with objects subtracted, respectively.

Cleaning

A further factor which affects the detection is the CLEAN boolean option. It offers the possibility to recheck the deblending after subtracting the flux contribution from the neighbouring bright sources, estimated with a Moffat profile.¶ The profile slope is controlled by CLEAN_PARAM, which biases the neighbour influence low as the parameter increases. As a result, by proper increasing the cleaning effect, some fragmental detections originally assigned to very brighter object far behind the nearest neighbours may be re-identify as a new detection. This subtle effect is interesting as it changes the boundary points of a bright object.

Weighting

Information of image defects, such as bad pixels, CCD gaps, image warping or vignetting can be considered in the detection through a map weighting each pixel with its noise intensity. The weight image can be calculated internally as the RMS background map as mentioned above, whose pixel value is in unit of ADU, when WEIGHT_TYPE is set to BACKGROUND, or an external FITS image named with WEIGHT_IMAGE, whose pixel value can be the absolute standard deviation, relative variance to be scaled (in unit of ADU^2), or the weight as the inverse of the relative variance, depending when the WEIGHT_TYPE parameter is set to MAP_RMS, MAP_VAR or MAP_WEIGHT, respectively. When a weigh map is introduced (when WEIGHT_TYPE is not NONE), a threshold can be set, with WEIGHT_THRESH, which is the lower limit in weight value and upper limit in variances and standard deviation, in order to clean the unwanted pixels in detections.

Weighting is an important issue as it affects all the steps mentioned above. The low-weighted pixels are discarded before the background estimation. The weight map is also convolved with the filter, like the background subtracted image, if filtering is applied prior to detection. Then the convolved weight map sets detection thresholds for each pixel. Before filtering and thresholding, low-weighted pixels are reassigned the values interpolated from their surrounding neighbours. In cleaning, deblending recheck is done with pixel thresholds

---

¶The Moffat profile reads $I(r) = I(0)(1 + k\,r^2)^{-\beta}$, with the cleaning parameter β.

in the weight map. The weighting also enters the error estimates in the measurements. As the detection and measurement in SEXTRACTOR are separated into two passes, it is possible to apply the weighting only in one of the steps, and the corresponding thresholds in detection and measurement can be set differently into DETECT_THRESH and ANALYSIS_THRESH, respectively.

Due to the role weight map plays in the detection and measurement, in ExAM the weight map is also used to be combined with region files into a master flag image, for the next run of SEXTRACTOR detection (see below).

Flagging

For each object, SEXTRACTOR calculates an internal flag, named FLAGS in the output catalog, as an indicator of possible problem occurred in the detection. For each type of problem, the flag value is a power of 2, and if the detection involves several problems, their flags are combined with bitwise AND. Possible internal flag values are:

FLAG	meaning
1	The MAG_AUTO photometry of the object is biased by the bright neighbours, or at least 10% of the integrated area is affected by bad pixels.
2	The object is blended with another object.
4	The object contains saturated pixels with threshold of saturation pixel value controlled by SATUR_LEVEL
8	The object is truncated at the image bounder.
16	The aperture data of the object is incomplete.
32	The isophotal data of the object is incomplete.
64	Deblending involved with memory overflow.
128	Extraction involved with memory overflow.

If an external FITS flag image, with integer flag value on each pixel, is given as input, to the option FLAG_IMAGE, SEXTRACTOR can also combine the flags of pixels within the *isophot* area of the object, write the combined flag for the object (as IMAFLAGS_ISO) and the number of pixels of interest (as NIMAFLAGS_ISO) into the output catalog. The types of combination, options for FLAG_TYPE, are:

TYPE	Description
OR:	IMAFLAGS_ISO: pixel flag values are bitwise ORed
	NIMAFLAGS_ISO: number of non-zero pixels
AND:	IMAFLAGS_ISO: non-zero pixel flag values are bitwise ANDed
	NIMAFLAGS_ISO: number of non-zero pixels
MIN:	IMAFLAGS_ISO: signed minimum of all the pixel flag values
	NIMAFLAGS_ISO: number of pixels with IMAFLAGS_ISO
MAX:	IMAFLAGS_ISO: signed maximum of all the pixel flag values
	NIMAFLAGS_ISO: number of pixels with IMAFLAGS_ISO
MOST:	IMAFLAGS_ISO: the most common pixel flag value
	NIMAFLAGS_ISO: number of pixels with IMAFLAGS_ISO

With the option of external flag image for detection, it makes sense to combine the weight map, regions of saturated star, diffraction spikes and reflection halos into one master flag image and pass it to SEXTRACTOR as an external flag image. With this master flag, SEXTRACTOR can be run again and calculate the combination of flag values within the object's isophot area, which can serve as a indicator whether an object overlaps with regions of image defects. This is indeed

why ExAM gives an option to make a master flag image.

As a summary to above discussion of detection with SExtractor, a typical list of relevant SExtractor configuration parameters is shown in the following, especially for ExAM.

Parameter	Value	Description
CATALOG_TYPE	FITS_LDAC	Output catalog format
DETECT_TYPE	CCD	CCD exponential multi-thresholding
DETECT_MINAREA	5	minimum number of pixels above threshold
THRESH_TYPE	RELATIVE	in background standard deviation σ_{bg}
DETECT_THRESH	3.0	in background standard deviation σ_{bg}
ANALYSIS_THRESH	3.0	in background standard deviation σ_{bg}
FILTER	Y	apply filter for detection
FILTER_NAME	default.conv	name of the file containing the filter
DEBLEND_NTHRESH	32	Number of deblending sub-thresholds
DEBLEND_MINCONT	0.01	Minimum contrast parameter for deblending
CLEAN	Y	Clean spurious detections
CLEAN_PARAM	5.0	Cleaning efficiency
WEIGHT_TYPE	MAP_WEIGHT	uses external weight image
FLAG_TYPE	MIN or MAX	MAX if bad pixel flag = 1, MAX otherwise.
SATUR_LEVEL	50000.0	level (in ADUs) at which arises saturation
BACK_TYPE	AUTO	subtract internal background map
BACK_SIZE	128	Background mesh size in pixel
BACK_FILTERSIZE	3	Background filter in unit of mesh
BACK_FILTTHRESH	0.0	Threshold for background-map filter

2.3.1 SExtractor measurements used in ExAM

The parameters that SExtractor can measure are listed in a file passed to PARAME-TERS_NAME. Among them, some are used in ExAM to separate stars and galaxies and as an estimate of contamination in the object from the image defects. Here we also list the least required measurement parameters that will be analyzed in ExAM:

Parameter	Description
NUMBER	index number of extraction
FLUX_RADIUS	radius containing 50% total flux of the object
MAG_AUTO	magnitude measured within elliptical aperture
	with aperture size determined from brightness moments
MU_MAX	brightness peak pixel magnitude of the object
CLASS_STAR	star/galaxy classifier from neutral network
FLAGS	flags for different detection problems
XWIN_IMAGE	position measured with Gaussian window weight function
YWIN_IMAGE	position measured with Gaussian window weight function
ISOAREA_IMAGE	isophotal pixels of the object above the detection threshold
XMIN_IMAGE	boundary limit isophotal area of the object
YMIN_IMAGE	boundary limit isophotal area of the object
XMAX_IMAGE	boundary limit isophotal area of the object
YMAX_IMAGE	boundary limit isophotal area of the object

2.4   The masking algorithm in ExAM

As we have seen from the above discussion, images defects such as reflection halos and diffraction spikes, for which there is no easy fix, must be masked. Due to their varying properties *w.r.t.* the optics system, the sources brightness and the exposure time, it is also not simple to find a universal criteria to identify and measure the defects, which imposes some difficulties in automating the masking process.

In this section, I will show how these difficulties are overcome with the masking program Extraction Auto-Masking, hereafter ExAM. In brief, ExAM takes a catalogue of sources extracted from the image with SEXTRACTOR, selects the stellar objects from the catalogue, picks up saturated stars among them, and provides the masking profiles, whose features controlled by the user. For reflection halos, the positions of the very bright star are extracted from external standard catalogue, such as USNO or 2MASS. The local background of sources within expected halo profile are measured as a reference to rank the intensity of the halos, and a number of the brightest ones are masked. The output of ExAM can be chosen as ASCII region format, which can be viewed with ds9, or a flag image FITS (or Flexible Image Transport System) format (Wells et al. 1981). Additionally, ExAM can combine the weighting information or user provided mask regions with masks internally generated into a master-flag image in FITS format. Once ExAM is configured for observations with certain type of telescope, the process is quite efficient and automatic, which saves lots of manual labor.

In following subsections, we will look into these steps in detail.

2.4.1   S/G separation

In order to mask saturated stars in the image, the first step in ExAM is to select stars from a SEXTRACTOR catalog. Here we take the catalog extracted from CFHTLS D1 image for example, with SEXTRACTOR configuration as shown above.

The usual approach to select stars is by defining a region, so called *stellar locus*, in the size-magnitude diagram, as shown in Fig.2.5a. In the plot, each point represents a detection in the image. The horizontal axis is the size of the object, measured by FLUX_RADIUS, and the vertical axis is the magnitude, MAG_AUTO. In such a diagram, bright and big objects are located in the lower-right corner while faint and small ones in the upper-left corner.

The main perceivable features in the plot are: a big clump of detections in the upper (fainter) part of the plot, representing the galaxies, and a vertical bar with similar (small) size, representing the not saturated stars, followed by a curved tail going to the brighter and bigger end, representing the saturated stars. Since stellar objects are point-like, the size of a star in the image is just that of the PSF, which is dominated by the atmospheric seeing, for ground based observation. Thus the vertical bar, which is defined as the unsaturated stellar locus, consists of stars with different magnitudes but the similar seeing size. When the star is very bright, the electrons converted from the photons, emitted by the star, exceed the maximum amount of charge that a pixel is able to collect and transfer, and the pixel get saturated and the electrons bleed into the neighbouring pixels. As a result, the size of very bright star in the image, characterized by the radius enclosing half of its flux, increases as the star gets brighter, *i.e.* the size and magnitude are no longer independent, resulting in a bright curved saturated tail as we see in the plot. On the other hand, the fainter end of the vertical bar mixes up with the clump of galaxies, which shows that in size-magnitude diagram, faint stars are usually hard to be distinguish from the galaxies which are so faint that only a small portion of flux exceed the background threshold. In lensing study, the detections which are reliable to be classified as stars, and are useful for PSF modeling and correction, are located in part of the vertical bar, below the mixing point, and above the turning point of saturation. The goal of
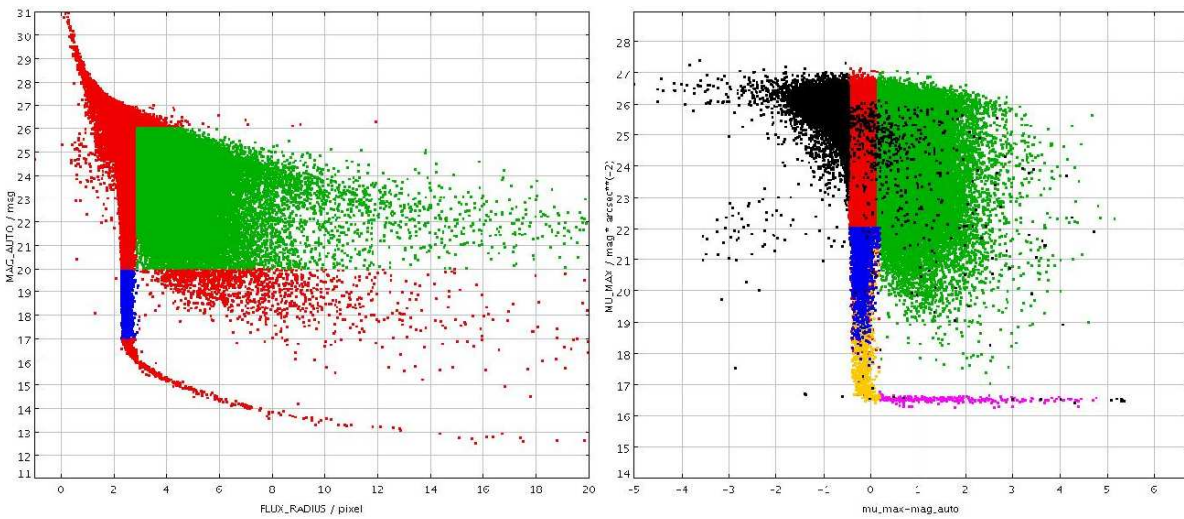
Figure 2.5: (a) *left panel* Size-magnitude diagram of extractions (red dots) from CFHTLS D1 image in r' band. The size is measured with FLUX_RADIUS and magnitude with MAG_AUTO. The stars (blue dots) and galaxies (green dots) are manually selected. (b) *right panel:* Similar size-magnitude diagram for the same data but with MU_MAX-MAG_AUTO as "size" and MU_MAX is magnitude. Compared to the original definition of size-magnitude, the vertical stellar locus and horizontal saturation bar allows for automatic classification of sources with algorithm. In this diagram, galaxies are in green dots, good stars for PSF correction in blue, stars with spikes in yellow, saturated stars in magenta, and spurious detection in black, all done with ExAM automatically.

S/G separation, at least for lensing study, lies in the method to pick up this range vertical bar in an fast and automatic fashion.

Algorithms to search for dense regions in parameter space can be greatly simplified if the expected region of interest is of "good" shape, *i.e.* if it is compact, and elongated parallel or perpendicular to the parameter axis. But this is not the case for stellar locus auto-searching in size-magnitude space, as the saturation tail is curved. However, a good mapping between the parameter spaces is found, by replacing the size FLUX_RADIUS by the difference MU_MAX-MAG_AUTO, and the magnitude MAG_AUTO by MU_MAX, as shown in Fig.2.5b. The previous stellar locus and saturation tail after the mapping are each along one of the axis, which allows for an automatic detection algorithm. The physical reason behind such a mapping is as follows. If a star is not saturated, the ratio between the peak flux to the total flux is nearly constant, as the flux profile follows the light distribution of the PSF. So the difference between MU_MAX and MAG_AUTO remains constant, independent of the brightness of the star, measured with the peak flux, or MU_MAX. Thus the stellar locus is a vertical bar in the diagram. Once the star is saturated, the peak flux reaches the saturation threshold and remains constant, while due to the bleeding of electrons to the neighbouring pixels, the total flux still increases as the star gets brighter and brighter. As a result, for saturated stars, the difference between MU_MAX and MAG_AUTO increases (as the ratio between peak and total flux decreases), which results in a horizontal bar of saturated stars.

Taking the advantage of the shape of the locus of saturated and unsaturated stars, the search task can be automated by projecting the loci onto each axis, analysing the histogram and locating the boundaries. Specifically, the algorithm is divided into following steps. For convenience, we denote x and y for MU_MAX-MAG_AUTO and MAG_AUTO, respectively.

1. Take a histogram in x with a subsample of objects in the catalog, in magnitude range $y \in [0, 20]$, and define the peak of the histogram as the center of unsaturated stellar locus x_c^v. The magnitude range is empirical but efficient to force the statistics dominated by stars, as dashed line 1 in Fig.2.5b. Then objects within a vertical bar centered on this peak, with width $x_c^v \pm 0.5$ are selected, with upper and lower boundaries $y_{\max}^v$ and $y_{\min}^v$, set by the faintest, brightest objects in this range.

2. Select a subsample of objects in the lower 60% of the left half of the vertical bar, and define the lower statistical limit$^{\parallel}$, of these objects as the lower boundary of the unsaturated star $x_{\min}^v$. Similarly take the lower 40% object in the right half vertical bar, the upper limit $x_{\max}^v$ is estimated. The reason to choose lower percentage of objects in the vertical bar, is to reduce the contamination from spurious detections ($x < x_c^v$) and from galaxies ($x > x_c^v$) in the statistics.

3. Finally the stellar locus for unsaturated stars is selected within the vertical bar $x \in [x_{\min}^v, x_{\max}^v]$, and $y_{\min}^v, y_{\max}^v$ are updated by magnitude range of objects with CLASS_STAR above a threshold for unsaturated stars, typically $C_*^{\mathrm{uns}} > 0.8$. Thus the boundaries of unsaturated stellar locus box is defined.

4. For the horizontal bar of saturated stars, the similar approach is done, namely, the horizontal center y_c^h is the peak of histogram in magnitude for subsamples of objects in range $y_{\min}^v \pm 0.5$, and $y_{\min}^h, y_{\max}^h$ are found with similar statistical limits.

After the stellar locus boxes are marked out, the detections within the regions are further filtered to give a final selection of stars. In the vertical box, only detections with SExtractor S/G flag CLASS_STAR above the threshold REG_SGUNSAT, *and* with detection flag FLAGS below the threshold REG_SEXFLAG are classified as unsaturated stars.

While in the horizontal box, all detections are classified as saturated stars *except* those with CLASS_STAR below threshold REG_SGSAT, and those with FLAGS below the threshold REG_SEXFLAG. These criteria reduced the possibility of mis-classify a galaxy as star, and exclude bad detections which is not suitable to adopt their measurements for mask profile.

The above algorithm for stellar locus detection uses a statistical approach, which relies on the number of objects in the statistics. It may not work for shallow exposures with very few number of stars, typically around 20 or below, or images with very small field, *e.g.* single CCD from a mosaic, in which there are few galaxies and stars. These special cases are usually also not suitable for lensing studies. The workaround can be either to change the empirical parameters in ExAM given sufficient tests, or simply mask these few bright stars by hand!

Once the boxy regions of saturated and unsaturated stars are decided with S/G separation algorithm, objects within these regions, classified as stars, are further checked for features of spike.

2.4.2   spike thresholding

As we mentioned, due to the physical origins of the diffraction and readout spikes, the intensity of these defects depends on the telescope, observation, and the bright sources, so there is no universal relation to derive their flux. However, since in the real life, the features of spike are most easily discerned by eyes at a flux level a few σ_{bg} higher than the background, where σ_{bg} is the standard deviation of background measured in SExtractor, an isophot

---

$^{\parallel}$The statistical lower limit here refers to that, if the histogram is generally increasing in large x, the lower limit of x is the saddle point of bins in the lower end, or the first null bin encountered when decreasing x. Similar concept applies in the upper limit.

contour analysis is a convenient approach to detect them numerically. For this reason, in configuration of SEXTRACTOR, the detection threshold is set typically to $3 \sim 5\,\sigma_{\mathrm{bg}}$, higher than common setting for measurement of faint galaxies.

The geometry idea for spike recognition is as follows. Consider a circle, enclosed by a circumscribed square box, its radius r_0 equals to the *perimeter radius* estimated from the size of the box a, $r_0 = r_p := a/2$, and also equals to the *area radius* estimated from the area of the circle A, $r_0 = r_a := \sqrt{A/\pi}$. If the boundary of the circle is not smooth, due to additional *extended* features such as spikes, in general the size of boundary box and the area will increase, so that $r_0 < r_p$, $r_0 < r_a$, c.f. Fig.2.6.
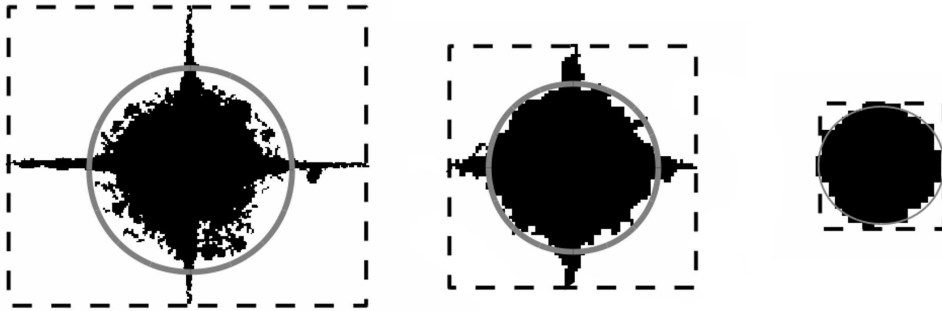

Figure 2.6: The dependence of the isophotal perimeter (length of dashed line) and isophotal area (enclosed by the grey circle) on the spikes features, from SEXTRACTOR segmentation image of CFHTLS D1 image. As the spike becomes significant, both the perimeter radius r_p and area radius r_a increase.

In case of a star in the image, if its original radius r_0 is the FWHM of seeing, the perimeter radius r_p and area radius r_a, measured from the object's isophot area and boundaries,

$$r_a = \sqrt{\mathsf{ISOAREA\_IMAGE}/\pi} \tag{2.1}$$
$$r_p = (\mathsf{XMAX\_IMAGE} - \mathsf{XMIN\_IMAGE} + \mathsf{YMAX\_IMAGE} - \mathsf{YMIN\_IMAGE})/8 \,, \tag{2.2}$$

can serve as the indicator for spikes. ExAM calculate r_a and r_p for each stars in stellar locus, and marks the ones, whose radii above the thresholds set by the user, for later spike masking. The diffraction spikes and CCD saturation are not necessarily relevant, for the former is a result of diffraction around the obstacle in the light path, while the latter is related to the charge capacity of the CCD. Thus the spikes check is done for all the objects classified as star.

Note also that the real seeing size r_0 is not used to estimate the extent of spikes, for two reasons. First, seeing size is generally different between observations, and even in one image, it may vary across the field. Thus the ratio r_p/r_0 or r_a/r_0 may not always indicate the spikes. Second, even if the seeing size is constant in field and well-measured, and given that the ratio r_p/r_0 or r_a/r_0 can be related to the length of spikes in some naive geometry models, the number of spikes, their rotation angles, the additional blended neighbours within the isophotal region and the pixelization of faint stars can complicates or even breaks the simple relation. However, in any case, the trend, that spikes increases the perimeter and area radii, always holds, which allows for the thresholding approach.

In ExAM, the values of the threshold for readout and diffraction spikes, can be controlled as input, through the configuration parameter SPKR_THRESH and SPKD_THRESH, together with the meaning of the threshold defined in SPKR_TTYPE and SPKD_TTYPE. The available choices of the threshold type can be perimeter radius (PERI), area radius (AREA), or the minimum (MIN) or maximum (MAX) of the two. In practise, the setting of threshold and its type is quite stable

for certain telescope, so that once a configuration of ExAM for one telescope is done, it can serve as a template for all the future masking works on data observed with this telescope. The examples of ExAM configuration will be shown in Appendix.A.3.

2.4.3   saturation and spike mask profile

Stars, that are saturated and/or with spikes, are masked with proper profiles provided in ExAM. The user has the full control over the scaling of these mask features. The key of scaling is to effectively cover the image area contaminated by the core and/or spikes in a star, while leave objects in the uncontaminated regions available for analysis.

For saturated stars, in order to mask their bright core, the mask is a circle centered on windowed position of the star (XWIN_IMAGE, YWIN_IMAGE), measured in SEXTRACTOR. The radius of the circular mask can be scaled *w.r.t.* the effective radius estimated from the area of isophots r_a, with a scaling factor set in the input configuration, STAR_RADF.

Note that for very bright saturated stars, this windowed position may not represents its true position in the image, since its central brightness profile is truncated due to the saturation and the charge transfer process may further ruin the pixels along the readout direction. As a result, SEXTRACTOR may just identify any one of the highly saturated pixel along the bright readout spike as the center of that star. Actually it has been checked that, in this case, any position measurement of the star fails. However, the good news is that this extreme case rarely happens, and it can be diagonised from the detection flags, which is the reason why for stars, we only use the measurement for those whose detection flags is *below* a value as configured by REG_SEXFLAG. We also note that such stars often produce reflection halos, so that they can be masked together with the halo masks, with their position extracted from the external star catalog.

The mask features are treated differently for diffraction and readout spikes, since while the latter is always along column or row in the FITS image, the former may rotates according to the rotation angle of supporting struts during the observation. The diffraction spike mask can have maximum 4 spikes** in anticlockwise order, with different angles given to the configuration parameter SPKD_ANG. Each spike mask is approximated with an isosceles triangle with height and width specified by SPKD_SLEN, SPKD_SWID, scaled *w.r.t.* to what is define in scaling type SPKD_STYPE, similar to that of thresholding type. In case of readout spike mask profile, at most 4 (rectangle) spikes are allowed, but in East-North-West-South order. The length and width of each spike can be specified differently, similar to those of diffraction spikes.

Note that for each star with spikes, a scaled circular core mask is also applied to avoid the leak of diffraction light outside of spike masks in the center. Again, the scaling configuration of spike features are found to be stable *w.r.t.* the telescope used for observation. ExAM leaves the flexible choices of scaling to the user not only because the scaling of the defect features depends on the specific observation configuration at hand, but also due to the fact that sometimes for the same star, according to the science goal and the person processing the masks, the requirement on the extent of mask can be different.

Finally, as an example, we show the mask profile for some of saturated stars in the CFHTLS D1 image in Fig.2.7.

**Each of the 4 spikes has an symmetric counterpart with position angle difference π.

**In case only 2 parameters are specified, the mask profile is a cross with two different lengths and the two parameters are specified in horizontal-vertical order.
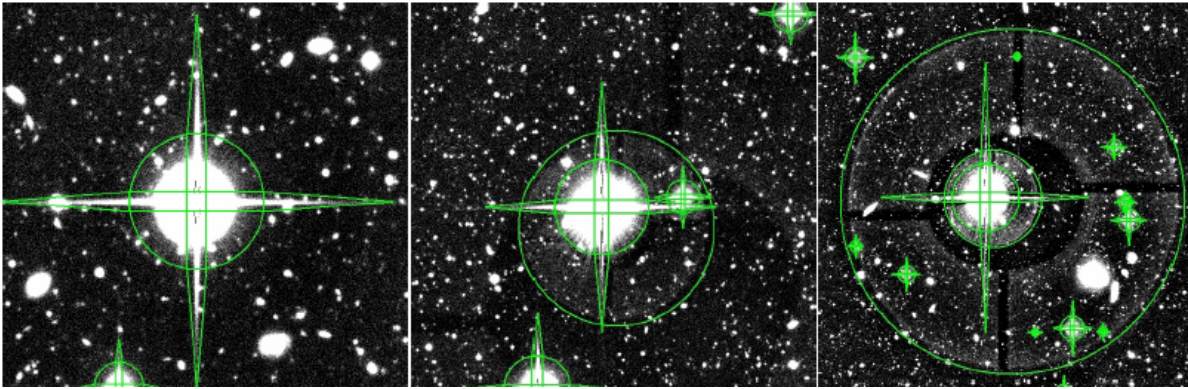
Figure 2.7: The mask profile for a sample of saturated stars in the CFHTLS D1 image

2.4.4 halo masking

The reflection halo masking is slightly different from the treatment in saturation and spikes, for three reasons. First, the shape and offset pattern of the halo *w.r.t.* to the star is closely related to the optics in the telescope due to their reflection nature which we have discussed. Thus, when the image is obtained with a special telescope for the first time, it is necessary to "guess" and "learn" (numerically rather than manually) the reflection halo features from the image. Second, given the depth of exposure, the stars that produce reflection halos are usually too bright to be measured accurately in SEXTRACTOR, as we discussed in previous subsection, so that their positions, which is the only information needed for halo masking, can be borrowed from external standard star catalog. Third, compared to spikes, which are common and obvious, the conclusion of whether there is indeed a perceivable halo in the image around a bright star, is inevitably subjective and sometime subtle. Thus, after configuring the halo features, ExAM leaves the decision to the user how many most brightest halos he/she would like to mask.

Before taking any guess about the halo features, we first extract the position of the most bright stars from the external catalog, like USNOB1 (Monet et al. 2003) or 2MASS (Skrutskie et al. 2006). This is achieved with a script, that wraps the cdsclient tools like `findusnob1` or `find2mass`, formats the extracted catalog and converts the sky coordinates to the image coordinates with WCS tools (Mink 2002) `sky2xy` The extracted bright stars are ranked in magnitude in the filter close to the one used in the observation. The number of stars is internally set to be 100, in the script, which is more than enough compared to the number of reflection halos in the image.

With the coordinates of "top 100" brightest stars in the image, ExAM provides a "guess" mode, with configuration `RUN_MODE` set to `GUESS`. In this mode, the program takes the star catalog as input and plots in a region file, the reflection halos centered on the stars, with guessed radius set by `GUESS_HRAD`, for "top 10" brightest stars in the catalog, which is enough to estimate the halo features. The user is supposed to open the image with ds9, load the region file with guessed halos, keep the regions only for halos actually present in the image, adjust their sizes and positions, and save the region file again. The thus output region file contains the available halo positions in the image and their "host" star positions.

Then switch ExAM to `LEARN` mode, and read the corrected guess region file as pointed by `LEARN_REG`. ExAM will fit the average radius of halos, their global offset center and linear offset parameters as a function of radius to this center. The parameters are saved to the halo

---

**The CDSClient program package is public available at `http://cdsarc.u-strasbg.fr/doc/cdsclient.html`. The WCS tools is available for download at `http://tdc-www.harvard.edu/wcstools/index.html`

feature configuration file `HALO_CFG`.

Finally in the `MASK` mode, in which the stars are selected and masked, the halo feature configuration is loaded, together with the "top 100" brightest star catalog. With the detail information of expected halo positions "learned", ExAM will load the SExtractor background map, and check the SExtractor centroid background value (`BACKGROUND`) of all the detections in the expect halo regions, and take their median values as the indicator of intensity of the reflection halo, c.f. Fig.2.8. At last, the halo intensity thus calculated are ranked, and a number, as `HALO_NUM` given by the user, of most intensive reflection halos are masked with the learned features.
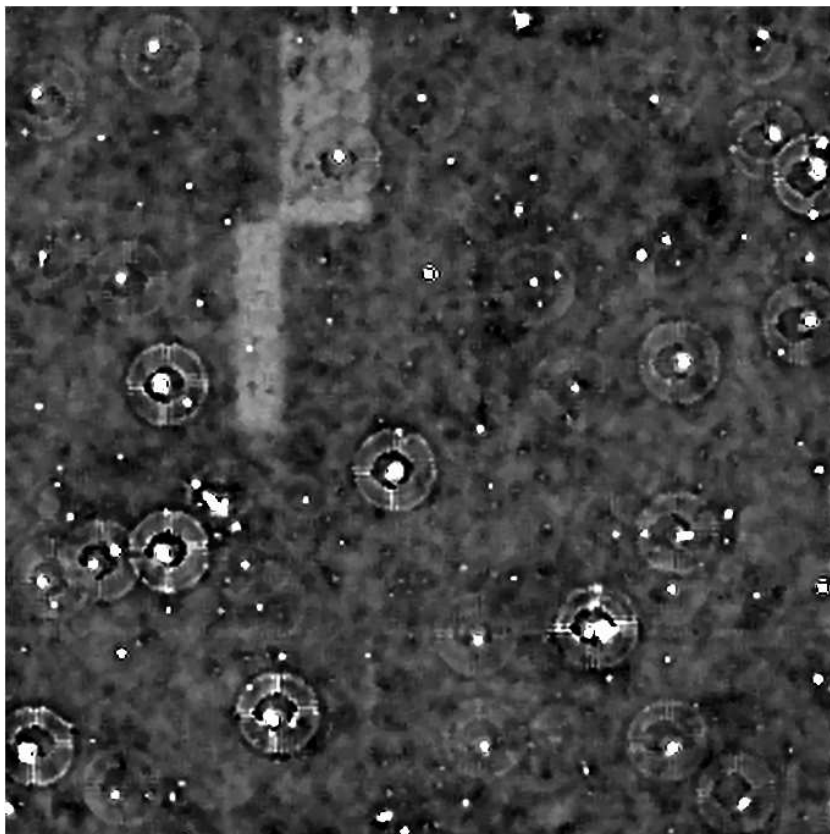
Figure 2.8: The background map of CFHTLS D1 image, measured with SExtractor. The intensity of reflective halos can be well observed. ExAM makes use of this map for the rank of the brightness stars with halos in the image, with the star position extracted from external standard star catalog, *e.g.* USNOB1.

Note in the `LEARN` mode, at least 2 real halos are required for learning. The fewer the halos, less accurate would be the fitting of halo features. Of course, if for one observation run, the exposures are generally shallow, the reflection halo can be masked just manually. The learning process also assumes that the vignetting effect is properly reduced in the image, which otherwise would lead to different halo sizes across the image.

2.4.5   outputs of ExAM

The main output of ExAM is the ds9 region file containing the mask regions of reflection halos, the saturated stars and the spikes. It can be used to filter the detection catalog after the SExtractor run. However, as such filter just check if the detection *center* is within the mask

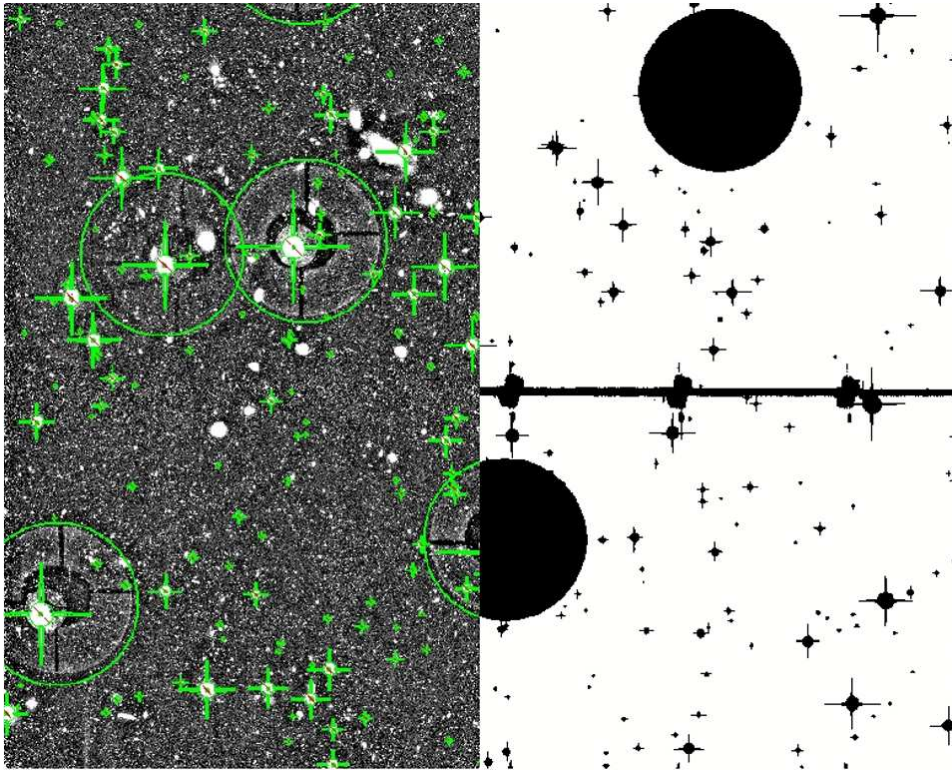Figure 2.9: The output of ExAM for CFHTLS D1 images. There are two formats in the output of ExAM, region file which can be viewed with ds9 (*the left half*) and a flag image in FITS format (*the right half*), containing the pixel mask of boundaries and CCD gaps, derived for weight map.

regions, detections with isophot area overlapped with mask regions are not generally cleaned, which means the remaining objects could be still partially contaminated by the image defects.

The solution to get over this worry, is to generate a flag image, run SEXTRACTOR again with the flag image as input, and check the `IMAFLAG_ISO` measurement to see if the object's isophot overlaps with mask regions, as we discussed in the flagging of SEXTRACTOR (see subsection?). ExAM offers the possibility to generate a 1/0 flag FITS image with the mask regions, even those read from an external mask region file, pointed by `EXT_REG`, when the region flag type `FRG_TYPE` is switched from `INT` (internal region) to `EXT` (external region). There are several tools to convert region to FITS, but usually the efficiency is low, *e.g.* , with FUNTOOLS, it takes half a day to convert a 10,000 regions into a flag FITS image, while with ExAM, it takes seconds. The great improvement in the efficiency of the conversion results from the algorithm used in ExAM. For each region, either in circular, triangular, or polygon form, ExAM first estimate their boundary points, and within the boundary box, it checks whether a pixel locates inside/outside the region. Compared to looping over all the regions for flagging each pixel in a wide field image, this algorithm shows its advantage. The output flag FITS image is named `FLAG_NAME`.

Objects detected near the boundaries of image or in the gaps of CCD which are partially covered with dithering pattern in the observations, usually have some problems in the measurement due to their low S/N. The positional information of these objects is contained in the weight image, which gives lower weight, thus high variance, in these regions. This can

---

**A FITS library and utility package developed at the High Energy Astrophysics Division of SAO, available at `https://www.cfa.harvard.edu/~john/funtools/`.

also be combined into the flag image in ExAM, through marking the pixels in these region as problematic, *e.g.* with integer value 1. It is done by importing the weight image by its name `WT_NAME`, thresholding the weights with a value, `WT_THRESH` either as an absolute value, setting `FWT_TYPE=ABS`, or the quantile of statistics, `FWT_TYPE=QNT`. In the quantile case, the sampling of the weight image, since it is as big as the wide field image, can be set with a grid size specified by `WT_SAMPLING`. The weight flag image is combined `AND` with the region flag image in the pixel space, and a master flag image is generated, when the `FLAG_TYPE` is set to `ALL`, *e.g.* Fig.2.9. Optionally, it can also be set to `WT` or `REG` for a flag image with only weighting or regions, respectively.

Chapter 3

Cluster weak lensing simulation

The gravitational shear, from which we can derive the physical properties of the lens, is estimated from the shape of distant galaxies. In weak lensing, since the change in the ellipticity of galaxy image due to the shear is typically around $1\% \sim 10\%$, and in addition, galaxies are not intrinsically circular, it is crucial to have sufficient statistics from galaxy sampling, and accurate shape measurement, with errors less than 1%. However, the sufficient statistics usually comes from a large number of distant faint galaxies, whose shape measurement are inevitably noisy. Thus, simulation for shape measurement becomes necessary to trace the bias and reduce the errors.

On the other hand, even assuming an accurate shape measurement, not all the clusters can be detected by weak lensing, and not all the mass estimates are accurate for detected clusters, for various reasons. For instance, the observation is relatively shallow for the detection of high redshift low mass clusters, or the galaxies are not randomly oriented but intrinsically aligned due to their local gravitational tidal field, or the weak shear of the cluster in galaxies in region far from the center is contaminated by the cosmic shear, or the cluster has more complex properties, such as substructures or triaxiality, than what we expected from a simple model, etc.. For this consideration, realistic lensing simulation in cosmological context is helpful.

In this chapter, I will first quickly review these two kinds of simulations, analyse their pros and cons in Section 3.1, and then in Section 3.2 introduce the simulation program I developed, SHUFF, which is essentially a tool to simulate a catalog of galaxies lensed by galaxy clusters, with sources, lenses and noise properties as inputs and various configuration options. The output from the simulation will be shown in Section ??. They can be used either to calibrate shape measurement method, or to test cluster detection, *e.g.* LENSFILTER, which will be introduced in the next chapter.

3.1 Available simulations for weak lensing

With the rapid development in the computer science and technology, numerical simulations have been intensively exploited to solve astrophysical problems in various physical scales, from star formation to the structure formation in cosmological context. For gravitational lensing, there are two kinds of simulation in literature for different purposes.

The first kind of simulation takes the dark matter particles from N-body cosmological simulation, project the particles onto two dimensional lens planes, calculate the deflection angle map of the lens plane, and then apply the lensing effect to an image of background galaxies. In this type of lensing simulation, the deflection angle map plays a key role. It contains the information of matter distribution derived from N-body simulation. On the other hand, once the deflection angle map is obtained, the lensing effect is realized by shotting a light ray from

observer today, passing through the lens plane and getting deflected according to deflection angle map and finally arriving at a position in the image with source galaxies. Thus the pixels in the lensed and unlensed images are mapped with the tracing light ray, so called ray tracing simulation (e.g. Meneghetti et al. 2008; Hilbert et al. 2007). The highlight of ray-tracing simulation is that it is a realistic simulation of gravitational lensing by the various structures in the Universe, with both strong and weak lensing effects (Merten et al. 2009), which provides the possibility to study in detail the physics of the realistic lenses. The shortcoming is that, since the lensing is done in image space, the pixel mapping and resampling is computational heavy, and to improve the efficiency, one may need special designed graphical hardware, such as Graphic Processing Unit (GPU) (Merten et al. 2009; Bate et al. 2010). The output of the ray-tracing simulation is usually the lensed galaxy image, on which one has to apply the shape measurement method to extract the shape information of the lensed galaxies.

The other kind of simulation is aimed at the shear measurement calibration. it originates from the problem of reducing the systematic bias in the shear measurement, in order to reach a high accuracy for cosmic shear study. Collaborations were setup among the cosmic groups to work calibration of measurement with the simulated images of galaxies containing the artificial input shear. The simulation is designed by the Shear Testing Programme (STEP) for the calibration of different shear measurement pipeline, *i.e.* for KSB (STEP-I)(Heymans et al. 2006b) and for Shapelets (STEP-II) (Massey et al. 2007b). The idea further grows into a competition, within and outside of the lensing community, for an accurate shear measurement method, called Gravitational LEnsing Accuracy Testing 2008 (GREAT08) (Bridle et al. 2010) and 2010 (GREAT10) (Kitching et al. 2010). The highlight of this type of simulation is that the image of galaxies with shearing effect is easy to produce, *e.g.* with SKYMAKER(Bertin 2009), and the shape information before and after the shearing effect are available. STEP I,II and Great08 assume a constant shear, as their purpose is to calibrate the accuracy of shear measurement achievable with different pipelines. This will be not the case for the Great10 simulations, where the shear field will be simulated as a Gaussian Random Field. Therefore, these simulations are not suitable to simulate the shear expected e.g. from galaxy clusters.

Regarding our purpose to calibrate the shape measurement as well as the cluster detection and mass estimation methods, a new weak lensing simulation is desired, featuring the realistic shear from galaxy clusters, and providing shape information of galaxies in the simulation, and yet not so computationally consuming. To this end, I developed cluster weak lensing simulation, SHUFF, where the input and output are catalog of unlensed and lensed galaxies, respectively, and the lensing effect of analytical triaxial NFW/SIS halos is applied to the shape of galaxies in catalog-space.

3.2   Shuff Simulation

3.2.1   Sources

SHUFF takes a catalog of unlensed source galaxies as input. The source galaxies can be either generated by a simulation program STUFF*, written by Emmanuel Bertin (Bertin 2009), or be configured in SHUFF itself for as a mock catalog. In the following, we will introduce these two ways for source galaxies simulation.

Source properties simulated with STUFF

STUFF is a program that simulates "perfect" astronomical catalogues. It generates object

---

*The program is publicly available at `http://www.astromatic.net/software/stuff`

lists in ASCII which can read by the SkyMaker[†] program, developed by Emmanuel Bertin and Pascal Fouqué (Bertin 2009) to produce realistic astronomical fields.

The program can be configured for simulation of observations with specific filters and observational conditions like field of view, CCD pixel scale, etc. Given the parameters for the cosmological standard model, the simulated galaxies are drawn from the distribution of Schechter luminosity function (Schechter 1976). The luminosity function can be parameterized specifically for different galaxy types, and allows for a evolution in redshift, for each galaxy type. Given the galaxies types defined in the simulation, and the evolutionary luminosity functions parameterized according to the observational fitting results available in literature, a catalog of galaxies are simulated with intrinsic luminosities and distribution in redshift. With the spectral energy distribution (SED) of the galaxy defined according to the galaxy type, the intrinsic luminosity of the galaxy is then converted to the apparent magnitude in the simulated bands.

The morphology of the galaxies are also simulated in Stuff, though all the shapes are described only by ellipses. Each galaxy's brightness profile consists of an exponential bulge and a de-Vaucouleur disk, of which the flux ratio is decided by the galaxy type. The size of bulge and disk are drawn from observational constrained distributions (de Jong & Lacey 2000; Binggeli et al. 1984), and the axial ratio of the bulge is distributed according to Sandage et al. (1970), while the inclination angle of disk is random. These distributions can actually be easily updated with the new results published in literature. The two dimensional position of all the galaxies are randomly distributed in the field of view.

As a result, the output galaxy catalog from Stuff simulation contains a list of galaxies with their positions, redshift, magnitude, galaxy type, bulge-to-total flux ratio, size, axial ratio and position angles of bulge and disk.

The features of the properties of galaxies simulated with Stuff is that they are all parameterized according to the theoretical (or observational constrained) models. The simulation is done in catalog space, which is computationally faster to obtain and easier to handle, than the simulation of galaxy images in the pixel space. Moreover, the simulation image can be easily obtained with the imaging program SkyMaker, which takes an ASCII galaxy catalog of the same format as that from Stuff, and produce an astronomical image containing all the galaxies as well as various instrumental effects, like configurable PSF models realistic flux noises and saturation of bright stars. Fig.3.1 shows a comparison of SkyMaker simulated images with only the galaxies simulated with Stuff(Fig.3.1a) and the same field but with anisotropic PSF, atmospheric seeing, background noises, and bright saturated stars Stuff(Fig.3.1b). It can be seen that while the very faint galaxies disappear in the background, all the additional noisy effects change the intrinsic shape of galaxies. Note here there is no lensing effect, which will be introduced with Shuff simulation.

Besides elliptical shapes for the bulge and disk component of the galaxy, which may not allow for detail structures in the galaxy, such as spiral arms, the other disadvantage of Stuff simulation is that, the shape and density of the galaxies are uncorrelated, which for the moment, may not be used to simulate the clustering effect due to the underlying gravitational field. Also despite the multiple band simulation, the color and morphology is not correlated with the environment either. In addition, since the redshift of galaxies are derived from the evolutionary luminosity function, its distribution may not be simply parameterized as modelled in most lensing study.

However, for our purpose of source galaxies for weak lensing of galaxy cluster, what Stuff simulates is fairly enough and easy to achieve. We can also make use of the features of Stuffformat catalog and its compatibility with SkyMaker, so that in the lensing simulation,

---

[†]The program is publicly available at `http://www.astromatic.net/software/skymaker`
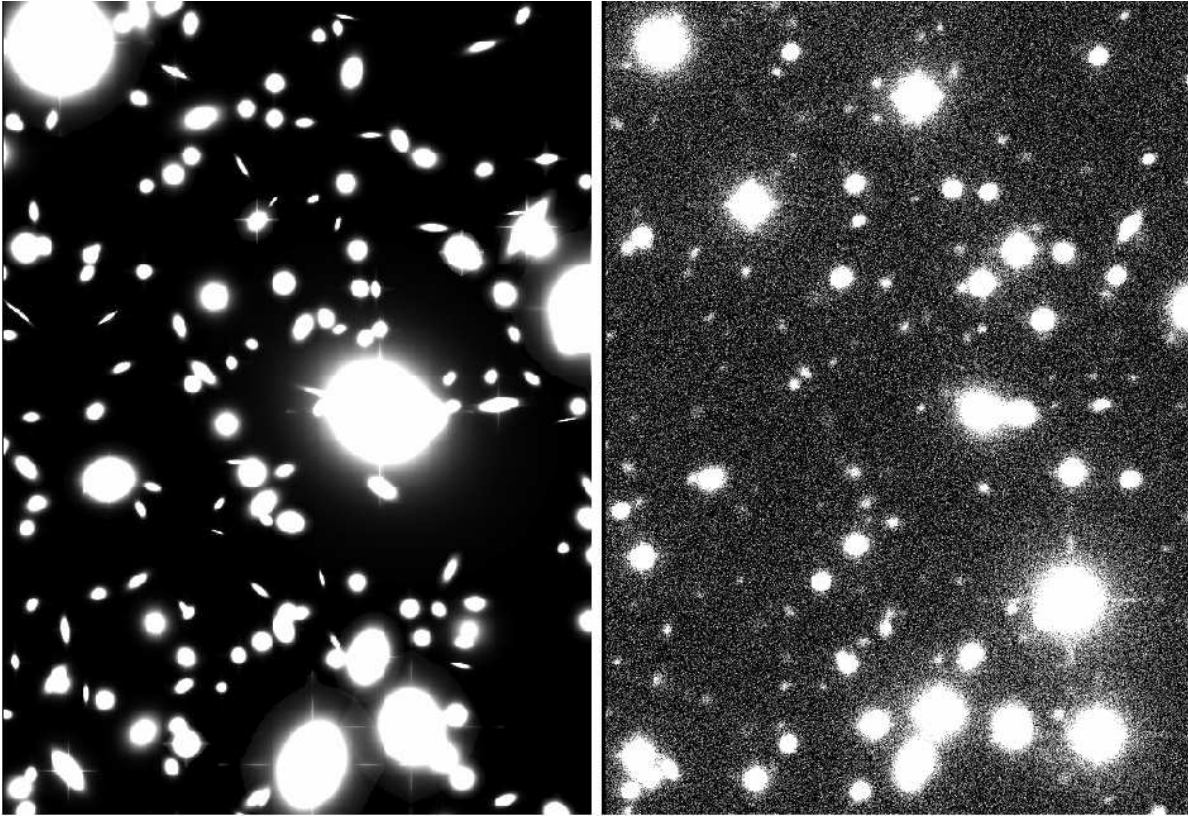
Figure 3.1: The simulated images produced by SkyMaker, with Stuff galaxy catalog as input. Two panels represent the same field with the same galaxies. (a) *the left half* shows the simulated galaxies with their intrinsic shapes, while (b) *right half* shows how the galaxy appearances are affected by the additional imaging effects simulated in SkyMaker, like PSF, atmospheric seeing, noise in the background and saturation stars.

physical informations about the shape and photometry of the galaxies can be separated from the imaging effect such as noises and PSFs. The shortcomings like source redshift distribution and shape correlations can be introduced later in the Shuff simulation, as we will discuss right after.

Source properties modelling/modification in Shuff

Shuff takes the aforementioned galaxy catalog from Stuff as the input of source galaxies to be lensed. The properties of these simulated galaxies are derived from the theoretical models with parameters fitted to observations. Since the fitting parameters used in Shuff depends on the observational data available and literature published, they may not be up-to-date or suitable for lensing study. For instance, according to the evolution model of luminosity function for a specific galaxy type, the redshift distribution of galaxies of the same type is found to be skewed towards high redshift, which is too deep compared to realistic redshift distribution in the lensing data. On the other hand, from the lensing point of view, there are parametrized redshift distributions commonly adopted in lensing studies, which are easy to parameterize and compare with other distributions. In addition, lensing strength is sensitive to the galaxy intrinsic ellipticity dispersion, number density of background galaxies and their spatial distribution, which are not directly controllable in Stuff. Under these consideration, Shuff offers some further configurations of source properties for lensing study purpose. This flexibility is realized

with the setting of source mode `SRC_MODE` in SHUFF simulation.

While in "Stuff" mode, (`SRC_MODE = STF`), all source properties are exclusively taken from the STUFF catalog; in "Mock" mode, (`SRC_MODE = MOC`), a mock source catalog will be generated internally and the input source galaxy catalog is ignored. To produce such a mock catalog, the user has to specify a set of properties similar to those given by STUFF, namely the axial ratio, position angle and size of galaxy bulge and disk, respectively, the galaxy magnitude, bulge-to-total magnitude ratio and the galaxy type. In "Mock" mode, these properties are passed to corresponding configuration as input parameters (see SHUFF CONFIGURE TABLE), and will be adopted for all the galaxies internally generated, *i.e.* the mock galaxies have the same magnitude, bulge/disk properties, etc.

The projected 2d positions of galaxies in field of view can be distributed in two ways, random distribution (`POS_MODE=RND`) or on grids (`POS_MODE=RND`). In either mode, the number density $n_{\rm gal}$, in unit of galaxy per arcmin^2, of all the galaxies (both foreground and background) is passed to `MOCK_DENS`. With the number density and field of view size S in unit of arcmin, if the position distribution is random, the total number of galaxies $N_{\rm gal}$ is computed as an integer with fractional part dropped, $N_{\rm gal} = {\rm Int}[n_{\rm gal} \times S^2]$. The galaxies are randomly distributed in the 2d FoV with equal probability at any position, and the random seed is set by `POS_SEED`. If the galaxies are located on grids, the total number of galaxies is slightly larger than what is computed directly from the density and FoV area, $N_{\rm gal} = ({\rm Ceil}[\sqrt{n_{\rm gal}} \times S])^2$, so that each dimension is sampled with the same number of grid points. The "Grid" and "Random" modes are introduced to check the dependence of cluster detection on the 2d spatial distribution of shear signals.

The ellipticity of simulated galaxies can be either fixed or randomly generated. To set the same ellipticity for all the galaxies, the user can set `ELP_MODE=FIX`, and accordingly set the axial ratios and position angles of bulge and disk for all the galaxies with `MOCK_BR, MOCK_BA, MOCK_DR, MOCK_DR`, respectively. This mode is particularly useful when one wants to switches off the ellipticity distribution, and set all the galaxies intrinsically circular. The other mode, `ELP_MODE=RND`, is more realistic, which draws the ellipticity of each galaxy from a 2d Gaussian distribution, with random seed set with `ELP_SEED`. More specifically, the phase of ellipticities are drawn from a uniform distribution in range $[0, 360]$, hence the phases of position angle are in range $[0, 180]$. The module of ellipticity ε are drawn from a Gaussian distribution with the dispersion σ_ε set by `MOCK_ESIG`. By default, we set $\sigma_\varepsilon = 0.3$ (Miralda-Escude 1991a; Tyson & Seitzer 1988; Brainerd et al. 1996). Then the axial ratio r of both bulge and disk is converted from this module by $r = (1 - |\varepsilon|)/(1 + |\varepsilon|)$ for $|\varepsilon| < 1$, and $r = 10^{-4}$ otherwise. Note an ellipse with axial ratio 10^{-4} is almost a line, but this rarely happens as $|\varepsilon| = 1$ is larger than $3\,\sigma_\varepsilon$ in a Gaussian distribution with $\sigma_\varepsilon = 0.3$. The control over the galaxy ellipticity provides a way to reveal the contribution from the galaxies intrinsic ellipticity dispersion to the shear noise in cluster detection.

Finally, the redshift of the galaxies are simulated with several models of redshift distribution, configured by `ZSD_MODE`. The most simple case is the single source redshift mode, (`ZSD_MODE=FIX`), where a single parameter, the source redshift $z_{\rm s}$, is passed to `MOCK_ZPM` input parameter array. In other source redshift modes, galaxies are distributed over the redshift with parametric redshift distribution $n(z)$ models. Currently, SHUFF adopted from NICAEA[‡], the

---

[‡]NICAEA is a numerical routines to calculate cosmology and weak-lensing quantities and functions written by Martin Kilbinger. The code is publicly available at `http://www2.iap.fr/users/kilbinge/nicaea/`

following three types of $n(z)$ models commonly used in lensing analysis,

$$n_{\text{LUD}}(z) \;=\; \frac{1}{N}\left(\frac{1.5\,z}{a}\right)^{b}\exp\left[-\left(\frac{1.5\,z}{a}\right)^{c}\right] \tag{3.1}$$

$$n_{\text{JNB}}(z) \;=\; \frac{1}{N}\frac{z^{a}}{z^{b}+c} \tag{3.2}$$

$$n_{\text{YMK}}(z) \;=\; \frac{1}{N}\frac{z^{a}+z^{ab}}{z^{b}+c} \tag{3.3}$$

where N is the normalization factor, and a, b, c are model parameters passed to `MOCK_ZPM` array. In case only galaxies within a redshift range are desired for simulation, SHUFF also provide the possibility, in "Mock" parametric model mode, to distribute sources according to $n(z)$ only within the redshift range $[z_{\min}, z_{\max}]$ (set by `SZD_ZMIN`, and `SZD_ZMAX`) and otherwise $n(z) = 0$. By default, $z_{\min} = 0.0$ and $z_{\max} = 5.0$. The normalization of $n(z)$ is done for $z \in [z_{\min}, z_{\max}]$. Given the $n(z)$ model, the redshift of each galaxies z_i is obtained by solving the equation of cumulative distribute function (CDF) of $n(z)$

$$\frac{1}{N}\int_{z_{\min}}^{z_i} n(z')\,\mathrm{d}z' = n_i \quad (z_{\min} < z_i < z_{\max}) \tag{3.4}$$

where n_i is a random number drawn from uniform distribution in range $[0, 1]$, with random seed set by `ZSD_SEED`. In order to optimize the efficiency, the CDF of $n(z)$ is pre-calculated and interpolated when solving the above equation. The parametric redshift distribution introduced here will be shown in the later chapter to be an important factor weak lensing cluster detection, since it decides the lensing strength of cluster shear sampled by galaxies distributed in redshift.

So far it can be seen that, the flexibility introduced in SHUFF in simulating the source properties, is mainly focusing on the distribution of position, ellipticity and redshift of the unlensed galaxies. Actually, these modifications can be adopted together with the galaxy properties simulated in STUFF, by setting the mixture mode (`SRC_MODE = MIX`) of source properties in SHUFF. In this special mode, the user needs to explicitly declare for each property of galaxy which type to adopt, "Mock" or "Stuff". For parameters like galaxy type, bulge or disk size, magnitude and bulge-to-total magnitude ratio, input value "-1" stands for "adopting values from STUFF catalog". For ellipticity mode (`ELP_MODE`) and redshift distribution mode (`ZSD_MODE`), there is one more option `STF` which switches off the mock distribution and take only the STUFF one. For position distribution in "Mixed" mode, the galaxy positions are always taken from the input STUFF catalog, since they are already uniformly randomly distributed, and it makes on sense to take galaxies with different redshift and put them onto grids. Finally for using "Mock" redshift distribution in "Mixed" mode, in order to keep the same trend of the redshift dependence of *other* galaxy properties simulated in STUFF, both redshift distributions from input STUFF catalog and internal generated mock one, are first sorted in z, and then updated in order. In addition, while redshift distribution is updated, if STUFF magnitudes are still adopted, they will be changed according to their new luminosity distance computed with the updated redshifts.

3.2.2   Galaxy cluster as lens

Strictly speaking, there are two type of lenses in SHUFF, the galaxy cluster, and the random field of cosmic density perturbation. Since the shear from galaxy cluster is the key, or "shear signal", for cluster detection, while the shear produced by other lenses (either cosmologically, like cosmic shear (hereafter CS), or locally, like intrinsic alignment (hereafter IA)) are considered as "shear noise", the explanation of the simulation of these two types of lens are separated into two subsections. In this subsection, we look at galaxy cluster first.

radial density profile of lens

Galaxy clusters in SHUFF are simulated with triaxial analytical density profile models commonly adopted for dark matter halos. There are two types of halo model supported in SHUFF: NFW and SIS, of which the radial density profile read,

$$\rho_{\text{SIS}}(r) = \frac{\sigma_v^2}{2\pi G} r^{-2} \tag{3.5}$$

$$\rho_{\text{NFW}}(r) = \frac{\delta_c \, \rho_{\text{bg}}(z)}{(r/r_s)^n (1 + r/r_s)^{3-n}}, \tag{3.6}$$

respectively.

For SIS, the one dimensional velocity dispersion σ_v, in unit of km/s, is the only input parameter of its density profile.

For NFW, there are two main parameters, virial mass M_{vir} and concentration c, and two other conventional parameters, the mean density contrast at virial radius Δ_{vir}, and the slope of density profile n, which in literatures are usually set with $\Delta_{\text{vir}} = 200$, and $n = 1$. The characteristic scale r_s in Eq.3.6 is related to concentration by $r_s = r_{\text{vir}}/c$, where the virial radius r_{vir} reads,

$$r_{\text{vir}} = \left(\frac{3 \, M_{\text{vir}}}{4\pi \, \Delta_{\text{vir}} \, \rho(z)} \right)^{-1/3}. \tag{3.7}$$

The normalization factor of the profile δ_c is defined such that the mean density of the halo within r_{vir} is Δ_{vir} times the background density, $\bar{\rho}(r < r_{\text{vir}}) = \Delta_{\text{vir}}\rho_{\text{bg}}$. Explicitly in SHUFF, δ_c is computed with,

$$\delta_c = \frac{\Delta_{\text{vir}} \, c^3}{3} \left(\int_0^c \frac{t^2 \mathrm{d}t}{t^n(1+t)^{3-n}} \right)^{-1}. \tag{3.8}$$

In case the conventional virial density contrast $\Delta_{\text{vir}} \neq 200$, the corresponding r_{200} (the radius within which the mean density is 200 times the background one) is calculated by solving the following equation,

$$\frac{3 \, \delta_c}{(r_{200}/r_s)^3} \int_0^{r_{200}/r_s} \frac{t^2 \mathrm{d}t}{t^n(1+t)^{3-n}} = 200. \tag{3.9}$$

Note that for $\Delta_{\text{vir}} = 200$, $r_{200} = r_{\text{vir}}$, the equation above just returns the definition of δ_c in Eq.3.8. For completeness, the r_{200} of SIS is computed as

$$r_{200} = \sqrt{\frac{3 \, \sigma_v^2}{400\pi \, G \, \rho_{\text{bg}}(z)}} \tag{3.10}$$

In either case, M_{200} is always calculated as $M_{200} = 200 \, \rho_{\text{bg}} \, r_{200}^3 (4\pi/3)$. Note for NFW model, $M_{200} = M_{\text{vir}}$ when $\Delta_{\text{vir}} = 200$.

The extension of cluster in SHUFF is constrained by the "maximum extension density contrast" Δ_{max} (passed to CLS_DMAX), which defines the maximum radius of cluster $\rho(r_{\text{max}}) = \Delta_{\text{max}} \rho_{\text{bg}}(z)$. The contrast Δ_{max} in SHUFF is set as 1 by default. In case it is set much larger and the effective radius of a cluster shrinks, SHUFF takes the compromise $r_{\text{max}} = \text{Max}[r_{\text{max}}, r_{200}]$ to guarantee the extension is at least upto r_{200}.

triaxiality of lens

Cluster density profile model is not restrict to be spherical in SHUFF; triaxial ellipsoid modelling is supported. As the spherical symmetry is broken, more parameters are introduced for the projection of a ellipsoid.

Suppose a triaxial ellipsoid halo is located in its local coordinate system **R**, in which the major, median, minor axis are along **Z, Y, X** coordinate axis, respectively. On the other hand, the line-of-sight from the observer is along **z** axis of the global coordinate system **r**, with **x, y** axes extend in the perpendicular FoV plane. The rotation between two coordinate systems can be described by a set of Euler angles (α, β, γ), so that **r** system is first rotating around **z** by α, then around new **x** by β and finally around new **z** by γ, Fig.3.2, *i.e.* ,

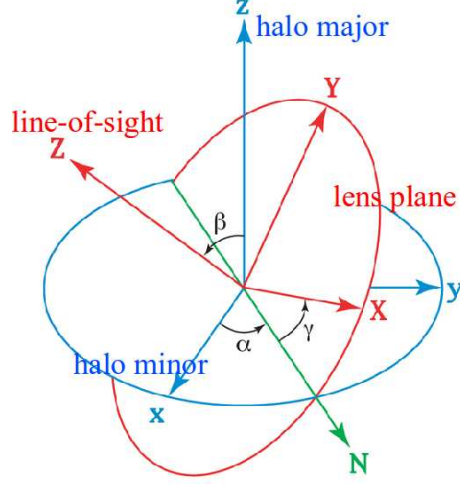Figure 3.2: The illustration of a triaxial halo projection *w.r.t.* the line of sight.

$$
\begin{pmatrix} X \\ Y \\ Z \end{pmatrix} = \begin{pmatrix} \cos\gamma & \sin\gamma & 0 \\ -\sin\gamma & \cos\gamma & 0 \\ 0 & 0 & 1 \end{pmatrix} \begin{pmatrix} 1 & 0 & 0 \\ 0 & \cos\beta & \sin\beta \\ 0 & -\sin\beta & \cos\beta \end{pmatrix} \begin{pmatrix} \cos\alpha & \sin\alpha & 0 \\ -\sin\alpha & \cos\alpha & 0 \\ 0 & 0 & 1 \end{pmatrix} \begin{pmatrix} x \\ y \\ z \end{pmatrix}
$$
$$
= \begin{pmatrix} A_{11} & A_{12} & A_{13} \\ A_{21} & A_{22} & A_{23} \\ A_{31} & A_{32} & A_{33} \end{pmatrix} \times \begin{pmatrix} x \\ y \\ z \end{pmatrix} \tag{3.11}
$$

where the rotation matrix elements A_{ij} read,

$$
\begin{aligned}
A_{11} &= \cos\alpha\cos\gamma - \sin\alpha\cos\beta\sin\gamma \\
A_{12} &= \sin\alpha\cos\gamma + \cos\alpha\cos\beta\sin\gamma \\
A_{13} &= \sin\beta\sin\gamma \\
A_{21} &= -\cos\alpha\sin\gamma - \sin\alpha\cos\beta\cos\gamma \\
A_{22} &= -\sin\alpha\sin\gamma + \cos\alpha\cos\beta\cos\gamma \\
A_{23} &= \sin\beta\cos\gamma \\
A_{31} &= \sin\alpha\sin\beta \\
A_{32} &= -\cos\alpha\sin\beta \\
A_{33} &= \cos\beta
\end{aligned} \tag{3.12}
$$

Thus, the coordinates in local coordinate system of the halo can be related to those in the global coordinate system of the observer through the rotation matrix, *i.e.* $R(X, Y, Z) = R(x, y, z)$. If we further define the axial ratio between the minor/major and median/major as a and b, respectively, the radial distances in two systems are related via,

$$
R^2(x, y, z) = \frac{X^2}{a^2} + \frac{Y^2}{b^2} + Z^2 = D\, z^2 + E(x, y)\, z + F(x^2, y^2) , \tag{3.13}
$$

where,

$$
\begin{aligned}
D &= B_1^2 + B_2^2 + B_3^2 \\
E(x,y) &= 2\,(B_1\,C_1 + B_2\,C_2 + B_3\,C_3) \\
F(x^2, y^2) &= C_1^2 + C_2^2 + C_3^2
\end{aligned}
\tag{3.14}
$$

in which,

$$
\left\{
\begin{aligned}
B_1 &= A_{13}/a \\
B_2 &= A_{23}/b \\
B_3 &= A_{33}
\end{aligned}
\right.
\quad \text{and} \quad
\left\{
\begin{aligned}
C_1\,(x,y) &= (A_{11}\,x + A_{12}\,y)/a \\
C_2\,(x,y) &= (A_{21}\,x + A_{22}\,y)/b \\
C_3\,(x,y) &= A_{31}\,x + A_{32}\,y
\end{aligned}
\right.
\tag{3.15}
$$

Hence, the surface mass density of the halo, projected along $\mathbf{z}$ axis, is simplified as $\Sigma(x,y) = \int \rho(R(x,y,z))\,\mathrm{d}z$, and given the 3d radial density profile of the halo, it is straightforward to calculate. However, in practise, there are two additional points to be noticed.

Firstly, both NFW and SIS density profile are divergent in the center. SHUFF offers two ways to bypass this problem. (A) When the clusters are read in, their positions in the internal projection map are slightly offset with

$$
x_{\mathrm{map}} = \mathrm{Floor}[x_{\mathrm{map}}] + 0.5 \,, \quad y_{\mathrm{map}} = \mathrm{Floor}[y_{\mathrm{map}}] + 0.5 \,,
\tag{3.16}
$$

So that the cluster is always located *between* the sampling grid points, *i.e.* no map grid points fall into the center of clusters. (B) The distances of sampling points around the center are then subjected to the grid spacing. In case when the fine grid is setup, the grid points may sample into very high surface density region and take a global dominating value, which ruins the FFT transformation of the map. In this case, density flattering core is applied in SHUFF, with core radius control by input keyword CLS_RMIN, in unit of kpc at the redshift of cluster. When a point with distance to cluster center $r < r_{\mathrm{min}}$ is sampled, the following threshold is setup,

$$
D = 1 \,, \quad E = 0 \,, \quad F = r_{\mathrm{min}}^2 \,,
\tag{3.17}
$$

so that $R^2(r,z) = z^2 + r_{\mathrm{min}}^2$ is no longer dependent of r, and hence the surface density gets "flattened". Depending on the mass of cluster and resolution of sampling map, $r_{\mathrm{min}} = 10$ kpc is generally sufficient to bypass the problem.

Secondly, the maximum extension of the cluster r_{max} calculated assuming the spherical symmetry now has to be converted into the surface boundary of an ellipsoid. Starting from the limit in R,

$$
R^2(x,y,z) = D\,z^2 + E(x,y)\,z + F(x^2,y^2) \geq r_{\mathrm{max}}^2 \,,
\tag{3.18}
$$

given the 2d position (x,y) where projection is to be done, the lower and upper limits, t_- and t_+ respectively, of integration in z (note here z is in unit of Mpc which is not redshift) can be estimated as,

$$
t_\pm = \frac{-E \pm \sqrt{\Delta}}{2\,D\,r_{\mathrm{max}}}
\tag{3.19}
$$

for $\Delta(x,y) = E^2 - 4\,D(F - r_{\mathrm{max}}^2) > 0$, and $\Sigma(x,y) = 0$ for $\Delta \leq 0$. Note $t_\pm$ is normalized by r_{max} and dimensionless.

With the above two additional considerations, the formulae used in SHUFF, for projection of surface mass density, are explicitly listed below, for NFW and SIS model, respectively.

- triaxial NFW surface mass density (for $\Delta(x,y) > 0$)

$$
\Sigma(x,y) = r_{\mathrm{max}}\,\rho_{\mathrm{bg}}\,\delta_c \int_{t_-}^{t_+} \mathrm{d}t \left(\sqrt{\hat{D}t^2 + \hat{E}t + \hat{F}} \right)^{-n} \left(1 + \sqrt{\hat{D}t^2 + \hat{E}t + \hat{F}} \right)^{n-3}
\tag{3.20}
$$

where dimensionless parameters $\hat{D}, \hat{E}, \hat{F}$ read,

$$\hat{D} = \frac{r_{\max}^2}{r_s^2} D \,, \quad \hat{E} = \frac{r_{\max}}{r_s^2} E \,, \quad \hat{F} = \frac{1}{r_s^2} F \tag{3.21}$$

- triaxial SIS surface mass density (for $\Delta(x, y) > 0$)

$$\Sigma(x, y) = \frac{\sigma_v^2}{2\pi G \, r_{\max}} \int_{t_-}^{t_+} dt \left(\hat{D}t^2 + \hat{E}t + \hat{F} \right)^{-1} \tag{3.22}$$

where dimensionless parameters $\hat{D}, \hat{E}, \hat{F}$ read,

$$\hat{D} = D \,, \quad \hat{E} = \frac{1}{r_{\max}} E \,, \quad \hat{F} = \frac{1}{r_{\max}^2} F \tag{3.23}$$

The surface mass density is then calculated for each grid point in the projection map $\Sigma(x_i, y_j) = \Sigma_{ij}$, and normalized by critical surface density $\Sigma_{\mathrm{cr}}(z_{\mathrm{d}})$ to get the convergence map κ_{ij},

$$\kappa_{ij} \;=\; \frac{\Sigma(x_i, y_j)}{\Sigma_{\mathrm{cr}}(z_{\mathrm{d}})} \;=\; \frac{4\pi \, G}{c^2} D_{\mathrm{d}}(0, z_{\mathrm{d}}) \, \Sigma_{ij} \left\langle \frac{D_{\mathrm{ds}}(z_{\mathrm{d}}, z_{\mathrm{s}})}{D_{\mathrm{s}}(0, z_{\mathrm{s}})} \right\rangle . \tag{3.24}$$

Note that in the last step, we used the relative distance factor $\langle D_{\mathrm{ds}}/D_{\mathrm{s}} \rangle$ averaged over the redshift distribution of the sources $n(z_{\mathrm{s}})$. In the case when the sources are not located on the single source plane, SHUFF introduces flexible configurations for the redshift distribution of sources: as we will show later, a global redshift histogram will be setup, and the average distance factor estimated with that histogram. Here we just remind that when an individual galaxy at redshift z_i is taken into account, a scaling factor $(D_{\mathrm{ds}}(z_i)/D_{\mathrm{s}}(z_i))/\langle D_{\mathrm{ds}}/D_{\mathrm{s}} \rangle$ will be applied to recover the specific κ for that galaxy at redshift z_i.

Since the projected surface mass contour of an ellipsoid is obvious elliptical, SHUFF takes advantage of this symmetry and improves the efficiency of projection computation. Specifically, for each grid point in the convergence map, if its symmetric point on the opposite side of cluster center is already stored with the convergence value, the same value will be shared. This feature also owns to the offset treatment of cluster center in the middle of the grid points. Statistically, only half of the projection plane is calculated.

The last but not the least, during the projection, the background mean density is substract from the cluster density. While subtracting a constant factor from the convergence map will not affect the 2d potential as they are related by 2nd order differential equation (2d Poisson equation), the more practical reason for this treatment is that the convergence field of cosmic shear is a random field fluctuating around 0, which in the real world corresponds to the mean background density. However, adding a projected background density into cosmic shear convergence field is not preferred and not adopted in SHUFF, since it involves the spacing between the lens planes, and also fails the zeropadding of convergence map when transforming it into potential map with FFT. Thus SHUFFtakes the convention that the zeropoint of convergence field is zero, and the projected background density is subtracted from the cluster convergence map.

Like the input source galaxies, a catalog of lenses is passed as input to SHUFF, with the angular position in the field, redshift, triaxial ratios, Euler rotation angles, halo model types and relative parameters for the halo density profile, all configured by user.

3.2.3 shear noises

As mentioned above, SHUFF takes into account the shear noises from cosmic shear (CS) and intrinsic alignment (IA). Given the cosmology and source galaxy redshift distribution, the expected cosmic shear power spectrum at redshift $z = 0$ can be derived. Similar power spectrum of intrinsic alignment can be calculated with the physical IA model.

It seems straightforward to apply the noise shear from its convergence field, which can be realized with one random field, of which the spatial correlation of the amplitudes is consistent with the 2d power spectrum integrated over source redshift distribution $n(z)$ from some maximum redshift (*e.g.* the horizon) to $z = 0$. Once this total convergence field (at $z = 0$) is obtained, the shear field resulting from the convolution of convergence field can be applied to all the galaxies in FoV, distributed in redshift. However there are two potential problems.

First, this approach is exact if all sources are located on a single source plane. In case the galaxies are distributed in redshift, the shear interpolated from the shear map at the position of the galaxy should be scaled according to the lensing efficiency $D_{ds}(z_d, z_s)/D_s(0, z_s)$ specifically for that galaxy at z_s, and the scaling factor is generally different for different z_s. In addition, an equivalent cosmic convergence plane at $z = 0$ switches off the scaling factor for any source redshift as $D_{ds}(0, z_s) = D_s(0, z_s)$. As a result, at the same a specific projection position, the same cosmic shear derived at $z = 0$, is applied to all galaxies along the line-of-sight at different redshift.

Second, in case of intrinsic alignment, by definition, galaxies are *locally* sheared by the underlying gravitational tidal potential at the same redshift of the galaxy. However, projecting all the surface density perturbation to redshift $z = 0$, and then applying the intrinsic shear to all the galaxies along the line-of-sight, is obviously contradicting to its original physical motivation.

Regarding to the above consideration, in SHUFF, 3d to 2d density perturbation projection is done differentially, a series of lens planes are constructed, each of which is one realization of 2d random perturbation field generated from the differential power spectra integrated between lens planes. During this approach, the redshift distribution of source galaxies is embedded into the calculation of power spectrum for each lens plane. In the following, we will first introduce the treatment of source redshift distribution in power spectra calculation, and then the realization of 2d random field.

$n(z)$ for 2d power spectra

The flexibility in modelling the redshift distribution of input unlensed galaxies provided in SHUFF, slightly complicates the treatment of source redshift distribution for power spectra calculation (of CS or IA), which deserves some discussion.

As mentioned in the source properties section, practically there are 3 types of $n(z)$ supported in SHUFF, single source plane (`ZSD_MODE=FIX`), parametric models (`ZSD_MODE=LUD`, `JNB` or `YMK`, for simplicity, any one of the 3 models will be referred as `MOD` hereafter) and histogram bins (`ZSD_MODE=STF`). In order to treat different input cases equally, in SHUFF, there is a global redshift slices spacing strategy, configured by the global range of redshift bins between $[Z_{min}, Z_{max}]$ (set by `GBL_ZMIN` and `GBL_ZMAX`), and number of global redshift bins N_Z (set by `GBL_NBIN`). Thus the global redshift bin size dZ is

$$dZ = \frac{Z_{max} - Z_{min}}{N_Z - 1} \tag{3.25}$$

By default, in SHUFF, 50 global redshift bins are setup in range $z \in [0, 5]$, giving a bin size 0.01 which is generally accurate to sample the redshift of galaxies, compared to the accuracy

in good photometric redshift results $\Delta z_{\text{phot}} \sim 0.05$. This spacing strategy is also used to setup the lens plane slices, which will be discussed later. With global redshift bins constructed, the $n(z)$ is sampled for each bin. In case of single source redshift plane $z = z_s$, the bin values are

$$n(z_i) = n_i = \begin{cases} 1/\mathrm{d}Z & (|z_i - z_s| < \mathrm{d}Z/2) \, , \\ 0 & \text{(otherwise)} \, . \end{cases} \tag{3.26}$$

While for parametric models $n(z)$,

$$n_i = \frac{n\,(z_i + \mathrm{d}Z/2)}{N} \quad \text{with} \quad N = \int_{Z_{\text{min}}}^{Z_{\text{max}}} \mathrm{d}z' n(z') \, .$$

Finally for source redshifts input from STUFF catalog, $n_i = N_i/N_{\text{tot}}/\mathrm{d}Z$.

As the global redshift distribution histogram is built up, the power spectra of cosmic shear $P_{\text{sim}}^{GG}(\ell, z_i)$ and intrinsic alignment $P_{\text{sim}}^{II}(\ell, z_i)$ for each lens plane can be readily calculated. By replacing the integration over comoving distance χ with redshift z via

$$\mathrm{d}\chi = \frac{c}{H_0} \frac{\mathrm{d}z}{E(z)} \, , \tag{3.27}$$

and replacing the integration with summation,

$$P^{GG}(\ell) = \sum_{z_i=Z_{\text{min}}}^{Z_{\text{max}}} P_{\text{sim}}^{GG}(\ell, z_i) \tag{3.28}$$

$$P^{II}(\ell) = \sum_{z_i=Z_{\text{min}}}^{Z_{\text{max}}} P_{\text{sim}}^{II}(\ell, z_i) \tag{3.29}$$

the differential power spectra read,

$$P_{\text{sim}}^{GG}(\ell, z_i) = \left[R_H^{-3}\,\Omega_m^2\, P_\delta^{CS}\,(k(\ell), z_i)\, \Delta z \right] \frac{9}{4} \frac{(1+z_i)^2}{E(z_i)}\, W^2(z_i), \tag{3.30}$$

$$P_{\text{sim}}^{II}(\ell, z_i) = \left[R_H^{-3}\,\Omega_m^2\, P_\delta^{IA}\,(k(\ell), z_i)\, \Delta z \right] X^2 \frac{n^2(z_i)\, E(z_i)}{f_K^2(w(z_i))\, D^2(z_i)} \, , \tag{3.31}$$

where

$$W(z_i) = \int_{z_i}^{z_{\text{max}}} \mathrm{d}z_s n(z_s) \left(f_K'(\chi_i) - f_K'(\chi_s) \frac{f_K(\chi_i)}{f_K(\chi_s)} \right) \, . \tag{3.32}$$

in which $f_K'(\chi)$ is the derivative of trigonometric function $w.r.t.$ the comoving distance χ. The factor in the parenthesis is actually the lens efficiency $D_{\text{ds}}/D_{\text{s}}$ with lens and source redshift z_i and z_s, respectively, so that $W(z)$ is just the $\langle D_{\text{ds}}/D_{\text{s}} \rangle$ weight-averaged over $n(z_{\text{s}})$ of galaxies *behind* the lens ($z_{\text{s}} > z_i$). We have mentioned this averaged distance factor in discussion of cluster convergence, and here the treatment for cosmic convergence field is exactly consistent. As an example, we show in Fig.3.3 the three dimensional power spectra $P_\delta(k, z)$ and two dimensional power spectra $P_{\text{sim}}^{GG}(\ell, z)$, $P_{\text{sim}}^{GG}(\ell, z)$, calculated in SHUFF.

There are several important points to be mentioned about these two explicit formulae used in SHUFF.

First, we take a dimensional check. $R_H = c/H_0$ is in unit of Mpc/h, the 3d wavenumber $k(\ell) = \ell/f_K(w(z_i))/R_H$ has the dimension h/Mpc, and for 3d density perturbation power spectra $[P_\delta] = \text{Mpc}^3/h^3$. Thus the resulting 2d power spectra P_{sim}^{XX} takes the dimension rad^2, as expected from the fact that the Fourier transform of 2d power spectra gives the 2d correlation function $\int \mathrm{d}^2\ell P(|\ell|) \exp[-i\ell\theta] = C(|\theta|)$, which is the dimensionless.
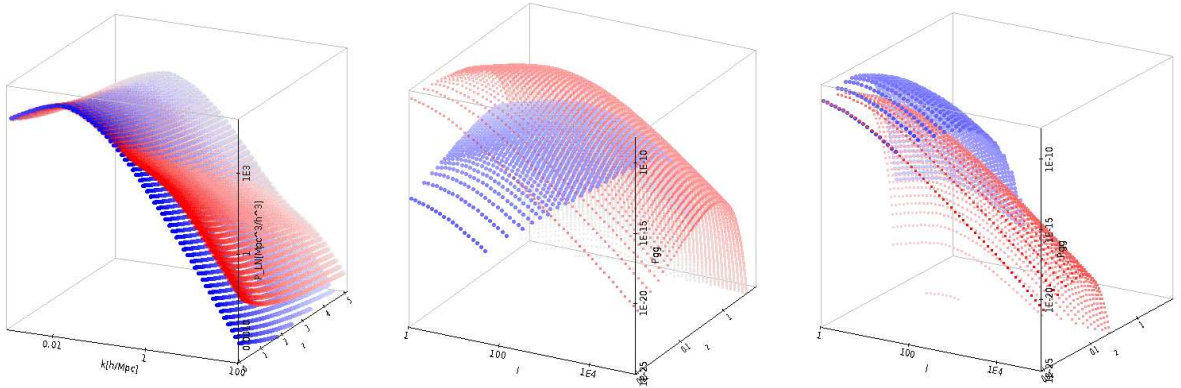
Figure 3.3: The power spectra calculated in SHUFF as a function of redshift. (a) *left panel* $P_\delta(k, z)$ of three dimensional linear (blue) and nonlinear (red) density perturbations; (b) *center panel* two dimensional power spectra of cosmic shear $P_{\text{sim}}^{GG}(\ell, z)$ (red) and intrinsic shear $P_{\text{sim}}^{II}(\ell, z)$ (blue), using $n_{\text{LUD}}(z)$ redshift distribution, with median redshift $a = 1.5$; (c) *right panel* similar to (b) but with median redshift $a = 0.1$.

Second, the 3d density power spectra $P_\delta(k, z)$ is calculated with NICAEA. Given the cosmological parameters, with the transfer function and linearity of cosmological density perturbation power spectrum specified, the 3d density power spectrum $P_\delta(k) \, (\text{Mpc}/h)^3$ can be calculated. Here the code is modified to output a table of 3d density power spectrum, both linear and non-linear, as a function of wavenumber k and redshift z. Such a table is taken as input (with name passed to IDAT_P3D) in SHUFF for the calculation of 2d cosmic shear and intrinsic alignment power spectra, as shown above. Note that after the modification in NICAEA, the 3d power spectra table samples 501 points in redshift z in range $[0.0, 5.0]$, and logarithmically samples 127 points in wavenumber k in range $[10^{-5}, 10^5]$ (h/Mpc), of which the spatial and redshift range and accuracy is sufficient to be used in SHUFF with interpolation.

Third, the right density power spectrum to use. Since the 2d power spectra are used to realize a Gaussian random field, by default, SHUFF uses the linear 3d power spectrum P_δ^{lin} in projection, both for CS and IA power spectra calculation. However, if the user wants to test the effect of projection of a non-linear 3d density power spectrum in the small scale, one can switch off the option CS_LINEAR="N" or IA_LINEAR="N".

Fourth, some controls over IA effects. As suggested in the linear IA model (Hirata & Seljak 2004), the perturbation for intrinsic shear is smoothed in sub-galactic scale, so that the linear power spectrum $P_\delta(k, z)$ has a cutoff $k < k_{\text{max}} = 1h/\text{Mpc}$. In SHUFF, this cutoff is controllable through input parameter IA_KMAX with the suggested cutoff scale as default value. Moreover, the strength amplitude of intrinsic alignment $X = C\rho_{\text{bg}}(z = 0)$ is a dimensionless parameter introduced in the linear IA modelling (Hirata & Seljak 2004). By assuming the intrinsic alignment dominates the low redshift galaxies ellipticity variance, the amplitude is constrained by SuperCOSMOS data (Brown et al. 2002) and is found to be $X = -0.0134$ (Joachimi & Schneider 2009; Bridle & King 2007). Regarding the future updates to the fitting results, the amplitude is set as an input value (IA_FACT) in SHUFF.

Finally, the redshift of lensed galaxies. Note the sources that are lensed, are not those right behind the lens plane, but those further behind with an offset in redshift $z_s > z_i + \Delta z_i$. The offset in redshift is introduced due to the concern that when the source is too close to the lens compared with the distance from the observer to source, the "infinite thin" lens

plane assumption breaks down. To avoid such a case, SHUFF defines the minimum ratio of $(D_{ds}/D_s)_{min}$ (SZD_ZSFRAC) for sources to apply lensing effect. Thus Δz_i is obtained by solving the following equation,

$$\frac{D_{ds}(z_i, z_i + \Delta z_i)}{D_s(0, z_i + \Delta z_i)} = \left(\frac{D_{ds}}{D_s}\right)_{min}. \qquad (3.33)$$

The 2d power spectra $P_{sim}^{GG}(\ell, z_i)$ and $P_{sim}^{II}(\ell, z_i)$ for CS and IA data array are internally stored for the realization of Gaussian random convergence fields. As the redshift sampling of the power spectra is setup with the global redshift binning, the sampling in ℓ can be configured between range P2D_LMIN and P2D_LMAX by P2D_NL sampling points. By default, both CS and IA power spectra are logarithmically sampled with 100 points in range $\ell \in [2.0, 10^7]$, which is found sufficient to cover the FoV of simulation and achieve the desired resolution in small scales.

In Fig.3.3a, for the calculation of non-linear power spectrum, we used the halo model non-linear power spectrum derived by Smith et al. (2003) and the transfer function derived by Eisenstein & Hu (1998). We found that on the small scales and low redshift, the non-linear evolution of the structure formation leads to the deviation from the extrapolation from linear evolution. The scale of deviation grows with redshift, with $k \sim 1\, h\, \mathrm{Mpc}^{-1}$ today, as the scale of galaxy cluster. In the calculation for the two dimensional power spectra of cosmic shear and intrinsic shear, we use the linear power spectrum as shown in the Fig.3.3a, since in SHUFF we realize the density field with Gaussian random field, which assumes the uncorrelated Fourier modes. We also found from Fig.3.3b and Fig.3.3c that the relative strength of cosmic shear and intrinsic shear significantly depends on the redshift distribution of the source galaxies, with the shallower the distribution, the more noise power from intrinsic shear than cosmic shear. The small scale cutoff in the 3d density power spectrum $k_{max} = 1h/\mathrm{Mpc}$ leads to the cutoffs in both plots for the project intrinsic shear power spectra, as introduced in the linear model (Hirata & Seljak 2004).

Realization of random convergence field

For a two dimensional random field $\delta(\boldsymbol{\theta})$, if its Fourier modes $\hat{\delta}(\boldsymbol{\ell})$ are statistically mutual independent, the probability distribution of each mode $\hat{\delta}(|\boldsymbol{\ell}|)$ is Gaussian with dispersion σ^2 given by the power spectrum $P_\delta(|\boldsymbol{\ell}|)$. In other words, starting from a power spectrum, a random field which is fully described by this power spectrum must be a Gaussian random field.

Here we assume no correlation between different Fourier modes of projected two dimensional density perturbation field, and realize the Gaussian random convergence field with its two dimensional power spectrum. The assumption is valid in case the projection is done with three dimensional density field $\delta(\mathbf{x})$ linearly expanded to first order, in which each perturbation mode evolves independently. As the perturbation grows on, second order perturbation in $\delta(\mathbf{x})$ is no longer negligible, then bi-spectrum corresponding to three-point correlation statistics should be considered. However, the bi-spectrum involves the understanding and modelling of the coupling between different Fourier perturbation modes, which is beyond the scope of this thesis. For the current case, with the power spectrum well constructed from the structure formation theory, we consider only the realization of Gaussian random convergence field.

It is worth mentioning that, the power spectra computed in the last subsection are those of the cosmic and intrinsic shear. But it can be easily shown that they are identical with those of the convergence. Since the shear and convergence are second order derivatives of two

dimensional deflection potential, in Fourier space, these relations read

$$\hat{\kappa}(\boldsymbol{\ell}) = \left[\frac{1}{2}(\ell_1^2 + \ell_2^2)\right] \hat{\psi}(\boldsymbol{\ell}), \tag{3.34}$$

$$\hat{\gamma}(\boldsymbol{\ell}) = \left[\frac{1}{2}(\ell_1^2 - \ell_2^2) + \mathrm{i}\,\ell_1\ell_2\right] \hat{\psi}(\boldsymbol{\ell}). \tag{3.35}$$

which leads to $\langle \hat{\kappa}(\boldsymbol{\ell})\hat{\kappa}^*(\boldsymbol{\ell})\rangle = \langle \hat{\gamma}(\boldsymbol{\ell})\hat{\gamma}^*(\boldsymbol{\ell})\rangle$, so that $P_\kappa(\ell) = P_\gamma(\ell)$.

Now we come back to look at how the Gaussian random field is realized from the power spectrum in SHUFF. We first take one of the lens planes and a two dimensional power spectrum, which can be either $P_{\mathrm{sim}}^{GG}(\ell)$ or $P_{\mathrm{sim}}^{II}(\ell)$.

Supppose the field of view of desired convergence map is $L \times L$ in unit of rad^2. We sample the map with a $N \times N$ grid with the spatial resolution $\Delta\theta = L/N$, and denote the convergence value at grid point (m,n) as κ_{mn}, i.e.

$$\kappa_{mn} = \kappa(\theta_{1,m}, \theta_{2,n}) \quad \text{where} \quad \begin{cases} \theta_{1,m} = m\,\Delta\theta & (m = 0, \cdots, N-1) \\ \theta_{2,n} = n\,\Delta\theta & (n = 0, \cdots, N-1) \end{cases}. \tag{3.36}$$

The Fourier transform of the convergence map $\hat{\kappa}_{jk}$ is sampled with on $N \times N$ grid in Fourier domain, with spectral resolution $\Delta\ell = 2\pi/L$,

$$\hat{\kappa}_{jk} = \hat{\kappa}(\ell_{1,j}, \ell_{2,k}) \quad \text{where} \quad \begin{cases} \ell_{1,j} = j\,\Delta\ell & (j = 0, \cdots, N) \\ \ell_{2,k} = k\,\Delta\ell & (k = 0, \cdots, N) \end{cases}. \tag{3.37}$$

The details about discrete Fourier transformation and the layout of Fourier plane are described in Appendix.A.1.

For each Fourier component of the convergence map $\hat{\kappa}_{jk}$, the real and imaginary part are drawn first from standard normal distribution with mean 0 and variance 1,

$$\hat{\kappa}_{jk} = \xi_{jk} + \mathrm{i}\,\eta_{jk} \quad \text{where} \quad \xi_{jk}, \eta_{jk} \sim \mathcal{N}(\mu = 0, \sigma^2 = 1). \tag{3.38}$$

As mentioned above, for a Gaussian random field, the variance of Fourier components $\hat{\kappa}(\ell_{1,j}, \ell_{2,k})$ is only a function of mode $\ell = \sqrt{(\ell_{1,j}^2 + \ell_{2,k}^2)}$, constrained by the power spectrum $P_\kappa(\ell)$,

$$\langle \hat{\kappa}^*(\ell')\,\hat{\kappa}(\ell)\rangle = (2\pi)^2 \delta(\ell - \ell')\,P_\kappa(\ell). \tag{3.39}$$

Thus, the module of $\hat{\kappa}(\ell_{1,j}, \ell_{2,k})$ is rescaled by the power spectrum such that its variance $\sigma^2 = P_k(\ell)$,

$$\hat{\kappa}_{jk} = \sqrt{\frac{P_\kappa(\ell)}{2}}\,(\xi_{jk} + \mathrm{i}\,\eta_{jk}). \tag{3.40}$$

Note a factor of 2 in the square root is introduced as the variance $\langle \xi^2 + \eta^2 \rangle = 2$.

Since the convergence map is real, the Fourier counterpart also has certain symmetries, i.e. $\hat{\kappa}_{N-i,N-j} = \hat{\kappa}_{jk}^*$. In particular, following Fourier components $\hat{\kappa}_{jk}$ deserve careful treatment.

- $\hat{\kappa}_{00} = 0$. Note that during the scaling of random complex number $\hat{\kappa}_{jk}$ according to the power spectrum, $P_\kappa(\ell = 0)$ is not defined, and neither is $\hat{\kappa}_{00}$. However, by definition in Fourier transform, $\hat{\kappa}_{00}$ (D.C.term) corresponds to the sum of the real map, and is a real number,

$$\hat{\kappa}_{00} = \frac{L^2}{N^2} \sum_m^{N-1} \sum_n^{N-1} \kappa_{mn}. \tag{3.41}$$

Thus a random field with 0 mean in the spatial domain, is equivalent to requiring

$$\Re[\hat{\kappa}_{00}] = \Im[\hat{\kappa}_{00}] = 0. \tag{3.42}$$

- $\hat{\kappa}_{0,N-k} = \hat{\kappa}_{0,k}^*$, $\hat{\kappa}_{N-j,0} = \hat{\kappa}_{j,0}^*$. So after the randomization of phase and scaling of module, one has to manually set,

$$\Re[\hat{\kappa}_{N-j,0}] = \Re[\hat{\kappa}_{j,0}] , \qquad \Im[\hat{\kappa}_{N-j,0}] = -\Im[\hat{\kappa}_{j,0}] ; \qquad (3.43)$$
$$\Re[\hat{\kappa}_{0,N-k}] = \Re[\hat{\kappa}_{0,k}] , \qquad \Im[\hat{\kappa}_{0,N-k}] = -\Im[\hat{\kappa}_{0,k}] . \qquad (3.44)$$

- $\hat{\kappa}_{N/2,N-k} = \hat{\kappa}_{N/2,k}^*$, $\hat{\kappa}_{N-j,N/2} = \hat{\kappa}_{j,N/2}^*$. Similarly, one has to manually set,

$$\Re[\hat{\kappa}_{N-j,N/2}] = \Re[\hat{\kappa}_{j,N/2}] , \qquad \Im[\hat{\kappa}_{N-j,N/2}] = -\Im[\hat{\kappa}_{j,N/2}] ; \qquad (3.45)$$
$$\Re[\hat{\kappa}_{N/2,N-k}] = \Re[\hat{\kappa}_{N/2,k}] , \qquad \Im[\hat{\kappa}_{N/2,N-k}] = -\Im[\hat{\kappa}_{N/2,k}] . \qquad (3.46)$$

- $\hat{\kappa}_{0,N/2}, \hat{\kappa}_{N/2,0}, \hat{\kappa}_{N/2,N/2}$ are real, as can be seen above with $j = k = N/2$. Thus, one has to manually nullify the imaginary part, and scale the real part by a factor $\sqrt{2}$ to keep the variance the same as that of the complex number,

$$\Re[\hat{\kappa}_{N/2,0}] = \sqrt{2}\,\Re[\hat{\kappa}_{N/2,0}] , \qquad \Im[\hat{\kappa}_{N/2,0}] = 0 ; \qquad (3.47)$$
$$\Re[\hat{\kappa}_{0,N/2}] = \sqrt{2}\,\Re[\hat{\kappa}_{0,N/2}] , \qquad \Im[\hat{\kappa}_{0,N/2}] = 0 ; \qquad (3.48)$$
$$\Re[\hat{\kappa}_{N/2,N/2}] = \sqrt{2}\,\Re[\hat{\kappa}_{N/2,N/2}] , \qquad \Im[\hat{\kappa}_{N/2,N/2}] = 0 . \qquad (3.49)$$

Finally, the convergence map, realized as a Gaussian random field, is obtained with the inverse Fourier transform,

$$\kappa_{mn} = \frac{1}{L^2} \sum_{j=0}^{N-1} \sum_{k=0}^{N-1} \hat{\kappa}_{jk}\, e^{+i\frac{2\pi}{N}(mj+nk)} . \qquad (3.50)$$

Note the normalization factor here is $1/L^2$ instead of $1/N^2$ as in the DFT forward-backward transform loop. The reason for this is that, FFTW library omits a factor L^2/N^2 in the forward transform and $1/L^2$ in the backward, which reduces to $1/N^2$ after a forward-backward loop. In the current case for realization of random field from the power spectrum, we start from the Fourier domain, so that only $1/L^2$ is needed as the normalization factor, when we apply once the inverse Fourier transform.

In SHUFF, both cosmic and intrinsic convergence field are realized with above scheme. Physically, the same projected surface density field is used in shearing the background galaxies as a effect of comic shear, and shearing the local galaxies as a effect of intrinsic shear. But the shear strengths are different due to the difference in the underlying physical process. With these consideration, in Fourier domain, the same random seed is used in both field for the randomization of the phase (or the real and imaginary part) of $\hat{\kappa}_{jk}$, but the module $|\hat{\kappa}_{jk}|^2$ is scaled according to cosmic and intrinsic power spectra, $P_{\text{sim}}^{GG}(\ell)$ and $P_{\text{sim}}^{II}(\ell)$, respectively. As a result, the spatial random structure (shear pattern) of two fields are kept the same, but the spatial correlation of amplitude (shear strength) in each field are different.

It is worth mentioning that, though the power spectrum of correlation between the cosmic and intrinsic shear P^{GI} can be readily calculated, in SHUFF, this power spectrum is not taken into account to realise an additional random field, since once the cosmic shear upon the background galaxies and intrinsic shear upon the local galaxies are properly applied, the correlation between two shears are automatically introduced.

We show in Fig.3.4 the comparison of the convergence field of galaxy clusters with or without the Gaussian random field representing the large scale density perturbation in the background, derived from the cosmic shear power spectrum. The source redshift is set at $z_s = 2$, the density perturbation field is projected with $0 < z < 2$.
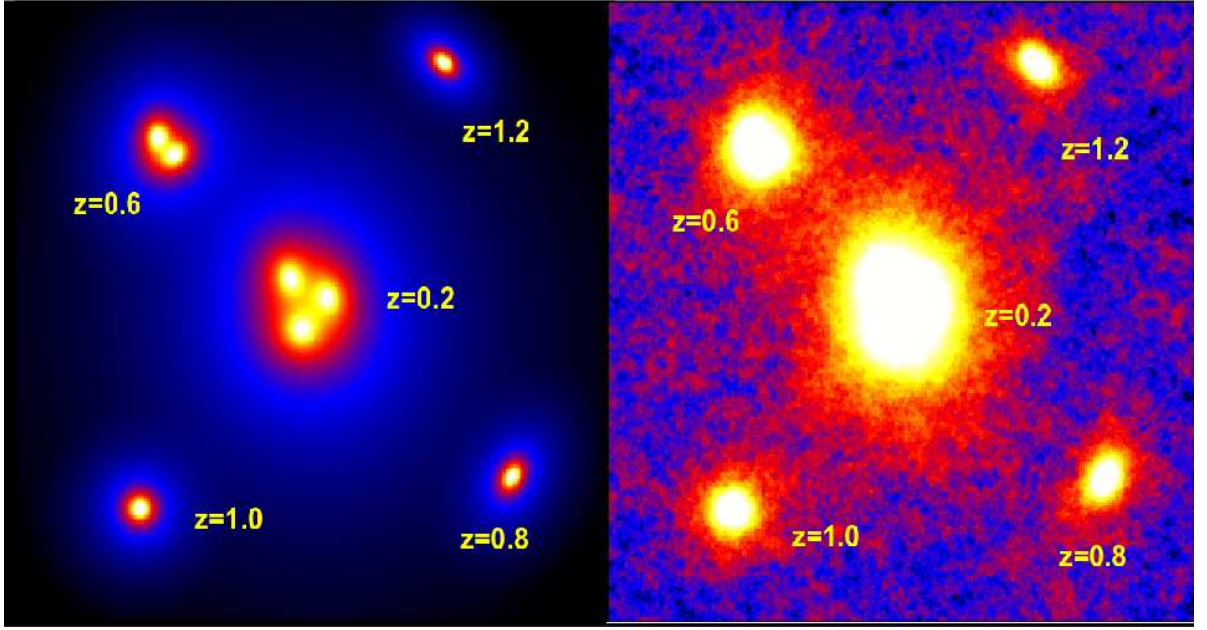
Figure 3.4: The convergence field of galaxy clusters (*left panel*) distributed in redshift as indicated in the plot, and in addition with density perturbation field (*right panel*) in redshift range $0 < z < 2$. For illustration purpose, the source galaxies are located on a single lens plane at $z_s = 2$.

3.2.4 other lens fields from convergence field

Once the convergence field $\kappa(\boldsymbol{\theta})$ is obtained, no matter it contains the projected cluster halos, or the random projected density perturbation field (realized in SHUFF with Gaussian random field), or both, the other lens fields, namely deflection potential field $\psi(\boldsymbol{\theta})$, deflection angle field $\alpha(\boldsymbol{\theta})$ and shear field $\gamma(\boldsymbol{\theta})$ can be readily calculated with the discrete Fourier transform and finite difference kernel of derivative operators.

As shown in Chapter 1, the convergence and shear are both second order derivatives of the two dimensional deflection potential, while the deflection angles are the gradient of the potential, *i.e.* ,

$$\alpha_1 = \partial_1 \psi , \tag{3.51}$$

$$\alpha_2 = \partial_2 \psi , \tag{3.52}$$

$$\kappa = \frac{1}{2}(\partial_1^2 + \partial_2^2)\, \psi , \tag{3.53}$$

$$\gamma_1 = \frac{1}{2}(\partial_1^2 - \partial_2^2)\, \psi , \tag{3.54}$$

$$\gamma_2 = \partial_1 \partial_2 \psi . \tag{3.55}$$

Thus, the procedure will be, to derive the deflection potential field from the convergence field by inverting Eq.(3.53) and then apply the differentiation to the potential field to get the other fields.

In practise, since we are working on discrete maps, we need to apply numerical differentiation, which approximates the derivative operation with the difference between the values estimated on the local points of a finite grid. The method, usually called finite difference method, is useful in solving the numerical differential equations, such as the sets of equations we have at hand Eq.(3.51)-Eq.(3.55). The finite difference of a function at the desired position

is essentially derived from the Taylor expansion of the function. According to the accuracy one wants to achieve, the function can be expanded upto different order, which results in different finite difference kernels for the same derivative operator. In SHUFF, given that the lensing parameter fields are sampled on a fine grid with sufficient number of sampling points (controlled by SIZE_MAP), we use the following finite difference scheme for the first and second order derivatives of the deflection potential, Fig.3.5,

$$\frac{\partial f_{0,0}}{\partial x}{=}\frac{1}{2h}\left(f_{1,0}{-}f_{-1,0}\right){+}O(h^2) \qquad \frac{\partial^2 f_{0,0}}{\partial x^2}{=}\frac{1}{h^2}\left(f_{1,0}{-}2f_{0,0}{+}f_{-1,0}\right){+}O(h^2) \qquad \frac{\partial^2 f_{0,0}}{\partial x\partial y}{=}\frac{1}{4h^2}\left(f_{1,1}{-}f_{1,-1}{-}f_{-1,1}{+}f_{-1,-1}\right){+}O(h^2)$$

Figure 3.5: Finite difference scheme used in SHUFF, from Abramowitz & Stegun (1964) p.883-884.

$$\partial_1 \psi_{mn} \;=\; \frac{1}{2h}(\psi_{m+1,n} - \psi_{m-1,n}) + \mathcal{O}(h^2) \; , \tag{3.56}$$

$$\partial_2 \psi_{mn} \;=\; \frac{1}{2h}(\psi_{m,n+1} - \psi_{m,n-1}) + \mathcal{O}(h^2) \; , \tag{3.57}$$

$$\partial_1^2 \psi_{mn} \;=\; \frac{1}{h^2}(\psi_{m+1,n} + \psi_{m-1,n} - 2\psi_{m,n}) + \mathcal{O}(h^2) \; , \tag{3.58}$$

$$\partial_2^2 \psi_{mn} \;=\; \frac{1}{h^2}(\psi_{m,n+1} + \psi_{m,n-1} - 2\psi_{m,n}) + \mathcal{O}(h^2) \; , \tag{3.59}$$

$$\partial_1 \partial_2 \psi_{mn} \;=\; \frac{1}{4h^2}(\psi_{m+1,n+1} + \psi_{m-1,n-1} - \psi_{m+1,n-1} - \psi_{m-1,n+1}) + \mathcal{O}(h^2) \; , \tag{3.60}$$

where $h = L/N$ is the grid spacing interval and the errors of Taylor expansion are $\mathcal{O}(h^2)$. For the boundary points $m, n = 0, N-1$, strictly speaking, the kernel needs to be modified. However, for the lensing parameter maps in SHUFF, the dimension of map internally calculated during intermediate steps, dubbed "extended map", is always larger than the dimension of the final output map. The extended margin size is controlled by SIZE_EXT. In addition, each extended map is further zeropadded around the borders, with zero padding margin size controlled by SIZE_PAD. Therefore, near the boundary of extended and zeropadded map, the map values are essentially zero, and we do not introduce additional finite difference kernels for the boundary.

With the derivative operators approximated by the finite difference kernel, the differential equations Eq.(3.51)-Eq.(3.55) reduces to linear algebra equations for the map elements, *e.g.*, $\kappa_{mn} = (\partial_1^2 + \partial_2^2)\psi_{mn}/2$, which can be solved with matrix method. However, in SHUFF, the problem is solved with discrete Fourier transform method, which is more efficient.

In the continuous case, the Fourier transform of the derivative of a function $f(\boldsymbol{\theta})$ is,

$$\partial_i f(\boldsymbol{\theta}) = \frac{1}{(2\pi)^2} \int \mathrm{d}^2\ell \, (\mathrm{i}\,\ell_i)\hat{f}(\boldsymbol{\ell})\mathrm{e}^{+\mathrm{i}\boldsymbol{\ell}\boldsymbol{\theta}} \; , \tag{3.61}$$

which shows the derivative operator $\partial/\partial\theta_i$ in Fourier domain is $\mathrm{i}\,\ell_i$, where $i = 1, 2$. Hence, the differential equations Eq.(3.51)-Eq.(3.55) simplifies to basic equations in Fourier domain,

$$\hat{\alpha}_1 = \mathrm{i}\,\ell_1\,\hat{\psi}\,, \tag{3.62}$$

$$\hat{\alpha}_2 = \mathrm{i}\,\ell_2\,\hat{\psi}\,, \tag{3.63}$$

$$\hat{\kappa} = -\frac{1}{2}(\ell_1^2 + \ell_2^2)\,\hat{\psi}\,, \tag{3.64}$$

$$\hat{\gamma}_1 = -\frac{1}{2}(\ell_1^2 - \ell_2^2)\,\hat{\psi}\,, \tag{3.65}$$

$$\hat{\gamma}_2 = -\ell_1\ell_2\,\hat{\psi}\,. \tag{3.66}$$

Analogously, in the discrete case, the Fourier transform of finite difference derivative kernel can be derived. Here we take the equation of $\hat{\kappa}_{jk}$ and $\hat{\psi}_{jk}$ for example. Suppose the physical size of the map is L in radian, and its grid number is $N \times N$. The map element in spatial domain is related with its Fourier counterpart by the inverse DFT,

$$\psi_{mn} = \frac{1}{L^2} \sum_{j=0}^{N-1} \sum_{k=0}^{N-1} \hat{\psi}_{jk} \mathrm{e}^{+\mathrm{i}\frac{2\pi}{N}(mj+nk)}\,, \tag{3.67}$$

$$\kappa_{mn} = \frac{1}{L^2} \sum_{j=0}^{N-1} \sum_{k=0}^{N-1} \hat{\kappa}_{jk} \mathrm{e}^{+\mathrm{i}\frac{2\pi}{N}(mj+nk)}\,. \tag{3.68}$$

While according to the finite difference scheme Eq.(3.58) and Eq.(3.59), the discrete two dimensional Poisson equation Eq.(3.53) becomes,

$$\kappa_{mn} = \frac{1}{2h^2}(\psi_{m+1,n} + \psi_{m-1,n} + \psi_{m,n+1} + \psi_{m,n-1} - 4\,\psi_{mn})\,. \tag{3.69}$$

Substitute κ_{mn}, ψ_{mn} with their Fourier transform Eq.(3.68) and Eq.(3.67), one finds the discrete version of Eq.(3.64),

$$\begin{aligned}\hat{\kappa}_{jk} &= \frac{1}{2h^2}\left[\mathrm{e}^{+\mathrm{i}\frac{2\pi}{N}j} + \mathrm{e}^{-\mathrm{i}\frac{2\pi}{N}j} + \mathrm{e}^{+\mathrm{i}\frac{2\pi}{N}k} + \mathrm{e}^{-\mathrm{i}\frac{2\pi}{N}k} - 4\right]\hat{\psi}_{jk} \\ &= \frac{1}{h^2}\left[\cos\left(\frac{2\pi}{N}j\right) + \cos\left(\frac{2\pi}{N}k\right) - 2\right]\hat{\psi}_{jk}\,. \end{aligned} \tag{3.70}$$

Thus, the Fourier transform of two dimensional Laplacian operator $(\partial_1^2 + \partial_2^2)/2$ in the finite difference scheme is just the part before $\hat{\psi}_{jk}$ on the RHS of above equation, and in the continous limit $N \to \infty$, with the Taylor expansion $\cos(x) \approx 1 - x^2/2 + \mathcal{O}(x^4)$ and the fact that $\ell_{1,2;\,j} = j\Delta\ell = j\,2\pi/L$, it indeed reduces to $-(\ell_1^2 + \ell_2^2)/2$, exactly as in Eq.(3.64).

Similarly, others equations in Eq.(3.51)-Eq.(3.55) can also be discretized, and here we explicitly list them together,

$$\hat{\alpha}_{1,jk} = \frac{\mathrm{i}}{h} \sin\left(\frac{2\pi}{N}j\right)\hat{\psi}_{jk}\,, \tag{3.71}$$

$$\hat{\alpha}_{2,jk} = \frac{\mathrm{i}}{h} \sin\left(\frac{2\pi}{N}k\right)\hat{\psi}_{jk}\,, \tag{3.72}$$

$$\hat{\kappa}_{jk} = \frac{1}{h^2}\left[\cos\left(\frac{2\pi}{N}j\right) + \cos\left(\frac{2\pi}{N}k\right) - 2\right]\hat{\psi}_{jk}\,, \tag{3.73}$$

$$\hat{\gamma}_{1,jk} = \frac{1}{h^2}\left[\cos\left(\frac{2\pi}{N}j\right) - \cos\left(\frac{2\pi}{N}k\right)\right]\hat{\psi}_{jk}\,, \tag{3.74}$$

$$\hat{\gamma}_{2,jk} = \frac{-1}{h^2} \sin\left(\frac{2\pi}{N}j\right)\sin\left(\frac{2\pi}{N}k\right)\hat{\psi}_{jk}\,. \tag{3.75}$$

Once the finite difference kernel of derivative operator is found, it is straightforward to derive the lens parameter maps. Specifically, in SHUFF, the convergence map κ_{mn} is first transformed to Fourier domain, divided by the kernel on the RHS of Eq.(3.73) and Fourier transformed back to obtain the potential map ψ_{mn}. Then the potential map is further Fourier transformed and multiplied by different kernels as shown in Eq.(3.71), (3.72), (3.74), (3.75), and Fourier transformed back produce deflection angle maps $a_{1,mn}$, $a_{2,mn}$ and shear maps $\gamma_{1,mn}$, $\gamma_{2,mn}$, respectively.

There is only one caution for the potential map. $\hat{\psi}_{00}$ is the total sum of potential values in the spatial domain but is not defined in Eq.(3.73), *i.e.*, it can not be constrained by the finite difference scheme. However, we can fix it by comparing the convergence map recalculated from the potential with the original one that we used to calculate potential. We first set it to arbitrary value, *e.g.* $\hat{\psi}'_{00} = 1$. From Eq.(3.69), we note that $\sum \kappa_{mn} = 0$. In other words, the potential field $\psi'(\boldsymbol{\theta})$ calculated with this finite difference scheme corresponds to a convergence field $\kappa'(\boldsymbol{\theta})$ with zero mean,

$$\frac{1}{2} \nabla^2 \psi' = \kappa - \bar{\kappa} \ . \tag{3.76}$$

Compared with the definition $\nabla^2 \psi / 2 = \kappa$, it is clear that after the potential map ψ' is calculated, an additional term is needed to give the correct potential ψ,

$$\psi'(\boldsymbol{\theta}) \to \psi(\boldsymbol{\theta}) = \psi'(\boldsymbol{\theta}) + \frac{\bar{\kappa}}{2} |\boldsymbol{\theta}|^2 \ . \tag{3.77}$$

Thus after applying a two dimension Laplacian, the corrected potential reproduces the original convergence field,

$$\frac{1}{2} \nabla^2 \psi(\boldsymbol{\theta}) = \frac{1}{2} \nabla^2 \psi'(\boldsymbol{\theta}) + \frac{\bar{\kappa}}{4} \nabla^2 |\boldsymbol{\theta}|^2 = \kappa(\boldsymbol{\theta}) - \bar{\kappa} + \bar{\kappa} = \kappa(\boldsymbol{\theta}) \ , \tag{3.78}$$

where we used the Laplacian in polar coordinate $\nabla^2 = \theta^{-1} \partial_\theta (\theta \, \partial_\theta)$ in evaluating $\nabla^2 |\boldsymbol{\theta}|$. In practise, $\bar{\kappa}$ is estimated over extended and zeropadded convergence map, and θ is the radius from the center of the map.

In Fig.3.6, we show the resulting shear and deflection angle map obtained from convergence map, with finite difference scheme and DFT method.
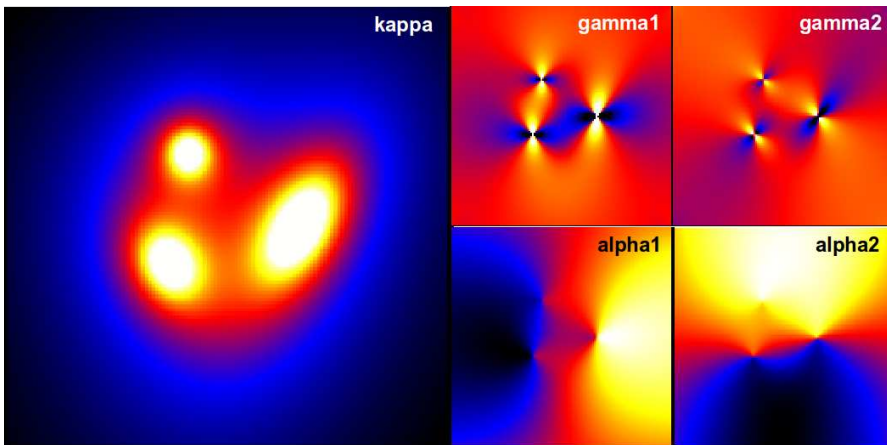

Figure 3.6: Example of conversion between the lens parameter maps with finite difference scheme and DFT method. The convergence map κ of three triaxial NFW cluster halos is on the left, while on top-right and bottom-right are the shear map $\gamma_{1,2}$ and deflection angle maps $\alpha_{1,2}$.

3.2.5 lensing with multiple lens planes

Up to now, we have the source galaxies distributed in the redshift, with desired properties of shape, magnitude, bulge-to-total flux ratio etc. We also have triaxial cluster halos as lenses with analytical density profile and distributed in redshift. In addition, we realized Gaussian random convergence fields from two dimensional power spectra at different redshift, as "lenses" of cosmic and intrinsic shear. Furthermore, given one convergence field, the other lens parameter field, namely deflection potential, deflection angle, and shear field can be readily calculated with finite difference and DFT. What is left is just to setup the lens planes, and successively apply the lensing effects to galaxies behind each lens plane.

SHUFF offers the opportunity to switch on/off the lensing of galaxy clusters, cosmic shear and intrinsic shear independently, so that the output ellipticity catalog of sheared galaxies can be used to investigate the shear from different "lenses". The option `LNS_MODE` can be set to `GCL`, `LSS` or `ALL`, which corresponds to the simulation with lensing effect of galaxy clusters only, LSS only or both, respectively. In case LSS is taken into account, by setting `IAE_MODE` to `LIN` or `OFF`, the user can further switch on or off intrinsic alignment effect.

As mentioned in subsection ($n(z)$ for 2d power spectra), the global redshift bins are constructed in the calculation of CS/IA power spectra at different redshift. The same redshift binning strategy is shared here for the multiple lens planes setup. Among total N_Z global redshift bins, for each bin at redshift z_i ($i = 1, \cdots, N_Z$), the program sets up a lens plane, finds cluster halos within redshift range $[z_i, z_{i+1})$ and checks if LSS is on. For each halo belonging to the lens plane, its convergence map is computed. In case there are multiple halos within the same redshift range, the convergence maps with single halo are summed up. If the LSS is switched on, according to the cosmic convergence power spectrum $P_{\text{sim}}^{GG}(z_i)$ calculated for that lens plane, a Gaussian random field is realized as the cosmic convergence field of LSS. Then it is added into the convergence map of cluster halo(s). Note the random seed i_{rand} for realization of random field for each lens plane is chosen as a function of the lens plane sequence number i, $i_{\text{rand}} = i_0 + i$, where i_0 is the global random seed for LSS random fields set with input `LSS_SEED`. Thus, if one wants to change the randomization of LSS random fields in all the lens planes, only one input i_{rand} needs to be updated. The convergence map containing projected cluster halos and density perturbation is used to generate the deflection angle and shear maps, with finite difference kernel and discrete Fourier transform method mentioned in the last section. With these lens parameter maps at hand, SHUFF applies three effects in gravitational lensing, deflection, magnification and shear.

To deflect the position of galaxies behind the lens, one needs two dimensional deflection angle map α_{ij} but defined on the source galaxy plane. However, what we calculated from the convergence map are the deflection angle map defined on the grids of the lens plane, $\boldsymbol{\alpha} = \boldsymbol{\alpha}(\boldsymbol{\theta})$. In other words, for the moment we only know that, if an image is observed at position $\boldsymbol{\theta}$, its original position (source position) is at $\boldsymbol{\beta}(\boldsymbol{\theta}) = \boldsymbol{\theta} - \boldsymbol{\alpha}(\boldsymbol{\theta})$ on the lens plane. But in practise, what we have is the position of original source galaxy $\boldsymbol{\beta}$ on the source plane, thus we need to invert the lens equation to get the image position $\boldsymbol{\theta}$ after the deflection with deflection angle $\tilde{\boldsymbol{\alpha}}(\boldsymbol{\beta})$ defined as a function of source position, *i.e.* $\boldsymbol{\theta}(\boldsymbol{\beta}) = \boldsymbol{\beta} + \tilde{\boldsymbol{\alpha}}(\boldsymbol{\beta})$. In SHUFF this inversion of lens equation is solved with following grid mapping method, *c.f.* Fig.3.7.

We start with deflection angle maps α_1 and α_2 defined on the lens plane, and we pick up one grid box with four vertices A, B, C, D on the neighbouring grid points. Since each vertex indicates an image position on the lens plane and we have the deflection angles α_1 and α_2 defined on the vertex, its source position can be found directly. We denote the source positions as A', B', C', D'. Of course, they may not be on the grid as $\boldsymbol{\alpha}$ is generally non zero, but now we have the deformed grid box defined on the source plane. With this deformed box, an algorithm is used to search for the source plane grid points within the deformed box. Once
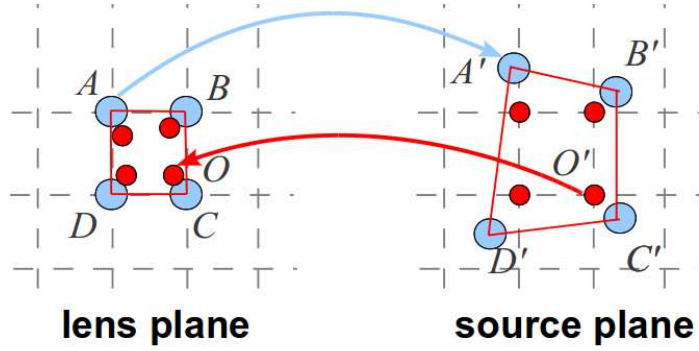
Figure 3.7: The illustration of lens equation inversion. See text for details.

such a grid point is found, *e.g.* O', its *relative* position within the deformed box on source plane is mapped to the *relative* position O inside the undeformed grid box on the lens plane. Finally, the deflection angle value α_1 and α_2 at position O is interpolated from the values on the vertices A, B, C, D, and assigned to the grid position O' on the source plane. In this way, the deflection angle values on the grid of source plane are updated one by one which results in a deflection angle map defined on the source plane, as we denoted $\boldsymbol{\alpha}(\boldsymbol{\beta})$ above.

Note that the mapping we used above is only valid for the conformal transform, *i.e.* without any foldings or cusps. In the strong lensing region, a box can be deformed in such a way that its vertices get overlapped or folded, which fails the conformal point-to-point mapping we used above. We check for each point on the lens plane grid, the value of convergence κ and reduced share $\mathbf{g} = \boldsymbol{\gamma}/(1-\kappa)$ are compared to the strong lensing threshold defined by the input `WL_KMAX` and `WL_RGMAX`, respectively. For those grid points with κ or $\mathbf{g}$ above threshold, we first flag them on the lens plane, and we use no grid mapping by setting the deflection angles to zero. As a by-product of this checking approach, we also obtain a strong-or-weak lensing (S/W) flag map $\zeta(\boldsymbol{\theta})$ defined on the lens plane. This S/W flag map is further used to determine whether a weak lensing effect will be applied to a galaxy in that region, as we will explain right after.

Once the deflection angle map $\boldsymbol{\alpha}(\boldsymbol{\beta})$ defined on the source plane is obtained, we apply lensing effects on the galaxies with redshift behind that of the lens plane by an offset $z_\mathrm{s} > z_\mathrm{d} + \Delta z$, as we have explained before. For each of these galaxies with position $\boldsymbol{\beta}_\mathrm{s}$, its deflection angle $\boldsymbol{\alpha}(\boldsymbol{\beta}_\mathrm{s})$ is interpolated from the map and scaled by a distance factor related to its redshift, since the convergence is computed for sources on the effective source plane with $D_\mathrm{ds}(z_\mathrm{eff})/D_\mathrm{s}(z_\mathrm{eff}) = \langle D_\mathrm{ds}/D_\mathrm{s} \rangle$, and the new (deflected) position is estimated by,

$$\boldsymbol{\theta}_\mathrm{s} = \boldsymbol{\beta}_\mathrm{s} + \boldsymbol{\alpha}(\boldsymbol{\beta}_\mathrm{s}) \frac{D_\mathrm{ds}(z_\mathrm{s})/D_\mathrm{s}(z_\mathrm{s})}{\langle D_\mathrm{ds}/D_\mathrm{s} \rangle} \ . \tag{3.79}$$

At the image position $\boldsymbol{\theta}_\mathrm{s}$ within the grid box on the lens plane, if none of the four vertices of the box is flagged as "strong lensing point" in the flag map $\zeta(\boldsymbol{\theta})$, then for that galaxy to be lensed, the convergence $\kappa(\boldsymbol{\theta}_\mathrm{s})$ and $\mathbf{g}(\boldsymbol{\theta}_\mathrm{s})$ reduced shear at the position of the (deflected) galaxy is interpolated from the convergence and reduced shear maps, respectively, and scaled by the same distance factor accounting for the redshift of the galaxy as for the deflection angle.

The shape of galaxy in SHUFF is elliptical, so that it can be described in three equivalent ways, each of which involves 3 independent parameters. The common description for an elliptical is the major axis length a, axial ratio r and the position angle θ, which we denote here as the "shape space" $\mathcal{S}(a, r, \theta)$. Alternatively, an ellipse can also be described by a complex ellipticity $\boldsymbol{\varepsilon} = \varepsilon_1 + \mathrm{i}\,\varepsilon_2$ and the area ω, which we denote as the "ellipticity space" $\mathcal{E}(\varepsilon_1, \varepsilon_2, \omega)$.

The mapping between $\mathcal{S}$ and $\mathcal{E}$ is,

$$\varepsilon_1 = \frac{1-r}{1+r}\cos 2\theta \,, \tag{3.80}$$

$$\varepsilon_2 = \frac{1-r}{1+r}\sin 2\theta \,, \tag{3.81}$$

$$\omega = a^2 r \,. \tag{3.82}$$

The last, given the surface brightness profile of a galaxy $I(\theta)$, the elliptical shape of the profile can also be described by the second moments, which we denote as "moments space" $\mathcal{Q}(Q_{11}, Q_{22}, Q_{12})$. Since the moments Q_{11}, Q_{22}, Q_{12} stand for the rms σ^2 of the flux *w.r.t.* x, y, and $x = y$ axis, respectively, they are related to the parameters in shape space by,

$$Q_{11} = a^2 \left(\cos^2 \theta + r^2 \sin^2 \theta \right) \,, \tag{3.83}$$

$$Q_{22} = a^2 \left(\sin^2 \theta + r^2 \cos^2 \theta \right) \,, \tag{3.84}$$

$$Q_{12} = a^2 (1 - r^2) \cos \theta \sin \theta \,. \tag{3.85}$$

Note that there is a scaling factor between Q_{11}, Q_{22}, Q_{12} and a according to definition of size given the surface brightness profile $I(\theta)$, *e.g.* for Gaussian profile, the size corresponding to Full-Width-at-Half-Maximum (FWHM) is $a = 2\sqrt{2 \ln 2}\,\sigma$, so that the scaling factor is $2 \ln 2$. However, for a galaxy before and after the lensing, the definition for the size remains the same, so that we adopt the convention that the scaling factor is unit. Thus, we obtained the transform between the three representations $\mathcal{S}, \mathcal{E}, \mathcal{Q}$ of the same ellipse.

The shear and magnification effects on a galaxy is easily expressed in $\mathcal{E}$-space, *i.e.* in the weak lensing regime, the ellipticity and area of a galaxy reads,

$$\varepsilon = \frac{\varepsilon_0 + \mathbf{g}}{1 + \mathbf{g}^* \, \varepsilon_0} \,, \tag{3.86}$$

$$\omega = \frac{\omega_0}{(1-\kappa)^2 (1 - |\mathbf{g}|^2)} \,, \tag{3.87}$$

where ε_0 (or ω_0) and ε (or ω) stand for the ellipticity (or area) before and after the lensing, respectively.

The input and output galaxy shape is described in $\mathcal{S}$-space, *i.e.* the radius, axial ratio and the position angle of bulge and disk, individually. To obtain the shape of the whole galaxy from that of its bulge and disk components, it is straightforward to combine the moments of both components,

$$Q_{ij} = k \, Q_{ij}^{\mathrm{b}} + (1 - k) \, Q_{ij}^{\mathrm{d}} \,, \tag{3.88}$$

where k is the bulge-to-total flux ratio and $Q_{ij}, Q_{ij}^{\mathrm{b}}$ and Q_{ij}^{d} are the second moments of the total, bulge and disk, respectively. Once the total moment is obtained, since the bulge-to-total flux ratio is unaffected by the gravitational lensing, the decomposition from the total galaxy moments to that of its bulge and disk components follows exactly the same way.

With the above relations derived, the shear and magnification effect is applied in SHUFF as follows. Take a galaxy to be lensed in $\mathcal{S}$-space, transform the shape to $\mathcal{Q}$-space to combine the moments of bulge and disk, transform to $\mathcal{E}$-space to apply the shear and magnification from the convergence $\kappa(\boldsymbol{\theta}_{\mathrm{s}})$ and reduced shear $\mathbf{g}(\boldsymbol{\theta}_{\mathrm{s}})$ interpolated from the maps, transform back to $\mathcal{Q}$-space to decompose it into moments of bulge and disk, and finally transform to $\mathcal{S}$-space and save the shape information in memory.

All the procedure above shows the deflection, magnification and shear effect of a single lens plane, applied on all the background galaxies distributed in redshift. The same procedure is successively repeated for all the lens planes available within range $z \in [Z_{\mathrm{min}}, Z_{\mathrm{max}}]$ in an

order from high-z to low-z, c.f. Fig.3.8. Each time after the lensing effect is applied, the shape parameters of all the galaxies are stored internally in the memory as the update original shape, ready for the next lensing events. In this way, the successive lensing of multiple lens planes with continuous distributed source galaxies is realized in SHUFF.
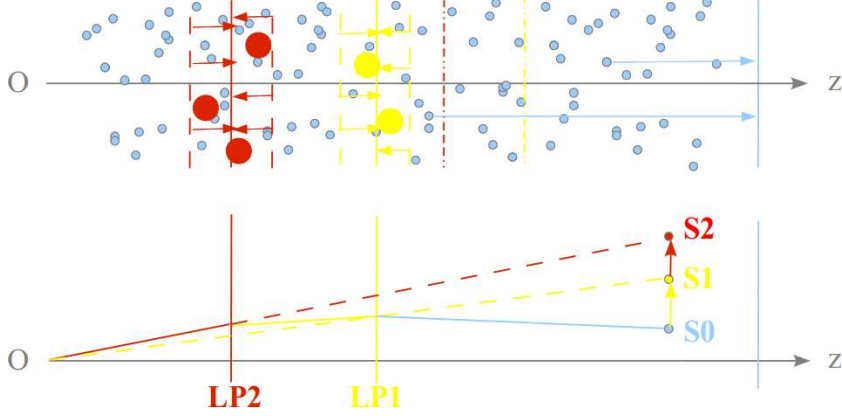

Figure 3.8: The illustration of successive lensing with multiple lense planes in SHUFF. In the upper panel, halos and density perturbation field are first projected into the lens planes, and the convergence map and other lensing parameter maps are calculated for a effective single redshift source plane at z_{eff}, shown as the blue line on the right. For each galaxy, the deflection angle and shear is applied after scaled by the relative lensing strength as in Eq.3.79. In the lower panel, the lensing effects are applied in order from high z to low z, where each time, the previously lensed galaxy is taken as a new source to apply the next lensing.

Note that once a galaxy falls in the strong lensing region of one lens plane, it is not lensed any more, and marked with "S/W" flag 2 in the final output, while those are lensed at least once are flagged 1, and the rest (not lensed) are flagged 0. The area of strong lensing region depends on the threshold of strong lensing for the convergence and reduced shear, and the mass of the halo as lens. But generally speaking, it is small, where at most some tens of galaxies per square degrees are finally marked with "S/W" flag equals 2.

So far we only discuss the gravitational lensing effect implemented in SHUFF from the cosmic convergence of cluster halos and Gaussian random field as large scale structure. The intrinsic shearing and clustering effect is only slightly different from it. If intrinsic shearing effect is also switched on with option IAE_MODE, on each lens plane, the convergence map of cluster halos and LSS are also computed, but stored in memory separately from that of cosmic convergence map. Here we remind that in case of the intrinsic convergence of the random field, the phase of the Fourier components is the same as that of the cosmic convergence of the random field, so that the structure in the spatial domain remains the same. Only the module of the Fourier components are scaled according to the intrinsic convergence power spectra $P_{\mathrm{sim}}^{II}(z_i)$. Hence the amplitude of random field is different from that in the cosmic convergence field, as the later is also related to the source distribution while the former is sensitive only to the number density of the local galaxies between the lens planes. Once the convergence field is computed, the similar deflection angle and reduced shear maps are derived and applied to the local galaxies. Obviously here there is no mapping between the lens plane and source plane and deflection angle calculated are negative due to the physics of clustering of objects towards the local mass concentration. The intrinsic shear at the position of galaxy that is "deflected" (or clustered) is interpolated from the reduced intrinsic shear map. And finally the intrinsic shear is applied to the ellipticity. Compared with multiple lens planes lensing scheme mentioned above, there is only one additional shear effect applied to the local galaxies between

the lens planes.

3.3   Example of SHUFF simulation

Here we briefly show a few examples of one SHUFF simulation, with 1 deg^2 field of view, and the multiple triaxial NFW halos at different redshift as in Fig.3.4, but different sources properties, and lensing effects.

We apply first the lensing of the halos in Fig.3.4 to a mock catalog, with all the "circular" source galaxies at $z_s = 2$, distributed on the grid, Fig.3.9. The convergence contours are in red, and as can be seen from the zoomed-in panels, the lensing effects, *i.e.* the deflection, magnification and distortion, in such case are spectacular .
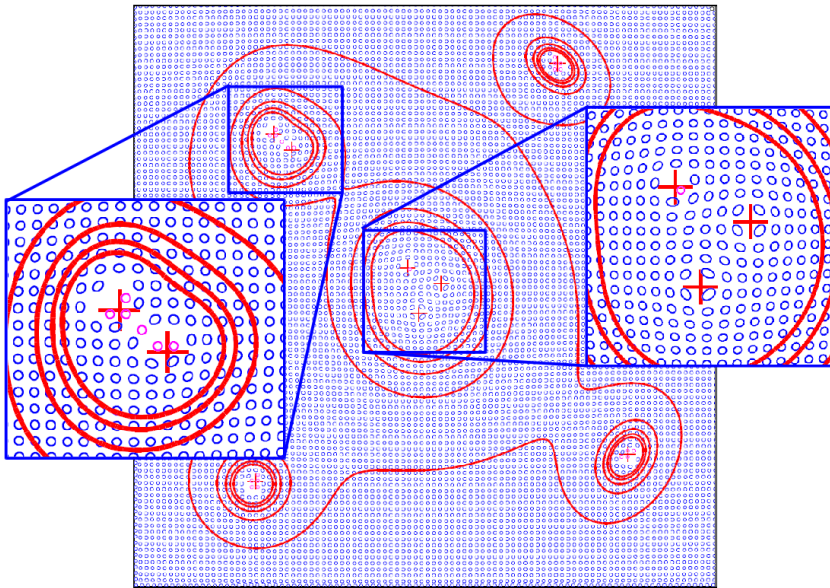

Figure 3.9: SHUFF simulation result with the same halos in Fig.3.4 and circular mock galaxies at $z_s = 2$. The field of view is 1 square degree.

Now we apply the same catalog of halos to a STUFF catalog distributed in redshift, with median redshift $z_m = 1.5$, and produce a noise-free image with SKYMAKER, Fig.3.11. As we introduced the intrinsic ellipticity, and the redshift distribution of the galaxies, the weak lensing effects needs to be estimated statistically rather than just by eye.

The comparison of the gravitational cluster shear and intrinsic alignment effect is shown in Fig.3.11, which is a zoomed view of the central 3 halos with redshift $z = 0.2$. The source galaxies are randomly distributed but set circular for demonstration purpose. The galaxies in the left panel are background galaxies located at redshift $z = 2.0$, while those in the left panel are local galaxies at the same redshift as the halos. As expected, the background galaxies ellipticities are anticorrelated with the ellipticities of local galaxies.

3.4   Output of SHUFF simulation

There are two main outputs from SHUFF simulation. The first one is a catalog of lensed galaxies, in the same format as the STUFF catalog. The second output is a master catalog of galaxies, in which for each galaxy, all the input/output properties are logged. In addition, such a check catalog contains a flag indicating whether a galaxy is weakly lensed, or in the
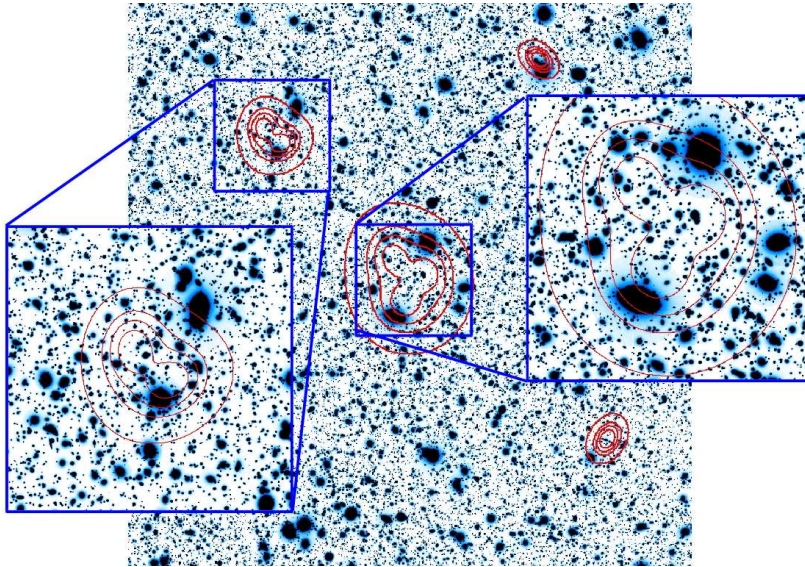
Figure 3.10: SHUFF simulation result with the same halos in Fig.3.9 but sources galaxies from STUFF simulation and distributed in redshift with median $z_m = 1.5$. The field of view is 1 square degree.

strong lensing region (thus not lensed), or not lensed as those in the foreground. Optionally, the projected total convergence map, and the lensing parameter maps such as convergence, shear, deflection angle, etc., of all the lens planes can be outputted in FITS format. For multiple lens planes, the FITS image is a multiple extension FITS (MEF) file, in which each lens plane is an extension which contains the lens plane redshift in the FITS extension header, and can be displayed in ds9 with `ds9 -medatacube` option. Finally, the region files of input galaxies, output galaxies and cluster halos are also saved. The regions of galaxies are elliptical contours representing the ellipticity and size (thus magnitude) of all the galaxies, while the region file for the cluster halos marks the position of all the halos with redshift labelled. For more information about the usage of the program, we refer the reader to Appendix A.

The abundant outputs are designed in the program mainly for the following purposes.

On the one hand, the output lensed galaxy catalog can be used by SKYMAKER to produce an image with additional the instrumental effects and realistic noises, as we have already shown one example in Subsection 3.2.1. Similarly the input catalog can also be used to make a lens-free image. With both of the images, one can apply the shape measurement method such as KSB, and estimate the limit when the cluster shear in the galaxies can still be correctly measured, given the noise level introduced by SKYMAKER. With the check catalog, it is also possible to compare the ellipticity of galaxies in the catalog with the one measured in the image, in order to calibrate the method of shape measurement and PSF correction. With the region files, one can directly see in the image, what is the shape and size of the galaxy originally in the catalog, which gives a direct estimate of the noise level in the image.

On the other hand, the check catalog contain the ellipticity information of all the galaxies. One can directly take it as the output of a "noise-free" shape measurement, and apply the cluster detection method with the catalog. Without the errors in the shape measurement, it is possible to see the intrinsic limit of the detection of galaxy cluster with weak lensing. Of course, the convergence maps of each lens plane can be used to compare with the detection map as a calibration of the cluster detection method, which we will discuss in detail in the next chapter. In addition, the convergence and other maps can also be taken as reference maps for
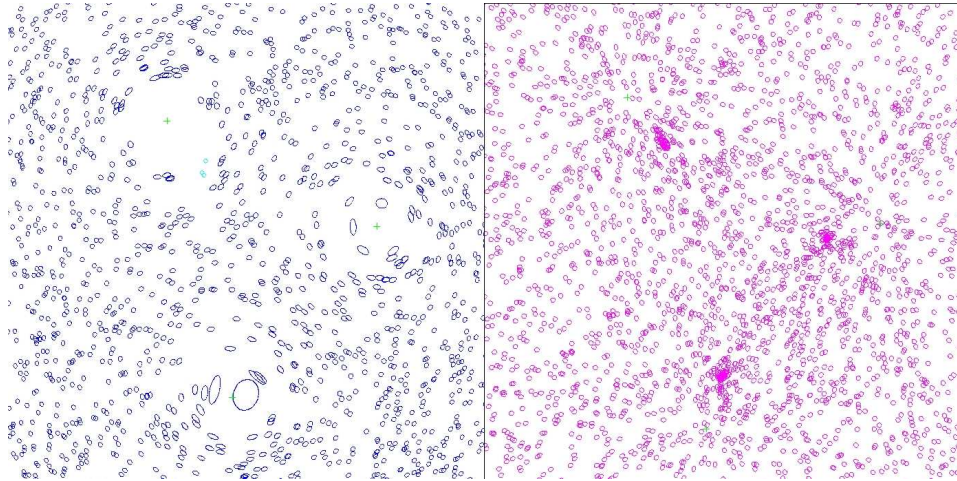
Figure 3.11: Comparison of cluster shear (*the left panel*) with background galaxies at $z_s = 2$, and intrinsic alignment effect (*the right panel*) with local galaxies at $z_s = 0.2$. The halos are the central three ones in Fig.3.11 with $z = 0.2$, indicated with green crosses.

calibrating the mass reconstruction method, which we have not used in the current work.

Lastly, with the cluster detection, we can measure the mass of the detected cluster. As we have all the properties of the cluster halos in the simulation logged, we can also check the accuracy of cluster mass estimation from weak lensing, and investigate the effect of halo triaxiality and substructures on the accuracy.

'

Chapter 4

Filtering detection of weak lensing cluster

In this chapter, we will discuss in practise, from the measured the ellipticities of the galaxies in the image, how the cluster of galaxies can be detected with the filtering method. We will first review the filters available in the literature in Sec.4.1. Then we will introduce the mathematical description of the principle of optimal filtering in Sec.4.2, followed by its application to cluster detection in Sec.4.3. Finally in Sec.4.4, the detailed numerical implementation of the optimal filtering in LensFilter is described. The result of optimal filtering detection applied to the Shuff simulation and real data will be discussed in Section 4.6.

4.1 S-statistics filters in the literature

In Chapter 2, we have defined the convergence as the surface mass density. Since the convergence and shear are both the second order derivative of the deflection potential, it can be shown that the aperture mass $M_{\mathrm{ap}}(\boldsymbol{\theta})$ at position $\boldsymbol{\theta}$ can be derived from the tangential shear field $\gamma_{\mathrm{t}}(\boldsymbol{\theta})$ convolved with a filter $\Psi(|\boldsymbol{\theta}|)$ (Schneider 1996),

$$M_{\mathrm{ap}}(\boldsymbol{\theta}) = \int \mathrm{d}^2\theta' \, \gamma_{\mathrm{t}}(\boldsymbol{\theta}';\boldsymbol{\theta}) \, \Psi(|\boldsymbol{\theta} - \boldsymbol{\theta}'|) \,, \tag{4.1}$$

where $\gamma_{\mathrm{t}}(\boldsymbol{\theta}';\boldsymbol{\theta})$ is the tangential component of the shear at the position $\boldsymbol{\theta}'$ with respect to $\boldsymbol{\theta}$, and filter $\Psi(|\boldsymbol{\theta}|)$ is a function of radius only, whose form can be chosen arbitrary in principle. Thus $M_{\mathrm{ap}}(\boldsymbol{\theta})$ can be interpreted as the total amount of radially weighted tangential shear around the fiducial position $\boldsymbol{\theta}$. Since in absence of cluster lens, and assuming the (tangential) share is not correlated $\langle \gamma_{\mathrm{t}}(\boldsymbol{\theta}')\gamma_{\mathrm{t}}(\boldsymbol{\theta})\rangle = \delta(|\boldsymbol{\theta}' - \boldsymbol{\theta}|)$, we have $\langle M_{\mathrm{ap}}\rangle = 0$, and the variance of $M_{\mathrm{ap}}(\boldsymbol{\theta})$ reads (Kruse & Schneider 1999),

$$\begin{aligned} \sigma^2(M_{\mathrm{ap}}(\boldsymbol{\theta})) &= \langle M_{\mathrm{ap}}^2\rangle - \langle M_{\mathrm{ap}}\rangle^2 = \langle M_{\mathrm{ap}}^2\rangle \\ &= \frac{1}{n^2}\int \mathrm{d}^2\theta \langle \gamma_{\mathrm{t}}\gamma_{\mathrm{t}}\rangle(\boldsymbol{\theta})\Psi^2(|\boldsymbol{\theta}|) \,. \end{aligned} \tag{4.2}$$

Thus, the S/N ratio of the aperture mass at fiducial point $\boldsymbol{\theta}$ can be defined as $S(\boldsymbol{\theta}) = M_{\mathrm{ap}}(\boldsymbol{\theta})/\sigma(M_{\mathrm{ap}}(\boldsymbol{\theta}))$, which is called S-statistics (Schirmer 2004), and its two dimensional graphical representation is called S-map, which is equivalent to the distribution of mass concentration. We will extensively use the S-map as the detection map of the galaxy clusters. In practise, the shear is sampled with galaxy ellipticity and in the weak lensing regime, the tangential ellipticity ε_{t} is on average an unbiased estimator of the tangential shear γ_{t}. Hence, the

signal and noise of S-statistics defined in Eq.(4.1) and Eq.(4.2) can be discretised as,

$$M_{\mathrm{ap}} = \frac{1}{n} \sum_i \varepsilon_{\mathrm{t}i} \, \Psi_i \,, \tag{4.3}$$

$$\sigma^2(M_{\mathrm{ap}}) = \frac{1}{2n^2} \sum_i |\varepsilon_i|^2 \Psi_i^2 \,, \tag{4.4}$$

where we used $\langle \varepsilon_{\mathrm{t}}^2 \rangle = |\varepsilon|^2$.

Since Ψ can be chosen with arbitrary function with only a lose constrain that its equivalent counterpart for the filtering of convergence field should be compensated (Schneider & Bartelmann 1997), its function can be chosen such that it optimizes the detection of galaxy cluster. In literature, a number of filters were proposed for this purpose.

Intuitively, since the signal of shear is from the galaxy cluster, the filter was adopted to possess the tangential shear profile of the cluster desired to be detected, $Q(\theta) \propto \gamma_{\mathrm{t}}(\theta)$ (Schneider 1996; Weinberg & Kamionkowski 2002). The pioneer approach of parameterizing the filter is done by Schneider et al. (1998) with the filter,

$$\Psi_{\mathrm{POLY}}(x) = \frac{6x^2}{\pi \theta_{\mathrm{ap}}^2}(1 - x^2)H(1 - x) \,, \tag{4.5}$$

where $x = \theta/\theta_{\mathrm{ap}}$ is defined as fraction of the filter size θ_{ap} and $H(x)$ is the Heaviside step function. This polynomial filter was originally proposed for cosmic shear analysis but also used then for detection of dark matter halos (Erben et al. 2000; Schirmer et al. 2004).

Later on, Padmanabhan et al. (2003) took an analytical approximation of the filter function for the detection of NFW halos,

$$\Psi_{\mathrm{PAD}}(x) = \frac{2\ln(1+x)}{x^2} - \frac{2}{x(1+x)} - \frac{1}{(1+x)^2} \,, \tag{4.6}$$

which was further modified by Hennawi & Spergel (2005) by multiplying a Gaussian window function with an empirical size to suppress the cosmic shear on the large scale.

As the shear profile of spherical NFW halo can be analytically calculated (Wright & Brainerd 2000; Bartelmann 1996), Schirmer (2004) derived a new analytical filter function accordingly for the NFW halo,

$$\Psi_{\mathrm{NFW}}(x) = \begin{cases} \frac{4(3y^2-2)}{y^2(y^2-1)\sqrt{1-y^2}} \operatorname{arctanh}\sqrt{\frac{1-y}{1+y}} + \frac{4}{y^2}\ln\frac{y}{2} + \frac{2}{1-y^2} & (y < 1) \\ \frac{10}{3} - 4\ln 2 & (y = 1) \\ \frac{4(3y^2-2)}{y^2(y^2-1)\sqrt{y^2-1}} \arctan\sqrt{\frac{y-1}{1+y}} + \frac{4}{y^2}\ln\frac{y}{2} + \frac{2}{1-y^2} & (y > 1) \end{cases} \,, \tag{4.7}$$

with $y = x/x_c$ and x_c is the size of the filter. Due to the computational complexity as a result of the case distinction, this filter is simplified (Schirmer et al. 2004) as,

$$\Psi_{\mathrm{TANH}}(x) = \frac{1}{1 + e^{6 - 150x} + e^{-47 + 50x}} \frac{\tanh(x/x_{\mathrm{c}})}{x/x_{\mathrm{c}}} \,, \tag{4.8}$$

keeping the same feature that it overweights the inner regions and suppresses the outer one. The x_c is empirically found to be 0.1 by Hetterscheidt et al. (2005). The new feature in Eq.(4.8) is that the divergence center is alleviated as $Q(x \to 0) \propto x$, and the box function in the first part on the right smoothly suppresses 10% innermost and outermost of the aperture, underweight the outer region where the tangential ellipticity of galaxies is dominated by the

cosmic shear, and the central region where the number density of background galaxies drops quickly, and strong lensing effects dominates.

Apart from the parameterization of filter with simple mathematical functions above, another different approach was proposed by Maturi et al. (2005), which takes into account the correlations between ellipticities due to the cosmic shear by large scale structure. The filter, which is called optimal filter, is derived from the spectral analysis of the Fourier transform of cluster shear signal $\hat{\tau}$ and power spectrum of cosmic shear P_γ and intrinsic ellipticity dispersion P_σ as noise in the Fourier space,

$$\Psi_{\mathrm{OPT}}(\boldsymbol{\ell}) = C\frac{\tau(\boldsymbol{\ell})}{P_N(\boldsymbol{\ell})} \quad \text{with} \quad C^{-1} = \int \mathrm{d}^2\ell \frac{|\hat{\tau}(\boldsymbol{\ell})|}{P_N(\ell)} \,, \tag{4.9}$$

where the noise power spectrum $P_N = P_\gamma + P_\sigma$. The optimal filtering has been applied to the Garching-Bonn Deep Survey (GaBoDS) observed with Wide-Field-Imager (WFI) camera mounted on MPG/ESO 2.2m telescope, with a low median redshift of galaxies $z_s \leq 1$, and detected 14 halos in 18 deg^2, with 5 already known clusters confirmed (Maturi et al. 2007). It was also applied to the ray tracing simulation of cluster weak lensing, and found reliable detection of dark matter halos, 50% completeness for halo mass $M \geq 7 \times 10^{13} M_\odot$, and 100% completeness for $M \geq 2 \times 10^{14} M_\odot$ (Pace et al. 2007). But the source galaxies redshift are fixed at $z_s = 2$ in the simulation, relatively higher than most ground-based weak lensing observation can achieve.

The optimal filtering detection is a promising method for cluster detection, as it avoids the empirical parameterization and scaling of the filter, and takes into account the noise properties in the data. In this work, we adopt this approach for our investigation of the limit of cluster detection with weak lensing. In order to fully adapt the method to the lensing data with specific conditions, especially the various effects realized with SHUFF, we generalized the method to include also the effect of the intrinsic alignment shear noise, and the continuous redshift distribution of the source galaxies. The improved method is implemented in the software LENSFILTER, which generates the S-map with an input ellipticity catalog, in an configurable but automatic way.

In the following sections, we will first introduce the optimal filtering principle, and then describe its implementation in LENSFILTER.

4.2   the principle of optimal filtering

In fact, the idea of the optimal filter is not new. The minimizing of variance according to the noise power spectrum in the data, is a mathematical variational problem similar to Wiener filtering (Wiener 1949; Rybicki & Press 1992; Zaroubi et al. 1995). Within astrophysics, it was already implemented in fields other than lensing, in astrophysics, (see e.g. Haehnelt & Tegmark 1996). Here we demonstrate the problem and its solution in general.

Any data contains not only signal but also noise. If we know the spatial dependence of the signal and noise in advance, it is possible to build a filter to optimize the signal and minimize the noise in the data. In this section, we introduce the principle of filtering techniques.

In two dimensional case, the measured data $D(\boldsymbol{\theta})$ can be expressed in terms of signal $S(\boldsymbol{\theta})$ and noise $N(\boldsymbol{\theta})$, assuming that there is no strong correlation between the two components,

$$D(\boldsymbol{\theta}) = S(\boldsymbol{\theta}) + N(\boldsymbol{\theta}) = A\,\tau(\boldsymbol{\theta}) + N(\boldsymbol{\theta}) \,. \tag{4.10}$$

In the last step, we rewrite the signal as the normalized spatial function $\tau(\boldsymbol{\theta})$ scaled by the amplitude (normalization factor) A, so that

$$\int \mathrm{d}^2\theta\, S(\boldsymbol{\theta}) = A \int \mathrm{d}^2\theta\, \tau(\boldsymbol{\theta}) = A \,. \tag{4.11}$$

For noise properties, we assume that the mean value is zero $\langle N(\boldsymbol{\theta}) \rangle = 0$, and isotropic, *i.e.* the spatial correlation of noise is only a function of scale $\langle N(\boldsymbol{\theta}')N(\boldsymbol{\theta}) \rangle = C(|\boldsymbol{\theta}' - \boldsymbol{\theta}|)$. As far as the topics in this thesis are considered, these two assumptions are well satisfied, *e.g.* the noise in the ellipticity due to random distribution and orientation of galaxies, or the cosmic shear induced ellipticity, which is isotropic and on average zero. The variance of the noise can be easily defined in the Fourier space, with the noise power spectrum

$$\langle \hat{N}^*(\boldsymbol{\ell}')\hat{N}(\boldsymbol{\ell}) \rangle = (2\pi)^2 \delta(\boldsymbol{\ell}' - \boldsymbol{\ell}) \, P_N(\ell) \, . \tag{4.12}$$

Now we can build a filter according to the spatial dependence of the signal $\tau(\boldsymbol{\theta})$, that we want to optimize, and the power spectrum of the noise $P_N(\boldsymbol{\ell})$, that we want to filter. Suppose we have a filter $\Psi(\boldsymbol{\theta})$, and take a position of interest as origin $\boldsymbol{\theta} = 0$. The estimate E of the signal amplitude A at this position *after* the filtering reads:

$$E = \int \mathrm{d}^2\theta' D(\boldsymbol{\theta}')\Psi(\boldsymbol{\theta}') = \frac{1}{(2\pi)^2} \int \mathrm{d}^2\ell \, \hat{\Psi}(\boldsymbol{\ell}) \, \hat{D}^*(\boldsymbol{\ell}) \, , \tag{4.13}$$

where in the last step, we substitute $\Psi(\boldsymbol{\theta})$ with its Fourier transform, and make use of the definition of the conjugation of Fourier transform of data $\hat{D}^*(\boldsymbol{\ell})$. Analogously, we have

$$E^2 = \frac{1}{(2\pi)^4} \int \mathrm{d}^2\ell \int \mathrm{d}^2\ell' \, \hat{\Psi}^*(\boldsymbol{\ell}) \, \hat{\Psi}(\boldsymbol{\ell}') \, \hat{D}(\boldsymbol{\ell})\hat{D}^*(\boldsymbol{\ell}') \, . \tag{4.14}$$

Since the Fourier transform of the data is $\hat{D}(\boldsymbol{\ell}) = A\hat{\tau}(\boldsymbol{\ell}) + \hat{N}(\boldsymbol{\ell})$, thus $\hat{D}(\boldsymbol{\ell})\hat{D}^*(\boldsymbol{\ell}')$ can be expanded as

$$\hat{D}(\boldsymbol{\ell})\hat{D}^*(\boldsymbol{\ell}') = A^2\hat{\tau}(\boldsymbol{\ell})\hat{\tau}^*(\boldsymbol{\ell}') + \hat{N}(\boldsymbol{\ell})\hat{N}^*(\boldsymbol{\ell}') + A\,\hat{\tau}(\boldsymbol{\ell})\hat{N}^*(\boldsymbol{\ell}') + A\,\hat{\tau}^*(\boldsymbol{\ell}')\hat{N}(\boldsymbol{\ell}) \, . \tag{4.15}$$

Now the estimate E and E^2 averaged over all positions in the data can be readily shown as,

$$\langle E \rangle = \frac{A}{(2\pi)^2} \int \mathrm{d}^2\ell \, \hat{\Psi}(\boldsymbol{\ell}) \, \hat{\tau}^*(\boldsymbol{\ell}) \, , \tag{4.16}$$

$$\langle E^2 \rangle = \langle E \rangle^2 + \frac{1}{(2\pi)^2} \int \mathrm{d}^2\ell \, \hat{\Psi}^*(\boldsymbol{\ell})\hat{\Psi}(\boldsymbol{\ell})P_N(\ell) \, , \tag{4.17}$$

where we used noise power spectrum defined in Eq.(4.12) and the fact that $\langle \hat{N}(\boldsymbol{\ell}) \rangle = 0$, so that last two terms in Eq.(4.15) average out.

In order to construct the optimal filter, we first define the *bias*, $b = \langle E - A \rangle$, which gives the average error in the estimated amplitude, and *noise*, $\sigma^2 = \langle (E - A)^2 \rangle$, which gives the rms deviation from the true amplitude A. With Eq.(4.16) and Eq.(4.17), the bias and the noise can be explicitly written as functions of $\Psi(\boldsymbol{\theta})$,

$$b\left(\hat{\Psi}(\boldsymbol{\ell})\right) = \langle E \rangle - A = A\left[\frac{1}{(2\pi)^2} \int \mathrm{d}^2\ell \, \hat{\Psi}(\boldsymbol{\ell}) \, \hat{\tau}^*(\boldsymbol{\ell}) - 1\right] \, , \tag{4.18}$$

$$\sigma^2\left(\hat{\Psi}(\boldsymbol{\ell})\right) = \langle E^2 \rangle - 2\langle E \rangle A + A^2 = (\langle E \rangle - A)^2 + \langle E^2 \rangle - \langle E \rangle^2$$

$$= b^2\left(\hat{\Psi}(\boldsymbol{\ell})\right) + \frac{1}{(2\pi)^2} \int \mathrm{d}^2\ell \, \hat{\Psi}^*(\boldsymbol{\ell})\hat{\Psi}(\boldsymbol{\ell})P_N(\ell) \, . \tag{4.19}$$

The optimal filter $\Psi(\boldsymbol{\theta})$ is obtained by requiring that it is unbiased $b = 0$ and the noise σ is minimized. The problem reduces to finding a $\hat{\Psi}(\boldsymbol{\ell})$ which minimizes $\sigma(\hat{\Psi})$ with constraint $b(\hat{\Psi}) = 0$, which can be solved by introducing a Lagrangian multiplier λ, and minimizing

$L(\hat{\Psi}, \lambda) = \sigma^2(\hat{\Psi}) + \lambda\, b(\hat{\Psi})$. Applying the derivative with respect to λ and functional derivative with respect to $\hat{\Psi}$, the equation for optimal filter $\hat{\Psi}(\boldsymbol{\ell})$ is obtained,

$$\frac{\partial L}{\partial \lambda} = 0 \implies \frac{1}{(2\pi)^2} \int d^2\ell\, \hat{\Psi}(\boldsymbol{\ell})\, \hat{\tau}^*(\boldsymbol{\ell}) = 1\, , \tag{4.20}$$

$$\frac{\partial L}{\partial \hat{\Psi}} = 0 \implies \frac{1}{(2\pi)^2} \int d^2\ell\, \left[\lambda\, A\, \hat{\tau}^*(\boldsymbol{\ell}) + \hat{\Psi}^*(\boldsymbol{\ell}) P_N(\boldsymbol{\ell}) \right] = 0\, . \tag{4.21}$$

Eq.(4.21) shows that by minimizing the noise σ, the profile of filter in Fourier domain is found to be $\hat{\Psi}(\boldsymbol{\ell}) = C\,\hat{\tau}(\boldsymbol{\ell})/P_N(\ell)$, which makes sense as it just overweights the wavelength ℓ where the signal is dominating over the noise in Fourier domain. The normalization factor C can be derived from the constraint $b = 0$, Eq.(4.20),

$$C = \left[\frac{1}{(2\pi)^2} \int d^2\ell'\, \frac{\hat{\tau}(\boldsymbol{\ell}')\hat{\tau}^*(\boldsymbol{\ell}')}{P_N(\ell')} \right]^{-1}\, , \tag{4.22}$$

and the optimal filter and the signal-to-noise ratio S/N after filtering, for the position of interest, read,

$$\hat{\Psi}(\boldsymbol{\ell}) = C\, \frac{\hat{\tau}(\boldsymbol{\ell}')}{P_N(\ell)}\, , \quad \text{S/N} = \frac{A}{\sigma} = \frac{A}{\sqrt{C}}\, . \tag{4.23}$$

Note that the normalization factor is just the minimized noise $\sigma^2 = C$.

4.3   Filtering technique for cluster detection

With the mathematical description of the filtering technique introduced in the last section, now we are ready to implement this technique in the cluster detection with weak gravitational lensing.

The data we have now is the measured ellipticities of all the galaxies distributed in the image. For each point in the field of view, the ellipticity $(\varepsilon_1, \varepsilon_2)$ of a galaxy at two dimensional distance θ away from the point with position angle ϕ can be reprojected into the relative tangential direction $\varepsilon_{\rm t}$ and radial direction $\varepsilon_{\rm x}$,

$$\begin{pmatrix} \varepsilon_{\rm t} \\ \varepsilon_{\rm x} \end{pmatrix} = -\begin{pmatrix} \cos 2\phi & \sin 2\phi \\ -\sin 2\phi & \cos 2\phi \end{pmatrix} \begin{pmatrix} \varepsilon_1 \\ \varepsilon_2 \end{pmatrix}\, . \tag{4.24}$$

Since the complex shear(ellipticity) has spin 2, an ellipse with $g_1 > 0$ ($\varepsilon_1 > 0$) is along the x-axis while $g_1 < 0$ ($\varepsilon_1 < 0$) is along y-axis. Similarly, an ellipse with $g_2 > 0$ ($\varepsilon_2 > 0$) is along the $x = y$ direction while $g_2 < 0$ ($\varepsilon_2 < 0$) is along $x = -y$ direction. After the above reprojection, an ellipse with $\varepsilon_{\rm t} > 0$ ($\varepsilon_{\rm t} < 0$) is along the tangential (radial) direction *w.r.t.* the point of interest, usually dubbed as E-mode, while an ellipse with $\varepsilon_{\rm x} > 0$ ($\varepsilon_{\rm x} < 0$) is oriented along the $45°$ ($135°$) away from the tangential direction, dubbed as B-mode.

The signal we want to detect is the tangential component of the reduced shear as a function of the distance from the cluster center $g(\theta)$. Note that gravitational shear has only E-mode, *i.e.* $\varepsilon_{\rm x} = 0$. Given the cluster density profile, which can be parameterized with virial mass and concentration parameter in case of NFW halo, or with velocity dispersion in case of SIS halo, and the redshift of the cluster and its lensing strength related to the redshift distribution of the source galaxies, the reduced shear profile can be readily calculated.

Regarding the shear induced ellipticity of galaxy, the noise in the ellipticity comes from various reasons. The most obvious one is the error in the shape measurement and PSF correction. For faint galaxies with low S/N ratio, the shape measurement can be very noisy. If the

PSF is varying significantly in the image or it is nearly constant but with large anisotropies, and there are few stars available for the PSF correction, then the PSF induced artificial shear becomes a serious contamination in the ellipticities from which we want to estimate the cluster shear. In addition, the galaxies are not intrinsically circular. Statistically speaking, their ellipticities are on average zero but with a dispersion which is usually approximated with a Gaussian distribution. Furthermore, averaging over very large scale, their orientations are randomly distributed. This is called intrinsic ellipticity which we have simulated with SHUFF. Note that all these noises contribute in not only the tangential component of the ellipticity but also the cross component.

There are further some noise components in the ellipticity of galaxies which are motivated by the local or global physics mechanisms. Locally, between the physical scale of galaxy and cluster of galaxies, the ellipticity of galaxies are affected by the local gravitational tidal field, which stretches the galaxies towards the mass concentration center, producing an effect which we simulated with intrinsic shear in SHUFF. Globally, the background galaxies are tangentially sheared by the intervening cosmological density perturbations along the line of sight, which we simulated with cosmic shear in SHUFF. Note for these two types of shear noises, they affect only the tangential (or radial) components of the ellipticity.

With so many noise components in the shear, the real gravitational shear signal produced by galaxy cluster, which we are interested in, should be strong enough to give high S/N ratio for the detection of cluster. In other words cluster detection with weak lensing method is limited only to those massive ones and of which the shear signal is "deeply" sampled by the distant galaxies. However, given the knowledge of the noise properties, *e.g.* in terms of their power spectra, the detection can be optimized so that we can approach the limit as close as possible by making use of the most information we can obtain. This is exactly the philosophy in applying the filtering techniques in cluster detection. Below we will discuss the implementation in detail.

4.4   LENSFILTER **implementation**

The filtering detection is implemented in the program I developed, LENSFILTER. It shares several modules with SHUFF, as this is just a reverse game to find out the lens you put into the simulation or from real data.

The main workflow of LENSFILTER is as follows. It reads from input a catalog of galaxy positions, redshifts and ellipticities. From the properties of the background galaxies and modeling of cosmic and intrinsic shear, different noise power spectra are calculated in Fourier space, as the noise part in the filter construction. Then it computes the cluster shear profile according to the target cluster configured for detection, and adjusts the shear according to the lensing strength given the redshift distribution of the lensed galaxies, which finishes the signal part of the filter construction. The filter is then built with the signal and noise analysis in the Fourier domain, transformed to spatial domain for a digital filter. Finally, the digital filter is convolved with the ellipticity field and results in a detection S/N map as output. We will go through these steps one by one, and abbreviate some similar steps which are already discussed in SHUFF.

4.4.1   Source configuration

The input galaxy catalog, parsed in with keyword `IDAT_GLS`, contains the galaxy positions x, y, ellipticity $\varepsilon_1, \varepsilon_2$ and a weight w assigned to the ellipticity by the error estimation in the shape measurement. Optionally the catalog can also contain the redshift of each galaxy z

mainly from photometric redshift estimation, by setting the keyword `SZD_MODE` to `BIN`. Alternatively, without the redshift for each galaxy, the user may configure a model of expected redshift distribution $n(z)$, `SZD_MODE = LUD`, `JNB`, `YMK` or just a single redshift `FIX`. The models supported in LENSFILTER are the same as those in SHUFF, with model parameters passed to keyword array `SZD_NZPRM`. For single redshift case, the source plane redshift z_s can be set as a single parameter to `SZD_NZPRM`.

The galaxies within the FoV are first filtered on input, with ellipticity $|\varepsilon| < 1.0$. In case the input catalog contains the galaxy redshift information, the user can set a redshift range of interest with keywords `SZD_ZMIN` and `SZD_ZMAX`, so that only those within the range are selected for further analysis. For redshift distribution modeling or single source plane case, there is no further selection of galaxies in the redshift and LENSFILTER assumes all input galaxies are within this range. After these selections, the weight of each galaxy is normal by the total weight of all the galaxies to be analyzed, and for each galaxy both of the ellipticity components are weighted by the normalized weight.

Then a global redshift histogram is setup and normalized for later power spectra calculation. The range of histogram is set by the keyword `GBL_ZMIN` and `GBL_ZMAX`, while the number of bins is set by `GBL_NBIN`, similar to those in SHUFF. Note for redshift distribution model case, the histogram is normalized only within the desired redshift range between `SZD_ZMIN` and `SZD_ZMAX`. By default, the user selected redshift range is identical to the range of global redshift histogram.

Given the global redshift histogram $n_i = n(z_i)$ and the target cluster redshift z_{gcl} as input (see below), the lensing strength $D_{\mathrm{ds}}/D_{\mathrm{s}}$ averaged over the redshift distribution is readily calculated and the equivalent source plane redshift is found with,

$$\frac{D_{\mathrm{ds}}(z_{\mathrm{gcl}}, z_{\mathrm{eff}})}{D_{\mathrm{s}}(0, z_{\mathrm{eff}})} = \left\langle \frac{D_{\mathrm{ds}}(z_{\mathrm{gcl}}, z_i)}{D_{\mathrm{s}}(0, z_i)} \right\rangle_{z_i > z'_{\mathrm{gcl}}} , \tag{4.25}$$

where $z'_{\mathrm{gcl}} = z_{\mathrm{gcl}} + \Delta z$. Δz is an offset decided according to the minimum ratio of $D_{\mathrm{ds}}/D_{\mathrm{d}}$ for a galaxy to be lensed by a cluster at D_{d}, configured by keyword `GCL_ZSFRAC` as in SHUFF.

Once the equivalent source plane redshift is found, if galaxy redshifts are provided, the ellipticity of each galaxy is scaled from the redshift of the galaxy to the redshift of common source plane,

$$\varepsilon' = \varepsilon \, \frac{D_{\mathrm{ds}}(z_{\mathrm{gcl}}, z_{\mathrm{eff}})}{D_{\mathrm{s}}(0, z_{\mathrm{eff}})} \frac{D_{\mathrm{s}}(0, z_i)}{D_{\mathrm{ds}}(z_{\mathrm{gcl}}, z_i)} . \tag{4.26}$$

This is mainly due to the concern that galaxies at different redshift behind the lens are sheared with different strength, even for those at the same projected position in the sky. In order to sample the shear of the cluster on the common equivalent source plane, the galaxy ellipticities need to be scaled. For catalog without redshift information, no redshift scaling is applied and one can only assume that all the galaxies are on a common source plane, which is not true especially when the clusters are at the high redshift, and the difference in shear due to the difference in source redshift is significant. On the other hand, since scaling of redshift modifies the ellipticity directly, it is apparent that the accuracy of redshift estimation is also crucial for the detection of high-z clusters.

After scaling the ellipticity of all galaxies to a common equivalent source plane, the galaxy ellipticities are sampled with a fine mesh in order to get the shear sampling on the grid of the source plane. The sampling grid point number is set to the dimension of the final output detection map, with the keyword `MAP_NPIX`. The ellipticities in the mesh are averaged, and in case there is no galaxies falling in the mesh, the grid value is zero. The number of non-zero grid points are used to calculate the practical number density of background galaxies, which is further used to estimate the noise level of random spatial distribution of galaxies with intrinsic

ellipticity dispersion (see below). Note that practical number density can be lower than that estimated from the galaxies in the catalog, if some of the galaxies are too close to each other or the mesh size is too large. But it serves as a better estimation of galaxy number density since if the galaxies are not homogeneously distributed in the field of view, or in the extreme case a large number of galaxies are located at almost the same position, the density after the binning is lower than the one before, and represents the true definition of density. Finally the ellipticity map of ε_1 and ε_2 components are stored internally for later filtering convolution.

4.4.2 Noise configuration

As shown in the filtering analysis section, for spatial isotropic noise with zero average, the important estimate of noise properties in filter construction is the power spectrum of noise in the Fourier domain. We decomposite the noise power spectrum into four components: the intrinsic ellipticity dispersion P_σ, the cosmic shear $P^{GG}(\ell)$, the intrinsic shear $P^{II}(\ell)$ and the correlation between cosmic and intrinsic shear $P^{GI}(\ell)$.

We have discussed the calculation of cosmic and intrinsic shear power spectra in the discussion for SHUFF simulation. The only difference here for building a filter is that, each power spectrum is summed over redshift from $Z_{\max}$ to $Z_{\min}$, and is only a function of wavenumber ℓ in Fourier domain. With the global redshift histogram setup, these two power spectra are readily calculated.

For the power spectrum $P^{GI}(\ell)$ of the correlation between cosmic and intrinsic shear, we did not formulate it for SHUFF, since there we only need to build the different type of lenses, and the correlation of their shear is automatically realized when the shears are applied to different source galaxies. However, for the filtering method, since we take from input catalog the ellipticities of galaxies in all the redshift range, different correlation are presented in the data. Therefore once the intrinsic shear is introduced, one has to deal with the correlation between the shear in foreground and background galaxies. Given the formulas of $P^{GG}(\ell)$ and $P^{II}(\ell)$, $P^{GI}(\ell)$ can be easily derived as,

$$P^{GI}(\ell) = \sum_{z_i = Z_{\min}}^{Z_{\max}} \left[R_H^{-3} \, \Omega_m^2 \, P_\delta^{IA}\left(k(\ell), z_i\right) \, \Delta z \right] (3X) \frac{n(z_i)(1 + z_i)}{f_K^2(w(z_i)) \, D(z_i)} \, W(z_i) \,, \qquad (4.27)$$

where all the variables are defined as the same as in Eq.(3.30) and Eq.(3.31). Since we mentioned that the strength amplitude coefficient X of intrinsic alignment is negative, hence so is the power spectrum P^{GI}. Physically, this is due to the fact that the gravitational shear in the background galaxies are tangential *w.r.t.* to the mass concentration center, while the intrinsic shear is radial. Therefore these two types of shears are anti-correlated and their power spectra is negative. Note the intrinsic alignment coefficient X can be controlled with keyword IA_FACT and a cutoff at small scale in the IA power spectrum can be set with keyword IA_KCUT; both are similar to those in SHUFF.

The power spectrum P_σ of the intrinsic ellipticity dispersion can be formulated as $P_\sigma = \sigma_\varepsilon^2/n$ where σ_ε is the dispersion of the intrinsic ellipticity distribution, controllable with keyword GAL_ESIG, and n is the number density of galaxies in the filtering area containing the shear signal. The power spectrum is defined such that when the dispersion increases, or when the number density of sheared galaxies is low, the noise increases. As we mentioned before, practically, the number of galaxies is estimated from the number of non-zero grid points in the ellipticity map after all the galaxy ellipticities are binned. Since total number of shear signal is limited in the data, when the size of the filter (or scale of interest) exceeds to size of FoV, the density will decrease. Thus at large scale this power spectrum increases with scale, $P_\sigma = P_\sigma(\ell)$, and at small scale, it is a flat spectrum where n is constant. In LENSFILTER, if we denote the

FoV is $L \times L$ in rad^2, the radius of filter $R = 2\pi/\ell$ in rad, and the total number of shear signal N, the scale dependence of the shear signal number density is $n(\ell) = NA(\ell)/(\pi R^2(\ell)L^2)$, where the effective overlap area $A(\ell)$ between the filter and FoV reads,

$$A(\ell) = \begin{cases} \pi R^2 & (R < L/2) \\ \pi R^2 + 2L\sqrt{R^2 - (L/2)^2} - 4R^2 \arccos(L/2R) & (L/2 \le R < L\sqrt{2}/2) \\ L^2 & (R \ge L\sqrt{2}/2) \end{cases} \quad . \quad (4.28)$$

Note that $n(\ell)$ is in unit of rad^{-2}, so that P_σ has the dimension rad^2, as expected.

In Fig.4.1 we show two examples of the total noise contributed by different power spectra in the Fourier space. The main difference between these two cases is the redshift distribution of
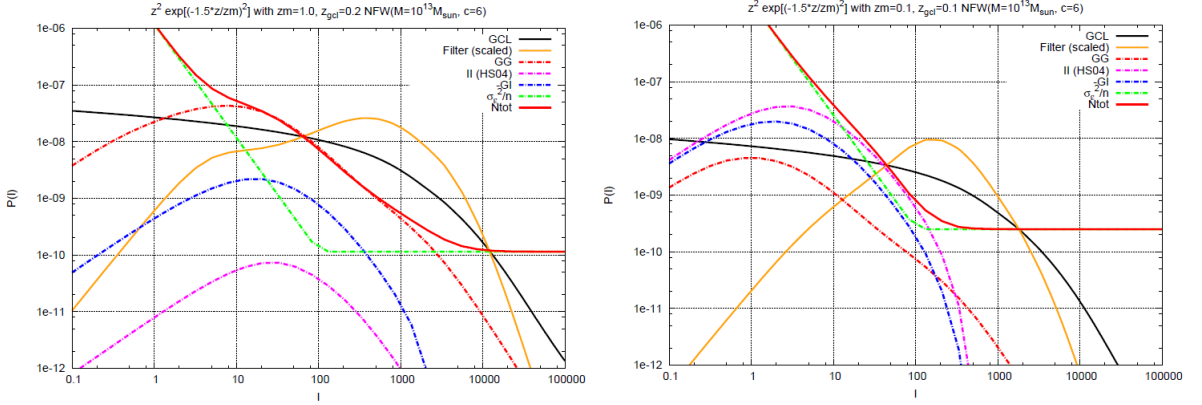

Figure 4.1: The comparison of the shear signal in Fourier space, noise power spectra and filter between two different source redshift distribution depths. The median redshift $z_m = 1.0$ on the left panel whhile $z_m = 0.1$ on the right. See text for details.

the source galaxies. We adopted the same redshift distribution model $n_{\rm LUD}(z)$ (see Eq.3.1) but with two different depths. In Fig.4.1a, the median redshift of the source galaxies is $z_m = 1.0$, while in Fig.4.1b, $z_m = 0.1$. The black line is the Fourier transform of the reduced shear profile of a NFW cluster halo with virial mass $M_{\rm vir} = 10^{13}M_\odot$ and concentration $c = 6$, located at different redshift $z_{\rm cl} = 0.2$ in Fig.4.1a, and $z_{\rm cl} = 0.1$ in Fig.4.1b. It can be seen that for clusters with the same properties (mass and concentration), the strength of its shear signal also depends on the relative redshift of the clusters and the redshift distribution of the source galaxies, by a factor $\langle D_{\rm ds}/D_{\rm s}\rangle$. Deeper source redshift distribution boosts the sampled shear signal from the cluster. The noise power spectra are dashed lines, with the intrinsic ellipticity dispersion P_σ in green, cosmic shear P^{GG} in red, intrinsic shear P^{II} in magenta and the correction between the latter two P^{GI} in blue. All the power spectra are integrated over the complete redshift distribution of the source galaxies. We notice that on small scales (large ℓ), the shear noise is dominated by the intrinsic ellipticity and the number density of the background galaxies. To the larger scales (smaller ℓ), the cosmic shear or intrinsic shear starts to dominate, and on even larger scales, the noise due to limited number of shear signal in the image, hence lower density of galaxies dominates again. Interestingly, the ratio between the noise from cosmic shear and intrinsic shear changes according to the redshift distribution of sources, with the deeper distribution, the higher contribution from the cosmic shear than from intrinsic shear. This is expected, from the fact that cosmic shear arise from the background galaxies while the intrinsic shear plays more important role in the local foreground galaxies (Hirata & Seljak 2004). Note that the anticorrelation between the cosmic and intrinsic shear gives a negative power spectra, in the sense that it somehow compensates the tangential shear noises from the

cosmic shear. The sum of all the noise power spectra is the solid red lines. As both the noise and signal changes with the redshift distribution, so does the filter, which is the solid golden lines. The filters peak at scales where the signal dominates over the noise in Fourier space. As there is no universal filter applicable to all the noise conditions and clusters to be detected, with LENSFILTER, it is possible to integrate all the aspects and build a filter specifically for each case.

In order to see how different noise components affect the filtering detection, LENSFIL-TER offers the option to switch on and off the each noise components with keyword `P2D_NN`. By default, all the noise components are switched on, with `P2D_NN`= 3, thus the total noise power spectrum $P(\ell) = P_\sigma(\ell) + P^{GG}(\ell) + P^{GI}(\ell) + P^{II}(\ell)$. Optionally, with `P2D_NN`= 2, the program ignores the intrinsic alignment noise power spectrum and accordingly also the power spectrum of correlation between intrinsic and cosmic shear. At last, with `P2D_NN`= 1, only the noise due to intrinsic ellipticity dispersion is taken into account. It is also worth mentioning that, when noise power spectrum is used to built the filter, it is scaled by a half, since we are filtering the tangential shear signal of the cluster, where only one (tangential) component of the ellipticity is taken into account.

4.4.3   Lens configuration

The shear signal from galaxy cluster depends on the density profile, total mass and redshift of the cluster, and the shear strength is scaled according to the distance factor $D_{\mathrm{ds}}/D_{\mathrm{s}}$ averaged over the redshift distribution of the source galaxies. Given the source redshift histogram built up above, the user can specify the properties of the cluster to be detected with the filtering techniques, *i.e.* the density profile model of the cluster halo, with keyword `GCL_MODEL` set as `NFW` or `SIS`, the redshift of the cluster, passed to keyword `GCL_Z`, the parameters of the halo density profile model, passed to keyword array `GCL_PARAM`. For NFW halo, the user needs to provide the virial mass, concentration parameter, the virial density contrast and the density profile slope index. If the concentration parameter is set with negative value, LENSFILTER switches on the mass-concentration relation for the NFW model,

$$c\left(M_{\mathrm{vir}}, z\right) = \frac{K}{1+z} \left(\frac{M_{\mathrm{vir}}}{1.5 \times 10^{13} h^{-1} M_\odot} \right) , \tag{4.29}$$

where we adopted the fitting result $K = 9, \alpha = -0.13$ (Bullock etal, 2001).

As the cluster halo model is parameterized, similar to the procedure in SHUFF, a convergence map of the cluster is calculated with dimension twice as the dimension of the input ellipticity map. During the projection, the cluster is set at the center of the filter map. During the projection, the cluster is set at the center of the filter map. We remind that the cluster position here has nothing to do with the cluster positions in the data to be filtered. Here we project the cluster halo in order to model the signal of its reduced shear for the construction of a numerical two dimensional filter, whose center coincides with the origin of signal. With such a filter, we can convolve the map of galaxy ellipticities already calculated. The other advantage of locating the cluster at the center is that, for even number of grid points as the dimension size, the center of the cluster is between the sampling grid points, so that the divergent convergence center of the cluster is never sampled. Compared to SHUFF, the difference here in LENSFILTER is that, the cluster we wanted to detect is set to be spherical, so that all the orientational Euler angles are zero, and two halo tri-axial ratios are both unitary. In principle, we can adapt these internal settings for the detections of elongated halo with certain orientation, however, for the detection of general cluster halos in the current thesis work, we switch off the triaxiality.

Following the same steps in SHUFF, we can convert the convergence map κ_{mn} to shear map $\boldsymbol{\gamma}_{mn}$ with finite difference kernel and discrete Fourier transform method, and obtain the reduced shear map $\mathbf{g}_{mn}$ with the cluster located in the center (see Ch.?? for details). During the calculation of convergence and shear, the scaling of lensing strength with the redshift distribution of the source galaxies is applied. Since galaxy cluster produced only tangential shear, we further derived a reduced tangential shear map $g_{mn} = \sqrt{g_{1,mn} + g_{2,mn}}$, which is the signal part for the filter construction.

4.4.4 Filter construction

With the reduced tangential shear map $g(\boldsymbol{\theta})$ of the cluster that we want to detect, and the noise power spectra $P(\ell)$ as a function of wavenumber $\ell = 2\pi/\theta$, we can construct the filter according to the filtering techniques.

Suppose the reduced tangential shear map has a field of view $L \times L$ in rad^2, and is sampled with $N \times N$ map grids. We first find its normalization factor $A = \sum g_{mn}$, and decompose it into a normalized spatial part τ_{mn} scaled by the amplitude A, $i.e.$ $g_{mn} = A\,\tau_{mn}$. Then the Fourier transform of the normalized reduced tangential shear map $\hat{\tau}_{jk}$ is,

$$\hat{\tau}_{jk} = \frac{L^2}{N^2} \sum_{m=0}^{N-1} \sum_{n=0}^{N-1} \tau_{mn}\, \mathrm{e}^{-i\frac{2\pi}{N}(mj+nk)} \ . \tag{4.30}$$

For each Fourier component $\hat{\tau}_{jk}$ with wavenumber $\ell = (2\pi/L)\sqrt{j^2 + k^2}$, we interpolate the precalculated noise power spectrum to derive $P_N(\ell)$. Dividing $\hat{\tau}_{jk}$ by the total noise power spectrum at ℓ, and applying the backward Fourier transform, we get the unnormalized filter,

$$\Psi_{mn} = \frac{1}{L^2} \sum_{j=0}^{N-1} \sum_{k=0}^{N-1} \frac{\hat{\tau}_{jk}}{P_N(\ell)}\, \mathrm{e}^{+i\frac{2\pi}{N}(mj+nk)} \ , \tag{4.31}$$

which is a discrete form Eq.(1.14). For the normalization factor of the filter, we further calculate the component $|\hat{\tau}_{jk}|^2/P(\ell)$ in Fourier domain, and transform it back to spatial domain,

$$\Phi_{mn} = \frac{1}{L^2} \sum_{j=0}^{N-1} \sum_{k=0}^{N-1} \frac{|\hat{\tau}_{jk}|^2}{P_N(\ell)}\, \mathrm{e}^{+i\frac{2\pi}{N}(mj+nk)} \ . \tag{4.32}$$

Compared with Eq.(4.13), it is obvious that the normalization factor is just the inverse of Φ_{00}. Thus we construct a filter according to the cluster shear signal and shear noise properties,

$$\Psi_{mn} = \frac{1}{\Phi_{00}\,L^2} \sum_{j=0}^{N-1} \sum_{k=0}^{N-1} \frac{\hat{\tau}_{jk}}{P_N(\ell)}\, \mathrm{e}^{+i\frac{2\pi}{N}(mj+nk)} \ , \tag{4.33}$$

and at the same time, we also get the expected detection S/N ratio with this filter,

$$\mathrm{S/N} = \frac{A}{\sqrt{\Phi_{00}}} \ . \tag{4.34}$$

The detection S/N ratio thus calculated gives a theoretical reference value for the detection peaks in the detection map, according to the theoretical modeling of the shear signal and noise properties. Generally speaking, peaks in the detection map with S/N> 3 can be regarded a true detection of a cluster producing the expected shear pattern, which imposes a theoretical limit for the detection of galaxy cluster. For a detection with lower S/N ratio, it may not be distinguishable between the true cluster and a spurious one which results from the noise. We will come back to this point again when we apply the filter to the simulated and real data.

4.4.5 Convolution for S-map

Once we get the filter map, with the convolution method, we can apply it to the ellipticity map we prepared before from the input ellipticity catalog of the galaxies.

We recall the expression for the signal and noise in S-statistics, *i.e.* Eq.(4.1) and Eq.(4.2),

$$S(\boldsymbol{\theta}) \quad = \quad \frac{1}{n} \sum_i \varepsilon_{\mathrm{t}i}(\boldsymbol{\theta}_i)\Psi(|\boldsymbol{\theta}_i - \boldsymbol{\theta}|) \, , \tag{4.35}$$

$$\sigma^2(\boldsymbol{\theta}) \quad = \quad \frac{1}{2n^2} \sum_i |\varepsilon_i(\boldsymbol{\theta}_i)|^2 \Psi^2(|\boldsymbol{\theta}_i - \boldsymbol{\theta}|) \, , \tag{4.36}$$

where n is number density of the galaxies, and ε_{t} is the tangential component of the ellipticity and we used $\langle \varepsilon_{\mathrm{t}} \rangle^2 = |\varepsilon|^2/2$. The tangential component is related to two components of ellipticity by,

$$\varepsilon_{\mathrm{t}}(\boldsymbol{\theta}_i) = -\varepsilon_1(\boldsymbol{\theta}_i)\cos 2\phi(\boldsymbol{\theta}_i - \boldsymbol{\theta}) - \varepsilon_2(\boldsymbol{\theta}_i)\sin 2\phi(\boldsymbol{\theta}_i - \boldsymbol{\theta}) \, , \tag{4.37}$$

where $\phi(\boldsymbol{\theta}_i - \boldsymbol{\theta})$ is the position angle of a galaxy at $\boldsymbol{\theta}_i$ with respect to the position of interest $\boldsymbol{\theta}$. Now the analytical expression above can be readily written in terms of convolution,

$$S(\boldsymbol{\theta}) \quad = \quad -\frac{1}{n}\big[(\varepsilon_1 * \Psi_{\mathrm{c}})(\boldsymbol{\theta}) + (\varepsilon_2 * \Psi_{\mathrm{s}})(\boldsymbol{\theta})\big] \, , \tag{4.38}$$

$$\sigma^2(\boldsymbol{\theta}) \quad = \quad \frac{1}{2n^2}\big[(|\varepsilon|^2 * \Psi^2)(\boldsymbol{\theta})\big] \, , \tag{4.39}$$

where $\Psi_{\mathrm{s}} = \Psi \sin 2\phi$, $\Psi_{\mathrm{c}} = \Psi \cos 2\phi$ can be easily obtained by weighting the filter map Ψ with the position angle map $\cos 2\phi$, $\sin 2\phi$ with origin at the center of the filter. For details about the numerical implementation of convolution, see Appendix A.2.

Note that the ellipticities used here are binned galaxy ellipticities which are weighted by w_i and normalized $\sum w_i = 1$ (see above source control part). In practice, as we build the filter with dimension $2L \times 2L$, the ellipticity maps are zeropadded to the same dimension, applied the convolution and boundary-trimmed, in order to avoid the vignetting effects.

4.5 Examples of filtering detection with LENSFILTER

Up to now, we described the detail implementation of filtering techniques. In short, given the input catalog of galaxies ellipticities, and with the desired cluster halo for detection configured, LENSFILTER builds up a optimal filter according to the spectra analysis of the signal and noise, applied the convolution to the ellipticity field and outputs a cluster detection S/N map. The user are referred to Appendix A for detail usage and help for running the program. In next section, we will apply the method to the SHUFF simulation data and real data from CHFTLS survey. Before that, we show two examples of filtering result.

To compared the filtering method in LENSFILTER with some general filters, *e.g.* Gaussian filters, we simulate with SHUFF three trixial cluster NFW halos at redshift $z_d = 0.2$ with virial mass $M_{200} = (10^{15}, 10^{14}, 10^{13})\, M_\odot$, concentration $c = 6$, and source galaxies at redshift $z_s = 1.0$ with intrinsic ellipticity dispersion $\sigma_\varepsilon = 0.3$. With the lensed ellipticity catalog from SHUFF, we used LENSFILTER configured for detection of specified halo masses with the same source properties, and compared the filtering result with a Gaussian filter with sizes $r = (1, 2, 4)$ arcmin, as shown in Fig.4.2. It can be seen that for Gaussian filter, if the filter size is chosen too small, cluster halos become undistinguishable from the spurious structure in the S/N map due to the noise in the intrinsic ellipticity, c.f. right-most plot on the lower row in Fig.4.2. Thus one has to have a right "guess" at the filter size in order to recover the halos input in the simulation. Moreover, even though the filter size is large enough, spurious
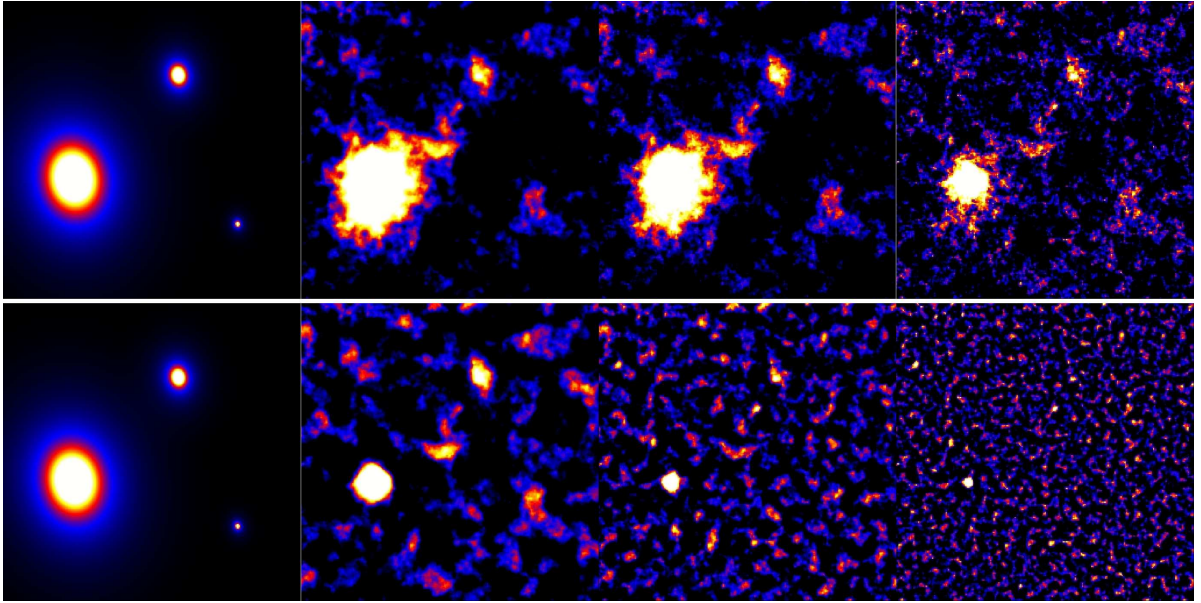
Figure 4.2: The comparison of filtering result for the same 3 triaxial NFW halos at $z_d = 0.2$ within 1 deg^2 FoV (*left-most plots*), with LENSFILTER (*upper plots*) and Gaussian filters with different size (*lower plots*). Source galaxies are locate at single source plane $z_s = 1.0$ with intrinsic ellipticity dispersion $\sigma_\varepsilon = 0.3$. LENSFILTER is configured with the same halo mass $M_{200} = (10^{15}, 10^{14}, 10^{13}) \, M_\odot$ as in SHUFF, leading to three S/N maps from left to right in the upper row. The result from Gaussian filters with filter size $r = (4, 2, 1)$ arcmin are shown from left to right in the lower row.

structures may still present in the detection map, c.f. second plot on the lower row in Fig.4.2, since the filter is not specifically designed for the target shear profile. In case of optimal filter from LENSFILTER, the spurious structures are suppressed as the filter is built to minimize the variance in S-statistics. For the less massive halos, the filter still produces a significant S/N ratio compared to Gaussian filter, so as to optimize the detection of desired halos. The LENSFILTER detection S/N ratio for halo with $M_{200} = (10^{13} \, M_\odot$ is low, which is related to the weak shear singal compared with the intrinsic ellipticity noise level. For these low mass halos, one may need additional informations to disentangle true detections from spurious ones, as we will show in the next example, with a tomography approach.

To study the lower limit of cluster mass that can be detected by optimal filtering method, we further use SHUFF to simulate a NFW halo with mass $M_{200} = (10^{13} \, M_\odot$ at redshift $z_d = 0.2$, and source galaxies distributed in redshift with $z_m = 1.5$, Fig.4.3. In this case, the difference in the source properties is that, for each simulated galaxy, the redshift is known, so that one can make use of subsamples of galaxies at different redshift ranges and compare the sampling of the same cluster shear at different distance. We first run LENSFILTER over the ellipticity field of all the galaxies with $z_s > 0.2$, *i.e.* behind the cluster and obtain a detection map with the cluster we input and a number of other spurious peaks, as shown in lower left plot of Fig.4.3. To determine whether these peaks are due to physical mass concentration or simply due to the noise in intrinsic ellipticity, we further run LENSFILTER over the ellipticities of galaxies within four source redshift ranges, (i) $(0.5, 1.0)$ (upper-center plot), (ii) $(1.0, 1.5)$ (upper-right plot), (iii) $(1.5, 2.0)$ (lower-center plot) and (iv) $z_s > 2.0$ (lower-right plot). From comparison between these four plots, we notice first that the cluster detection is most significant in range (ii) and (iii), where the source redshift distribution peaks. For subsamples in lower redshift
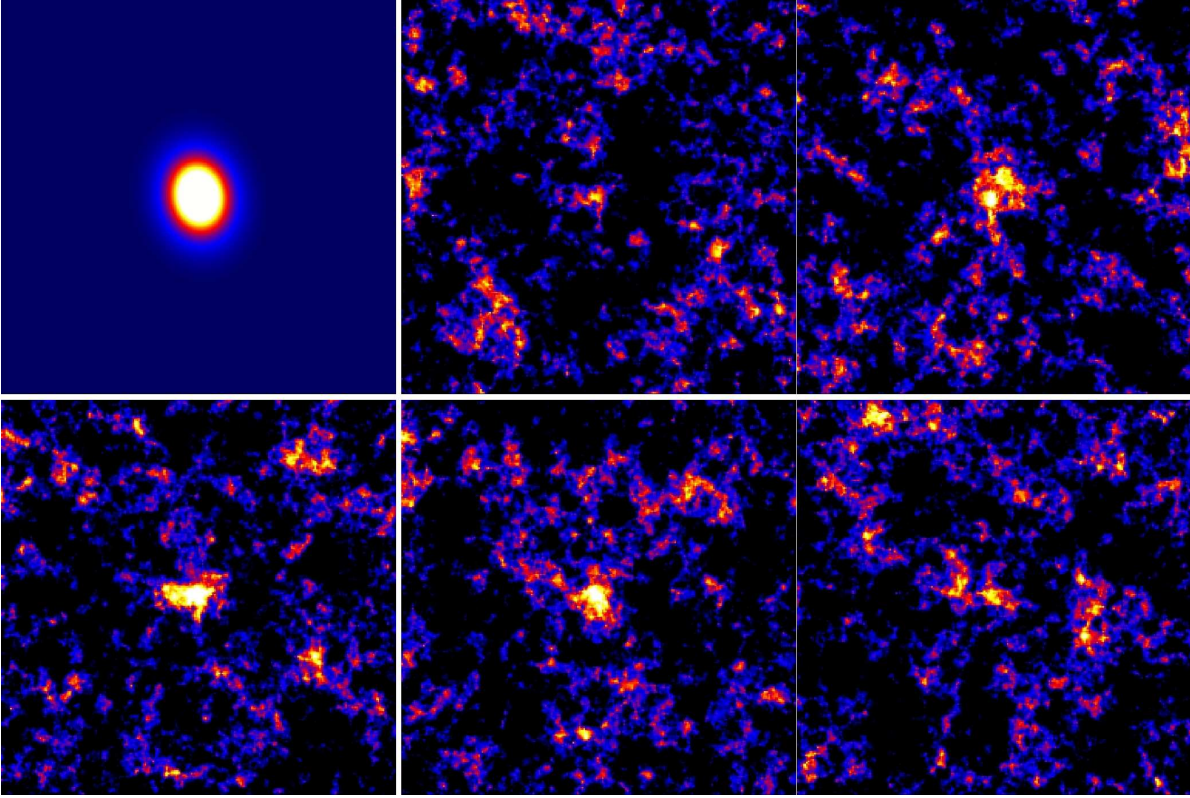
Figure 4.3: Optimal filtering detection with a less massive $M_{200} = 10^{13} \, M_\odot$ NFW halo at redshift $z_d = 0.2$. The source galaxies are distributed in redshift with median redshift $z_m = 1.5$. The cluster convergence map is shown in *upper-left* plot, while the optimal filtering detection, obtained from the ellipticities of all the background galaxies, is shown in *lower-left* plot. Four plots on the right show the detection results with subsamples of galaxies in redshift range (i) $(0.5, 1.0)$ (upper-center plot), (ii) $(1.0, 1.5)$ (upper-right plot), (iii) $(1.5, 2.0)$ (lower-center plot) and (iv) $z_s > 2.0$ (lower-right plot). While spurious detections appear only in some of the plots, the true detection peak in the center is present in maps of different redshift ranges.

range (i), the galaxy number density is high enough but the sampled shear is too low due to the low lensing strength $\langle D_{ds}/D_s \rangle$. For subsamples in the highest redshift range (iv), the galaxy number density is too low and their ellipticities are mainly dominated by the intrinsic ellipticity dispersion rather than the shear. However, we also notice that if the detected peak is physical, it should be present in the detection maps with background galaxies in different ranges, which in our case, is the central peak corresponding to the halo we input in the simulation. For the other detections in the map for all the galaxies $z_s > 0.2$, they are present only in some of the subsample detection maps, through which we can classify them as spurious. In this way, we can lower the cluster mass limit for optimal filtering detection, with the redshift information of the galaxies. Of course, in practise, there will be no spectroscopic redshift for all the galaxies at high redshift, but the tomography filtering detection can still be achieved given that accurate photometric redshifts are available.

4.6 Application of LENSFILTER to SHUFF simulation and real data

As an application of the optimal filtering in LENSFILTER, in this section, we will discuss the filtering detection result from SHUFF simulation and real data with LENSFILTER. We will first introduce the real data that we chose from the CFHT Legacy Survey. According to the property of galaxies in the real data, we setup two sets of SHUFF simulation with source properties similar to that in the real data. Then we applied the filtering detection to the ellipticity catalogs of lensed galaxies from the simulation and discuss the result as a primary investigation of the cluster detection limit. Finally, we apply the method to the real data and compare the result with X-ray observations.

4.6.1 CFHTLS data used in filtering detection

The real data we chose here is from the CFHT Legacy Survey (T05 release)[*] in r band. We select two deep fields (D1 and D2) and two pointings in the W1 (p2p3, p2p2) as shown in Fig.4.4. We summarize the image and source galaxy properties, namely the galaxy number
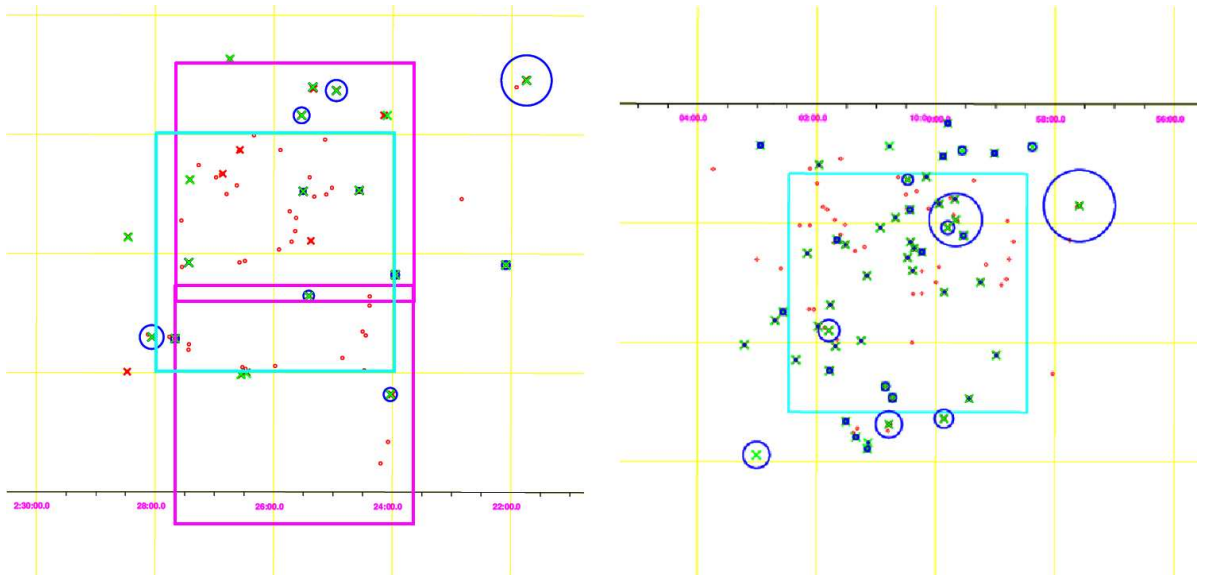

Figure 4.4: Four CFHTLS pointing chosen for cluster detection with LENSFILTER. On the left is the D1 pointing (cyan box) and two pointings from W1p2p3 (upper magenta box), and W1p2p2 (lower magenta box). On the right is the D2 pointing (cyan box). Marks such as points and crosses indicate the available cluster detections from mostly X-ray detections and the radius of blue circles indicates the X-ray mass. See text for detail specifications.

density n_{gal} and median source redshift z_m in the following table.

Pointing	WCS coordinates	Exposure time	n_{gal}/arcmin^2	z_m
D1	$(36.49583333, -4.494444444)$	58hr	42	1.0
D2	$(150.1166667, +2.208333333)$	37hr	35	0.9
W1p2p3	$(36.41425000, -4.200000000)$	42min	10	0.6
W1p2p2	$(36.41425000, -5.133333333)$	24min	4	0.5

---

[*]The image data is publicly available at `http://cadcwww.dao.nrc.ca/cfht/T0005.html`

The galaxies number density is estimated from the catalog extracted with SExtractor and masked by ExAM. The shape measurement is done with the improved KSB pipeline, LensR, developed by M. Radovich. The median redshift is estimated from the public photometric redshift catalog for CFHTLS Deep and Wide fields (Coupon et al. 2009).

We select these four pointings for the following reasons. Two Deep fields D1,D2 are observed with long exposure time and contain high number density and deep redshift distribution, allowing for ideal study of cluster detection with weak lensing. Two pointings in W1 are selected due to their large overlap regions with D1, thus the detection results can be compared between the deep and wide exposures. Despite the lack of very massive clusters in the fields, these regions contain relatively high density of published cluster detections in the literature and registered in the online database NASA/IPAC Extragalactic Database (NED)[†]. They are detected mostly with other methods like the density of luminous galaxies, color selection, X-ray luminosity and spectroscopic analysis (for low redshift clusters). We marked all the registered galaxy clusters in NED with the red spot in Fig.4.4, and clusters with X-ray sources in NED with the red cross. Besides, these pointing have full overlap with specific X-ray cluster surveys. D1 and two Wide pointings overlap with XMM-LSS survey, in which a number of galaxy clusters are confirmed with spectroscopy and/or through color selections[‡] (e.g. Andreon et al. 2004; Valtchanov et al. 2004; Andreon et al. 2006; Pierre et al. 2006; Pacaud et al. 2007). In Fig.4.4, we marked the public redshift confirmed XLSSC clusters in L3sdb database[§] with green cross, and those with X-ray mass estimated by Pacaud et al. (2007) with blue circles, of which the radius indicates the equivalent virial mass M_{200} converted from X-ray luminosity mass M_{500}, *e.g.* the biggest circle in the top-right corner, outside of the pointings, corresponds to a cluster with $M_{200} = 1.9 \times 10^{14} M_\odot$. D2 overlaps with Cosmological Evolution Survey (COSMOS) field, and we mark the X-ray detected redshift confirmed clusters found by Finoguenov et al. (2007) with green cross, and X-ray equivalent cluster mass M_{200} by the radius of blue circles, *e.g.* the biggest circle in the upper-right, outside of D2, corresponds to a cluster with $M_{200} = 2.7 \times 10^{14} M_\odot$ ($z = 0.37$), and the second most massive cluster within D2 field has $M_{200} = 2.0 \times 10^{14} M_\odot$ but located at relatively high redshift for weak lensing study $z = 0.73$.

4.6.2   The Shuff simulation datasets and filtering results

According to the source galaxy properties in the CFHTLS Deep and Wide data that we selected, we configure Shuff to simulate two kinds of weak lensing source galaxy distributions, with name SimD and SimW for datasets with source properties similar to those in the CFHTLS Deep and Wide images, respectively. For both datasets, we set the intrinsic ellipticity dispersion of galaxies $\sigma_\varepsilon = 0.3$, with redshift distribution $n_{\mathrm{LUD}}(z)$ (defined in Eq.3.1), and uniform random positions in 1 deg^2 field-of-view. The differences between two datasets are in the galaxy number density n_{gal} and median redshift z_m, where we set,

$$\begin{aligned} \text{for SimD:} \quad & n = 40 \ \mathrm{arcmin}^{-2}, \quad z_m = 1.0 \\ \text{for SimW:} \quad & n = 10 \ \mathrm{arcmin}^{-2}, \quad z_m = 0.5 \end{aligned}$$

which roughly represents the data quality of CFHTLS images we selected.

For both SimD and SimW source galaxies, we select a series of 16 spherical NFW halos

---

[†]The NED database can be accessed at `http://nedwww.ipac.caltech.edu/`
[‡]`http://www.brera.mi.astro.it/~andreon/clusters_public.html`
[§]`http://l3sdb.in2p3.fr:8080/l3sdb/login.jsp`

with their virial radius M_{200} and redshift z_d in,

$$M_{200} = (0.5, 1.0, 5.0, 10.0) \times 10^{14} M_\odot ,$$
$$z_d = (0.2, 0.4, 0.6, 0.8) .$$

For simplicity, here we adopt the mass-concentration $c(M, z)$ relation defined in Eq.(1.56) (Bullock et al. 2001; Comerford & Natarajan 2007). For each one of 16 types of NFW halos, we randomly distributed 10 halos in 1 deg^2. In other words, we configured totally 32 runs of SHUFF simulation for 2 type of sources, each with 16 types of lenses. Within each run, the distribution of source position, redshift, ellipticities, and lens positions are randomized.

As a primary application, we did not include the cosmic shear and intrinsic shear as noises in the SHUFF simulation. Thus, the following conclusion about the limit of cluster detection shall be taken with caution; what we estimate is the optimistic upper limit of the cluster detection.

The output lensed galaxy catalogs from these SHUFF simulation are directly input into LENSFILTER, and we used both the "accurate" ellipticity and redshift of the source galaxies from the catalog, *i.e.* without any measurement errors. Compared with the measured catalog from the real data, the "error-free" input for LENSFILTER will certainly benefit the detection result.

We also remind that in nature, the number density of the cluster halos depends on the halo mass and evolves with redshift, which can be derived either analytically from the halo mass function $N(m, z)$, *e.g.* in Press-Schechter formalism (Press & Schechter 1974), or from the N-body numerical simulation (e.g. Springel et al. 2005).

We plan to take into account these effects in a further analysis of cluster detection limit investigation with SHUFF/LENSFILTER, that will be done as a follow-up of this work. For the moment, we stay with the above basic configurations for the simulation datasets, and estimate firstly the limit related to the mass, redshift of the cluster halo, and the density, median redshift of the source galaxies. The result of such an estimation can be taken as a starting point not only for the more complicated study, but also for the filter configuration in its real data application.

In the following, we will discuss some representative cases among the 32 optimal filtering results.

We start with detection for SimD dataset first. Fig.4.5 shows the detection of the cluster halos of the same mass $M_{200} = 5 \times 10^{14} M_\odot$, at different redshifts $z_d = 0.2$ (upper-left plot), $z_d = 0.4$ (upper-right plot), $z_d = 0.6$ (lower-left plot), $z_d = 0.8$ (lower-right plot). The color indicates the S/N ratio in S-statistics, and the contour outlines the region with S/N level $(3, 4, 5, 6)$. The black crosses are the positions of halos randomly distributed in SHUFF. Due to the high galaxy number density and deep redshift distribution in SimD, the clusters are detected with S/N> 3 upto $z_d = 0.6$, nearly half of the source median redshift. For clusters at higher redshift, as the source number density decrease, and in the real case, the shape measurement for those lensed galaxies are also noisy, the noise level become relative stronger compared to the shear signal as limited by the mass of the cluster. Some clusters are then missing in the detection map, *i.e.* the detection completeness starts to drop, and spurious detections with S/N> 3 start to appear.

Fig.4.6 shows the dependence of the cluster detection completeness on the mass of the cluster. All the clusters in the plots are at the same redshift $z_d = 0.4$, which is not high compared to the source median redshift $z_m = 1.0$ in SimD. The mass of the clusters is $M_{200} = 10^{15} M_\odot$ (upper-left plot), $M_{200} = 5 \times 10^{14} M_\odot$ (upper-right plot), $M_{200} = 10^{14} M_\odot$ (lower-left plot), $M_{200} = 5 \times 10^{13} M_\odot$ (lower-right plot). Again the meaning of color, contour and crosses is the same as above. From the comparison between the four plots, we see that for clusters

with mass above $5 \times 10^{14} M_\odot$, the detection is complete, while the completeness drop quickly as the mass becomes lower (50% for $10^{14} M_\odot$). When the mass drops below $5 \times 10^{13} M_\odot$, all clusters in the simulation are missed, and some spurious detection with S/N> 3 appear. This shows that given the source properties and cluster redshift, low cluster mass is an intrinsic limit for the its detection.

We then take a look the situation with SimW, where the source galaxies density is low, and their redshift distribution is shallow. Fig.4.7 is similar to Fig.4.5 except that the mass of all the clusters is $M_{200} = 10^{15} M_\odot$. While this mass level is high enough for nearly all the clusters to be detected in deeper simulation SimD, the detection completeness starts to drop when the cluster redshift is $z_d \geq 0.4$. For higher redshift clusters, despite they are massive enough, the number of spurious detections is comparable with the true one, as expected from the low source density and high intrinsic ellipticity noise. When $z_d \geq 0.8$, the completeness is zero, and even the spurious detections are suppressed, due to the extremely low density source galaxies behind the clusters. Empirically, we find again that the completeness of detection drops quickly when the cluster redshift is beyond the half of the median source redshift.

Finally, we look at Fig.4.8, which is analogy to 4.6 except that the cluster redshift is $z_d = 0.2$ which is less than the half of median source redshift $z_m = 0.5$ in SimW. Similarly, clusters detection is complete for $10^{15} M_\odot$ and as the mass decreases, the completeness drops and number of spurious detections increase, for the same reason as in SimD.

We summarize the results in the following tables, where we list for each case, the number of peaks with S/N> 3, $N_{S/N>3}$ and number of peaks with S/N> 3 which corresponds to cluster detections, $N_{cl} \in [0, 10]$.

SimD ($n = 40$ arcmin^{-2}, $z_m = 1.0$)

N_{cl} / $N_{S/N>3}$	$z_d = 0.2$	$z_d = 0.4$	$z_d = 0.6$	$z_d = 0.8$
$M/10^{14} M_\odot = 0.5$	8/9	0/3	0/11	2/15
$M/10^{14} M_\odot = 1.0$	10/13	6/9	6/10	1/9
$M/10^{14} M_\odot = 5.0$	10/10	10/11	10/10	8/9
$M/10^{14} M_\odot = 10.0$	10/10	10/10	10/10	10/10

SimW ($n = 10$ arcmin^{-2}, $z_m = 0.5$)

N_{cl} / $N_{S/N>3}$	$z_d = 0.2$	$z_d = 0.4$	$z_d = 0.6$	$z_d = 0.8$
$M/10^{14} M_\odot = 0.5$	0/1	0/3	0/5	0/3
$M/10^{14} M_\odot = 1.0$	1/2	0/2	0/1	0/3
$M/10^{14} M_\odot = 5.0$	7/8	3/5	0/0	0/0
$M/10^{14} M_\odot = 10.0$	10/10	7/8	2/2	0/0

The complete detection corresponds to $N_{cl}/N_{S/N>3} = 10/10$. $N_{cl} < 10$ indicates some simulated clusters are missing or below S/N= 3, while $N_{cl} < N_{S/N>3}$ means additional spurious detections. From the table we find that, with the properties of clusters and source galaxies we simulate here, the mass and redshift are the intrinsic limits for the detection of clusters, while the source number density and redshift distribution are additional noises contribute limit. For high completeness of the cluster detection, we need high number density and deep redshift distribution. Given these condition of the noise level, there will be still a limit related to the cluster mass and redshift.

As we have discussed above, from the current SHUFF-LENSFILTER run, we did not draw the exact value of the limit in mass and redshift, as it depends on the source properties and also additional noise properties such as cosmic and intrinsic shear noises, errors in the shape measurement and photometric redshift, which will be included in the next testing SHUFF-

LENSFILTER run. Also, the numbers in the table above shall be replaced by the statistical percentages by simulating each of the 32 cases at least 10 times more, and meanwhile refining the increment of cluster mass and redshift between the cases, which will boost the number of study cases beyond 32. Such a large number of SHUFF-LENSFILTER runs are straightforward in our current framework and, at the time while the thesis is being written, have been partly desigend and tested, allowing for a more sophisticated limit estimation coming soon. However, current primary result did also show the trend of detection limit dependence and can serve as a optimisic "noise-free" limit, that the analysis from the real data can archieve at best.

4.6.3 Filtering detection results with CFHTLS data

With the analysis based on the SHUFF simulation, we proceed to apply the filter to the real data in CFHTLS data, *i.e.* 4 pointings we have chosen. The mask of the saturation halos and deflection spikes of the bright stars are done with ExAM. The galaxy ellipticity catalog is obtained from the improved KSB pipeline, LensR, developed by M. Radovich, (Huang et al. 2010). Instead of assuming a redshift distribution model, we used in LENSFILTER the public photometric redshift catalog for CFHTLS Deep and Wide fields (Coupon et al. 2009).

Regarding the detection limit as we learned from simulation datasets, for two deep pointings, D1 and D2, we configured the filter in searching for clusters with $M = 5 \times 10^{14} M_\odot$ at redshift $z_d = 0.2$ and 0.4. For two wide pointings, the filter is configured for clusters with $M = 10^{15} M_\odot$ at redshift $z_d = 0.2$. Even though there are not well-known clusters at such mass scale within these pointings, we chose a relatively large target mass since their detection results in the simulations are stable and nearly complete. Applying a filter aiming at larger cluster mass to a true less massive cluster actually yields similar results to cases where the filter is configured with right mass, with the difference that the convolved detection map is blurred due to the larger filtering strength, c.f. the detection of less massive cluster with optimal filter for massive cluster, in second plot from the left in Fig.4.2.

We shown the filtering detection result for D1, with filter configured for NFW cluster with $M = 5 \times 10^{14} M_\odot$ at redshift $z_d = 0.2$ (*left plot*) and 0.4 (*right plot*), in Fig.4.9. In the plots, the XLSSC clusters from XMM-LSS survey (Pacaud et al. 2007) are marked with the same style as in Fig.4.4. The white regions are the masks of bright stars produced by ExAM.

With the filter configured for cluster at $z_d = 0.2$, the galaxies with photometric redshift $z_s > 0.2$ are used as sources. We found 3 significant detections with S/N> 3 which match the XLSSC clusters, with redshift $z_d = 0.14, 0.26, 0.27$. As we further select galaxies at $z_s > 0.4$, we found two consistent detections on upper-right part of FoV, while the detection in the lower-right part becomes less significant. Even though this detection is confirmed with X-ray observation, in our weak lensing analysis, we scale the ellipticity of galaxies with their photometric redshifts which introduce error in the source selection, and may partly account for the decreasing of its significance. It may also due to the missing of shear sigal in the masked region closely located in the lower-right direction. We notice the boost of S/N for a $z = 0.31$ cluster on the left, which may due to a cleaning of foreground $z < 0.3$ galaxies within our photometric redshift selection procedure. As an approximated mass reference indicated by its low X-ray luminosity mass, a cluster with similar mass scale $\leq 10^{13} M_\odot$ is unlikely to produce a significant shear signal given the properties of the source galaixes. Above all, we found that two most significant detections in the image are present in detection with different ranges of source galaxies, and consistent with X-ray clusters.

The similar filtering was done also for D2, as shown in Fig.4.10. From the X-ray mass estimated by Finoguenov et al. (2007), we notice that except for the most massive 3 clusters at high redshift $z_d = 0.73, 0.55, 0.80$, most X-ray clusters in the low redshift are in a mass level $\sim 10^{13} M_\odot$. Also due to much larger masked area and 1 bad CCD chip, and recalling the lower

number density and less exposure time compared with D1, the detections with both filters did not match with X-ray clusters in a one-to-one manner. Nevertheless, a good correlation is still found between clusters detected by our weak lensing approach and those detected by X-ray observation.

Finally, we discuss the filtering detections in two wide pointings, as shown in Fig.4.11. The filtering detection result for two pointings in W1p2p3 (*upper-left plot*) and W1p2p2 (*lower-left plot*), with filter configured for NFW cluster with $M = 10^{15} M_\odot$ at redshift $z_d = 0.2$. Available X-ray detected clusters are marked as in Fig.4.4. From W1p2p2, we see that there is almost no significant detection at all, which is expected from the extreme low number density of galaxies and shallow redshift distribution. We thus conclude that such shallow observation is not suitable for cluster weak lensing studies. However, as a comparison, with the similar redshift distribution, but doubled number density of galaxies, in W1p2p3, we found one significant detection near the center with redshift $z_s = 0.14$. As these two fields overlap with D1, which is the reason we select only these two pointing from W1, we also show the detection map for D1 (Fig.4.9) with WCS coordinates aligned, for comparison. Interestingly, two most significant detections in D1 are found to be present also in W1p2p3, especially for the $z = 0.14$ detection. Besides their matching with X-ray detections, we consider it as a further confirmation of the cluster detected with weak lensing.

4.7   Summary

In this chapter, we have discussed in detail the weak lensing cluster detection with optimal filtering techniques. We described their implementation in the program LENSFILTER. As an example, we have shown the comparison between the result from optimal filter and a general Gaussian filter. We also showed the detection of very low mass cluster with tomography approach. As the application, we first configured the SHUFF simulation with a similar source properties to the real data from CFHTLS. The optimal filtering is then applied to the ellipticity catalog from the simulation and we investigated the limit of cluster detection due to the properties of the source galaxies and clusters. Finally, we applied the filter detection to four pointings in CFHTLS data, and found good agreement with X-ray detections in the D1 image. As a further confirmation of the detection in D1, we also find similar results in the W1p2p3 image, overlapping with D1.

Figure 4.5: The filtering detection with SHUFF simulation SimD datasets. The mass of all the halos in the plots is $M_{200} = 5 \times 10^{14} M_\odot$, with the difference in their redshifts $z_d = 0.2$ (upper-left plot), $z_d = 0.4$ (upper-right plot), $z_d = 0.6$ (lower-left plot), $z_d = 0.8$ (lower-right plot).The color indicates the S/N ratio in S-statistics, and the contour outlines the region with S/N level $(3, 4, 5, 6)$. The black crosses are the positions of halos randomly distributed in SHUFF.
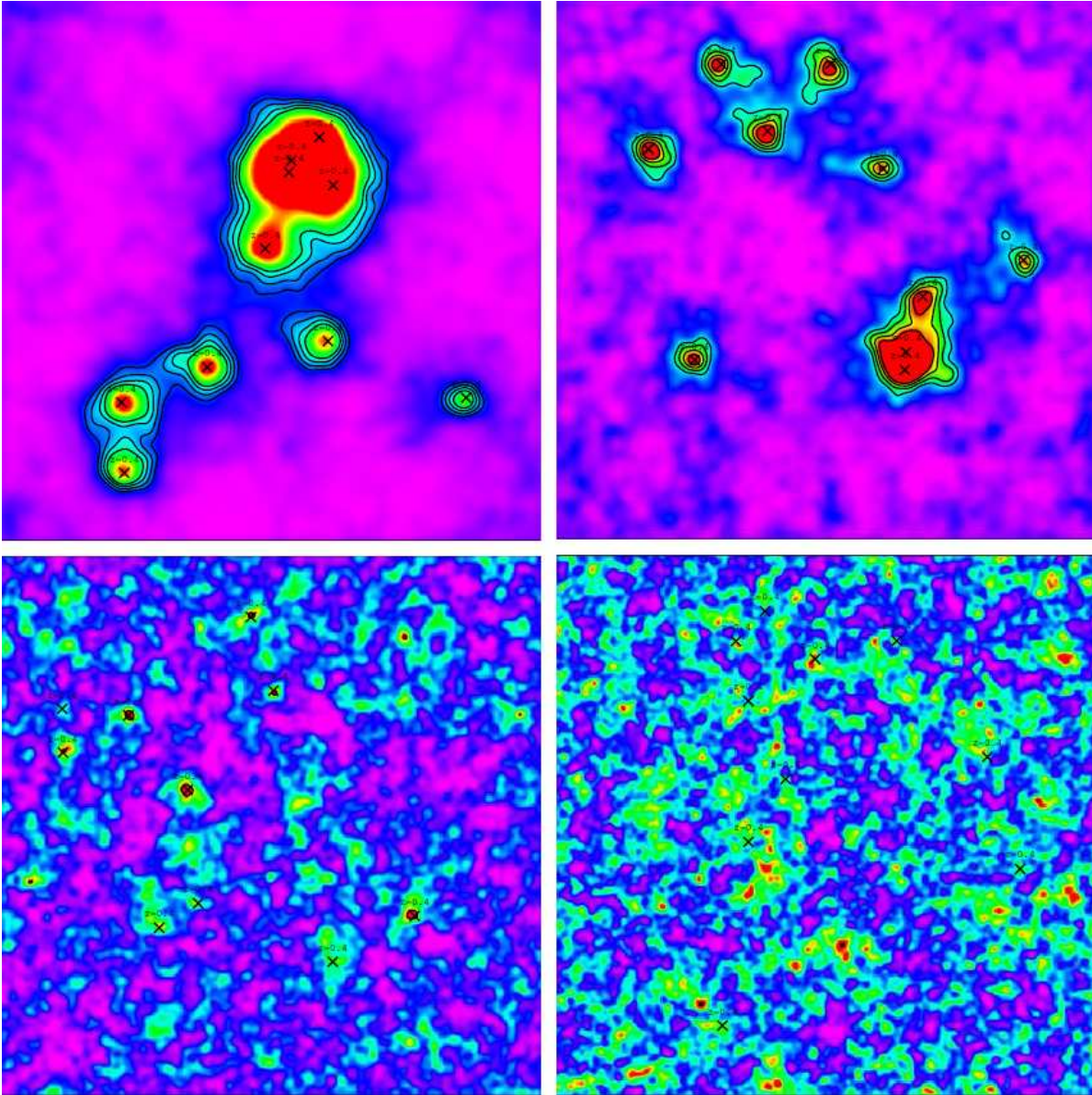
Figure 4.6: The filtering detection with SHUFF simulation SimD datasets. All the clusters in the plots are at the same redshift $z_d = 0.4$, with different mass $M_{200} = 10^{15} M_\odot$ (upper-left plot), $M_{200} = 5 \times 10^{14} M_\odot$ (upper-right plot), $M_{200} = 10^{14} M_\odot$ (lower-left plot), $M_{200} = 5 \times 10^{13} M_\odot$ (lower-right plot). The meaning of color, contour and crosses is the same as in Fig.4.5.
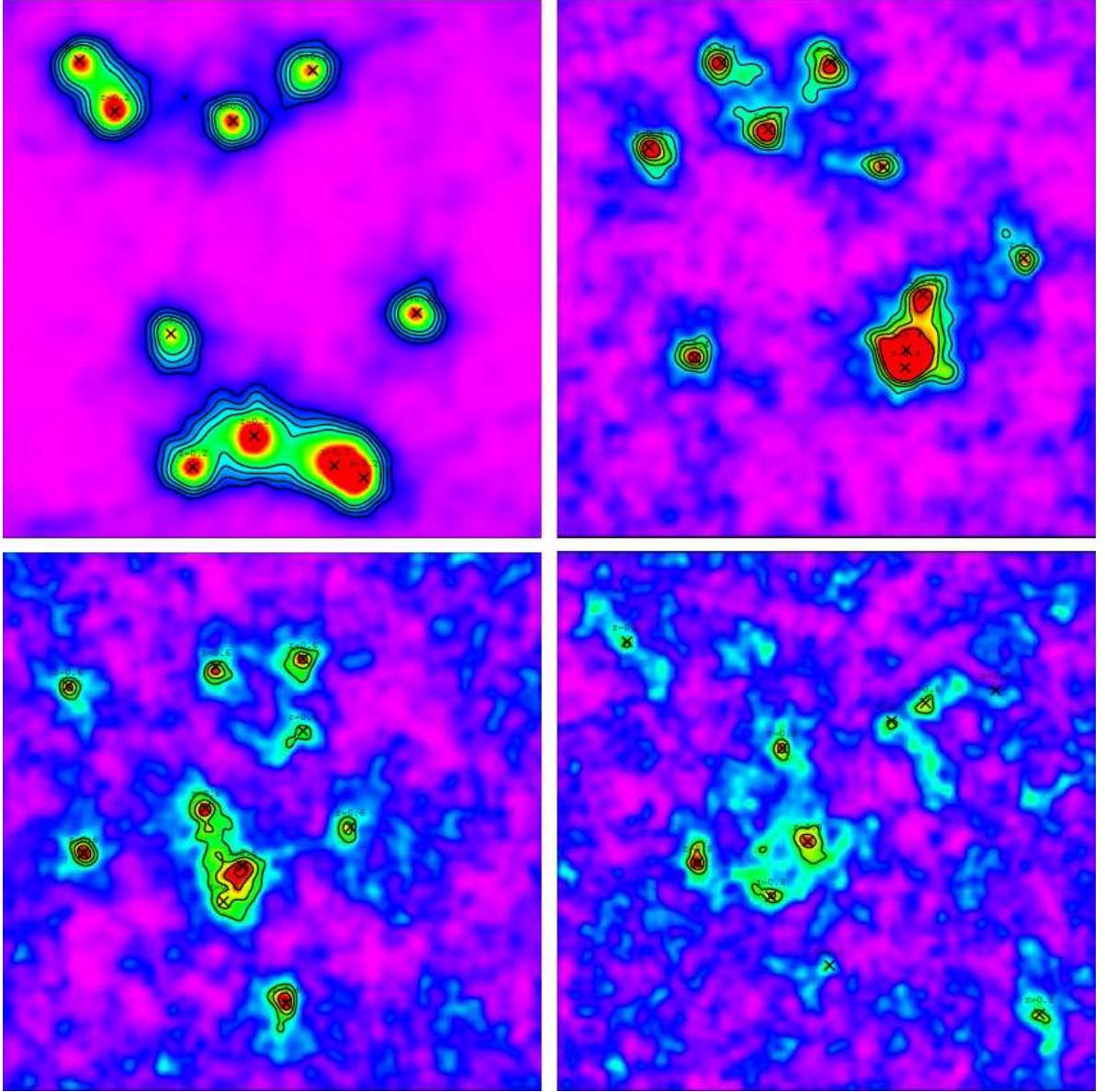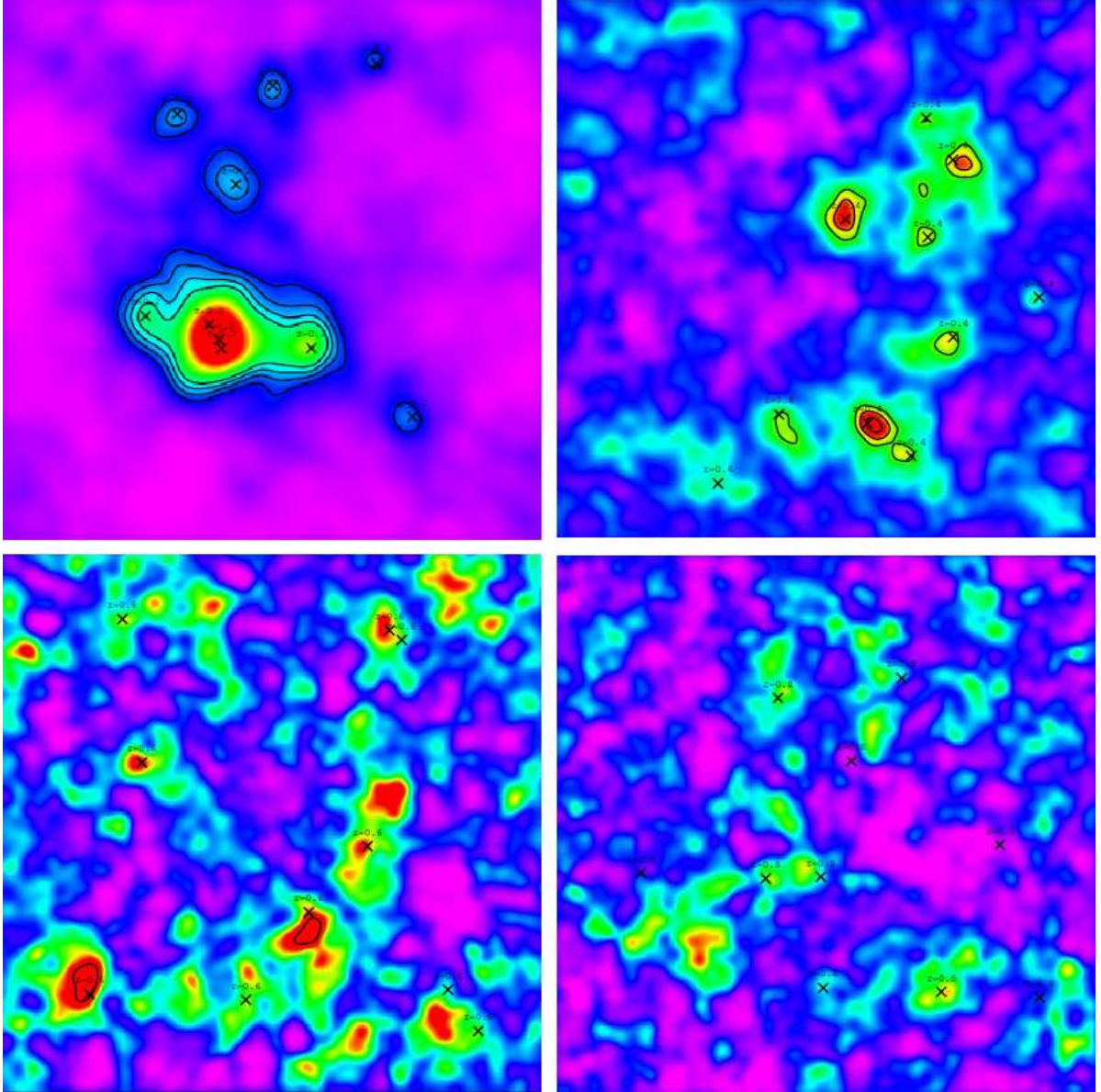
Figure 4.7: The filtering detection with SHUFF simulation SimW datasets. The mass of all the halos in the plots is $M_{200} = 10^{15} M_\odot$ and the redshift of clusters in each plots is the same as those in Fig.4.5.
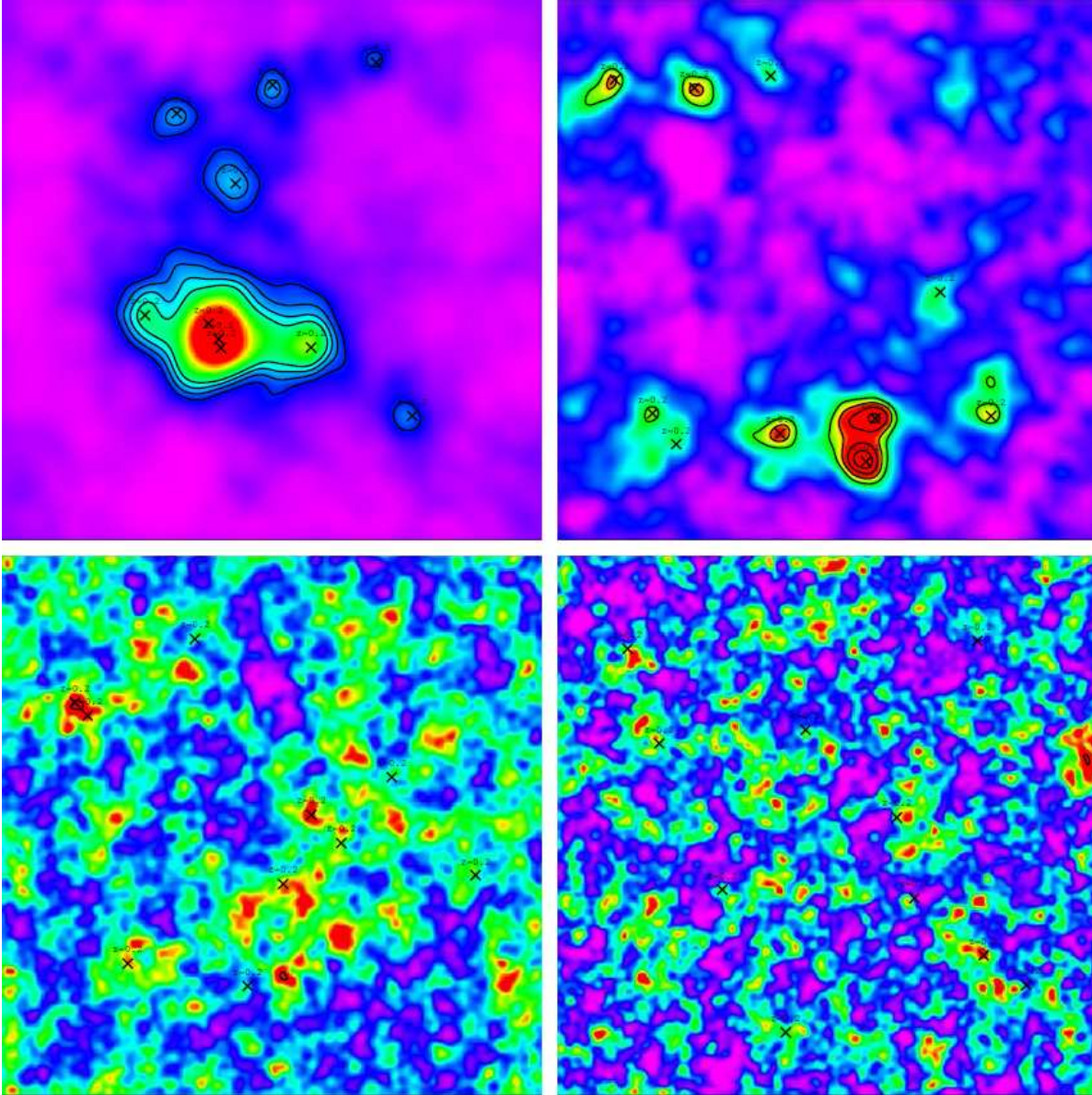
Figure 4.8: The filtering detection with SHUFF simulation SimW datasets. Similar to Fig.4.6 but all the clusters in the plots are at the same redshift $z_d = 0.2$
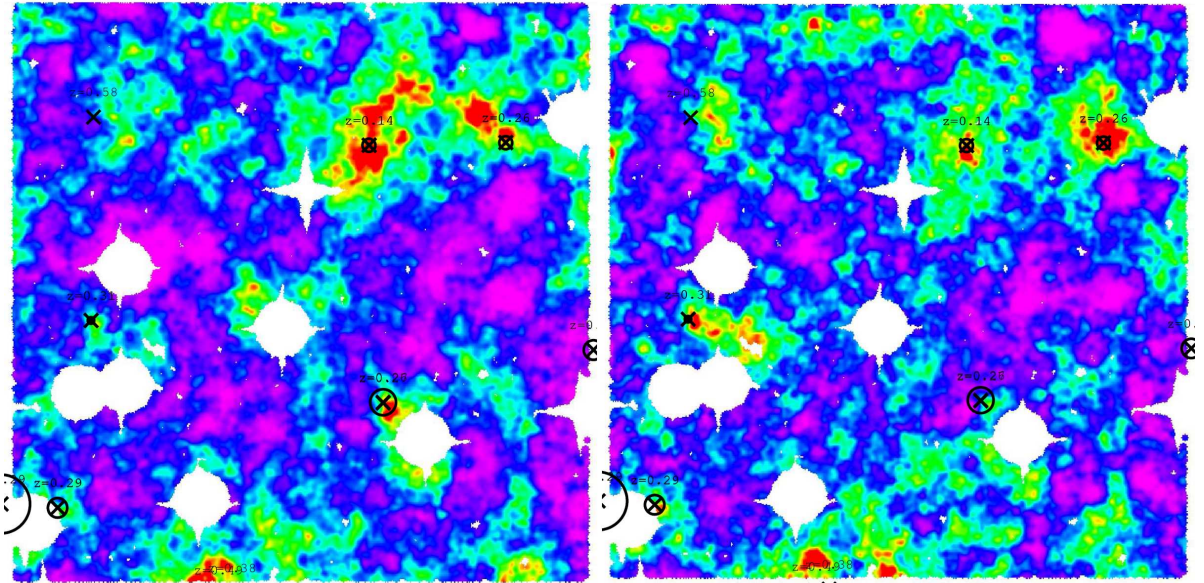
Figure 4.9: The filtering detection result for D1, with filter configured for NFW cluster with $M = 5 \times 10^{14} M_\odot$ at redshift $z_d = 0.2$ (*left plot*) and 0.4 (*right plot*). Also shown are the X-ray detected clusters as in Fig.4.4.
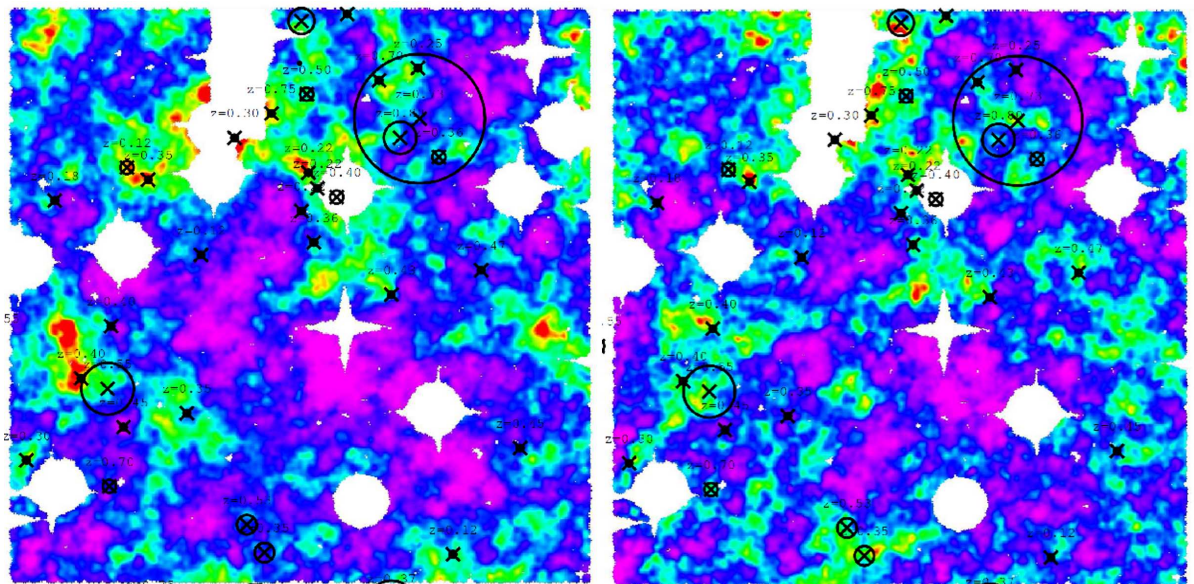
Figure 4.10: Similar to Fig.4.9 but for D2.
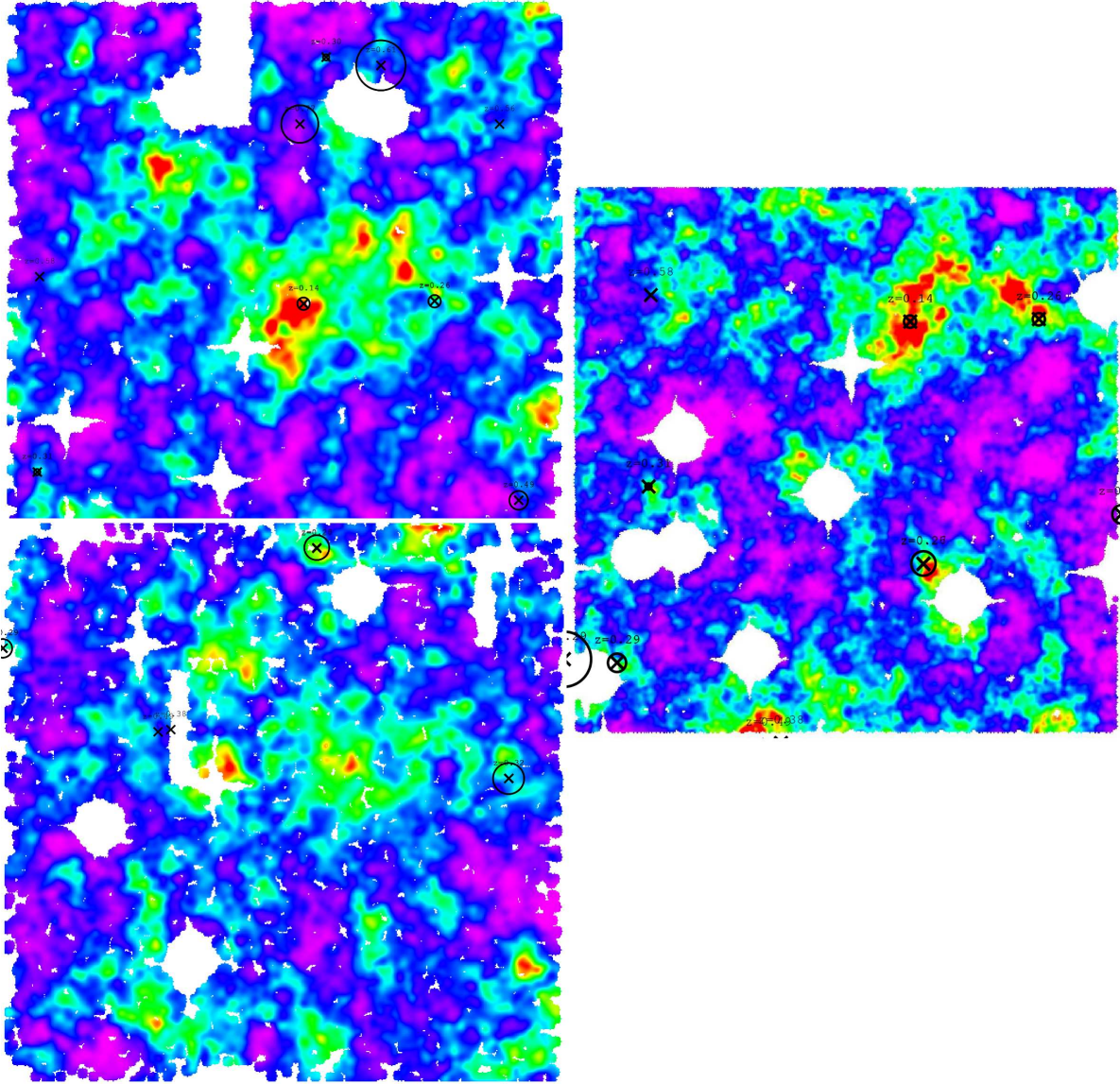
Figure 4.11: The filtering detection result for two pointings in W1p2p3 (*upper-left plot*) and W1p2p2 (*lower-left plot*), with filter configured for NFW cluster with $M = 10^{15} M_\odot$ at redshift $z_d = 0.2$. Besides X-ray detected clusters as in Fig.4.4, the detection map for D1 (Fig.4.9) is also shown for comparison with WCS coordinates matched.

Conclusion

We have shown that weak gravitational lensing is a powerful tool for the investigation of galaxy clusters. Instead of assuming the dynamical equilibrium state of the cluster, as in the case of X-ray approaches in cluster study, weak gravitational lensing relies only on the projected matter of the galaxy cluster, located between the observer and distant galaxies. From the statistical average of the distortion of the background galaxy images, the matter distribution of the individual cluster can be estimated. On the other hand, this method can also be used to search for galaxy clusters. As galaxy clusters are the largest and most massive gravitationally bounded systems in the Universe, their abundance and evolution provides important information for us to understand the structure formation history of our Universe.

However, we have seen (Chapter 1) that the detection of galaxy clusters with weak lensing is also challenging, as it depends on the signal to noise ratio of the cluster shear, observational conditions and good control over systematic errors. Naturally, the strength of shear signal is limited by the mass and redshift of the galaxy cluster. In addition, the cluster shear signal is estimated from the shape of background lensed galaxies which is intrinsically not circular and randomly oriented. Such instrinsic ellipticity dispersion introduces the intrinsic noise in the shear, which needs to be averaged out over a high density of lensed galaxies in a deep and large field observation. Furthermore, the galaxies in the field are not located at infinitely far distance, and the ratio D_{ds}/D_s moderates the strength of shear signals. Therefore a deep observation with large integration time is required to boost the sampling strength of the shear. Additional noises in the cluster shear are introduced from the cosmic shear, due to the cosmological weak lensing by the density perturbations along the line of sight, and the intrinsic shear, due to the local gravitational tidal force shearing on the galaxies. Apart from the theoretically expected noises above, in practice, there are also systematic errors in the measurement of the ellipticity of galaxy. The shape measurement of the background faint galaxies is generally noisy, and the anisotropy in PSF also introduces artificial shear. Thus one needs some algorithms to select stars in the image, and use some technical methods, *e.g.* KSB or Shapelets to correct the PSF and perform the shear measurement. Finally, the separation between foreground and background galaxies is needed to remove the contamination from the unlensed foreground galaxies: accurate photometric redshift, if available, can be used to properly scale the measured ellipticity of galaxies according to their redshift.

Regarding the challenges in the detection of galaxy clusters with weak lensing, in this thesis we aimed at the development of the methods to disentangle and evaluate these components. These methods are implemented in terms of three softwares, **as summarized below**.

In the wide field and long integration images, the presence of saturated stars is unavoidable. The result of saturation, in terms of reflection halos and diffraction spikes of very bright stars, seriously contaminates the shape measurement of galaxies. In Chapter 2, I discussed the physical reasons for these image defects, and how they are removed automatically with EXAM. The software selects the stars that are saturated and with spikes through the analysis of the measurements from SExtractor. The reflection halos are detected by the analysis of the background image. The mask profiles are scaled according to SExtractor measurements

and configurable with the optical features of the telescope taken into account. The mask of saturated stars can also be combined with the weight image to produce a master flag image in FITS format, which flags both the pixels in the saturation region, and the pixels in the image boundaries, CCD gaps and bad pixels. While the output ASCII region mask can be used to filter the detection and measurement in the galaxy catalog, the FITS flag image can be used with SEXTRACTOR to re-run the detection and measurement over the image. The software save the tedious work of manually masking the thousands of defects by looking into the image, and it is quite efficient with about 1 minute per square degree. ExAM has been applied to various telescopes like CFHT, Subaru and LBT. It is also integrated into the VST-tube pipeline, developed at INAF-OACN by A. Grado, aiming at the image processing of the coming VST data.

In order to reduce the systematic errors in the shape measurement and PSF correction, and to calibrate the method of cluster detection and mass estimation, a simulation approach is required, to simulate the shear signal from galaxy clusters, and shear noises as expected from theory, which can be yet separated from the systematic errors in the method. This was the goal of the Shuff code, discussed in Chapter 3. One possible approach would be to use N-body numerical simulations to describe the distribution of dark matter, and ray-tracing simulations for the lensing. Instead, in Shuff we use a simplified approach: a catalog of (unlensed) galaxies is first generated, e.g. using the E. Bertin' code STUFF, giving the galaxies' intrinsic shapes, positions in the field, redshifts and luminosities. Parameters as the redshift and spatial distribution can be further configured within SHUFF. The clusters are simulated as dark matter halos with analytical NFW/SIS profile, parametrized by their mass and concentration, triaxiality and redshift distribution. The cosmic shear noise is introduced with the slices of projected cosmological density field (realized as Gaussian random field), with the spatial correlation of the perturbation amplitude constrained by the cosmic shear power spectra calculated according to the redshift distribution of galaxies in the simulation. The intrinsic shear noise is introduced by a similar Gaussian random field but constrained by the intrinsic shear power spectra. SHUFF simulates the lensing effects, deflection, distortion and magnification, of multiple lens planes with galaxies continuously distributed in redshift. Compared to the ray-tracing simulation, the efficiency of SHUFF is obvious; for 1 square degree field of view, and galaxies with median redshift $z_m \sim 1$, it takes about 10 minutes for a run with complete effects. The output lensed galaxy catalog from SHUFF can be used either with SKYMAKER, developed by E. Bertin, to produce simulated images including instrumental effects for further shape measurement and PSF correction, or directly taken as already measured ellipticities and used for the cluster detection. Thus the difference between SHUFF ellipticities and measured one can be compared to calibrate the shear measurement method, while the simulation can be configured with different shear signal/noise properties for the investigation of cluster detection of weak lensing.

Finally, in Chapter 4 we discussed the software LENSFILTER, which I developed for the detection of cluster from a galaxy ellipticity catalog either from the simulation or from the measurement of the observational data. The detection implements an optimal filtering approach, derived from the signal and noise power spectra analysis in Fourier space. Compared to other empirical filters, *e.g.* Gaussian filter, in the literature, the optimal filter provided by LENSFILTER is configurable specifically for the observation conditions and with expected signal and noise properties, thus the detection is optimized, and limited only by the strength of the cluster shear signal and noise level. In addition to the galaxy ellipticities, a knowledge of their redshift distribution is needed: this is provided either by photometric redshifts, or by assuming a given redshift distribution, as configured by the user. The noise power spectra of the intrinsic ellipticity dispersion, cosmic shear, intrinsic shear and the correlation between cosmic

and intrinsic shear are then derived. According to the target cluster selected for detection, the shear signal of the cluster is analyzed with these noise power spectra in the Fourier space to build a digital filter, which is then convolved with the input ellipticity data field with DFT method, for a final output of detection S/N ratio map.

To investigate the limit of cluster detection, we have shown two sets of SHUFF simulations configured with source properties similar to that in the CFHTLS Deep (with galaxy number density $n \sim 1$ and median redshift $z_m \sim 1$) and Wide (with galaxy number density $n \sim 1$ and median redshift $z_m \sim 1$) observations. At the primary stage, we ignored the errors in the shear measurement and photometric redshift, and configured LENSFILTER with the same source properties and applied the filtering detection to the output galaxy ellipticties directly from SHUFF simulation as measured one. In this way, we investigate the detection limited only by the intrinsic properties of the shear signal and noise. We first found that for clusters with the mass $M \geq 5 \times 10^{14} M_\odot$ and redshift less than z_m, optimal filtering techniques implemented in LENSFILTER can successfully recover the clusters inputted in the simulations. With the decreasing of cluster mass and increasing of its redshift, the missing detection rate becomes higher and spurious detections also appear. We noticed that the successful detection of galaxy clusters is mainly subject to the observational depth relative to the redshift of the cluster, and the number density of the galaxies in the observations. With the errors in the shape measurement and redshift information introduced, the results are expected to deteriorate, which will be tested with on-going simulations. For the same data, the filtering result with Gaussian filter is compared and found to be comparable to the optimal filter only when the size of Gaussian filter is correctly guessed, but generally with more spurious features in the detection map.

We also applied the optimal filtering to the measured ellipticity catalog from publicly released CFHTLS images: to this end we compared results obtained from ovelapping pointings in the deep and wide (and shallow) components of this survey. The ellipticity catalog was obtained with the improved KSB pipeline, LensR, developed by M. Radovich. Since X-ray data taken with XMM are available in these fields, a comparison with X-ray detected clusters, available in literature, was also possible; the mass derived by X-ray data for these clusters is around $M \leq 2 \times 10^{14} M_\odot$ on average. From the optimal filtering detection result, we found some cluster detections matched with X-ray ones in the deep field, but only for low redshift and relatively massive clusters; there are more mismatches with X-ray detections in the wide fields partly due to the intrinsic shallower exposure depth and lower galaxy number density. Similarly, the matching of weak lensing detections in the overlapping Deep and Wide fields is limited to low redshift and relatively massive clusters. In addition, we recall that the errors in the shape measurement and photometric redshift also contribute to the mismatches and possible spurious cluster detections.

In the closing part of the thesis, I would like to mention that the papers with simulation and filtering results are in preparation. As a follow-up of this PhD thesis, I also plan to work on some further improvements of SHUFFand LENSFILTER. In the very next stage of SHUFF, I will proceed into two branches: (A) to introduce the halo mass function, and populate the analytical halos with their properties consistent with the cosmological context; (B) substitute the analytical models of the cluster halo with the dark matter halos extracted from the Millennium Simulation, and realize the background density perturbation field with the dark matter particles from that N-body simulation. With the currently framework of multiple lens planes and continous galaxies redshift distribution in SHUFF, these updates are straightforward. For the limit of cluster detection, we will apply the optimal filtering on the ellipticity catalog from SHUFFbut with the errors in the shear measurement and photometric redshift, in order to determine to what extent these errors affect in the method affects the detection results. In

addition, with the filtering detection result, a method of improved cluster mass estimation is being developed, featuring clusters with triaxiality and with substructures.

All these works are in preparation for the future cluster weak lensing studies based on ground-based wide field observations, such as VST-KIDS survey in 2011, and up-coming data from Subaru and LBT telescopes, as well as Euclid from space, in the long term. In the near future, with our robust methods in the cluster weak lensing well calibrated, more exciting results will be obtained both for the case-to-case study of individual cluster, and for statistical investigation of structure formation with cluster abundance and evolution.

Acknowledgments

At the end of the thesis, I would like to express my heartily gratitude to my supervisor, Dr. Mario Radovich. As my graduate work was on cosmology, CMB, and dark energy, I was complete new to weak lensing before I started my PhD program. In this three years, it is Dr. Radovich who leads me through the weak lensing theories, observational data reduction, and program development for weak lensing analysis. Meanwhile, he always leaves me the freedom to think and work on my own with all my PhD works. About those three programs I developed for this thesis work, I would thank him for the useful, sometimes time-consuming, discussion and cross-checking. I also owe my gratitude to him for the careful reading and correction of this thesis. I would like to say it has been my great pleasure to work with him for these three years.

Meanwhile, I would like to thank Dr. Aniello Grado in INAF-Osservatorio Astronomico di Capodimonte , for the instructions on the aspect of practical image reduction, and helpful discussion about some algorithms in the programs I developed. I am grateful to Liping Fu, Emanuella Puddu, Fedor Getman, Luca Limatola and other colleagues in INAF-OAC for the pleasant collaboration during my three years in Naples.

I would like to sincerely thank Prof. Chenggang Shu in Shanghai Normal University, and Prof. Dr. Yannick Mellier in Institut d'Astrophysique de Paris. Without their support, I may not get such a good opportunity to study abroad.

Finally I would like to thank my parents, who are always supporting me, and who have undertaken a lot.

Appendix A

Program Helps: Installation, Usage and Configuration file

The softwares I wrote and developed for my PhD thesis work follow the same similar approach for installation, configuration and usages. Thus I briefly summarize the similar steps here, while for each of the software, I list the configuration file in seperate sections.

A.1 Installation

All the packages will be available in the near future on `www.oacn.inaf.it/duel_inaf`

The installation precedure for all three softwares follows quite the same steps. Once you download the software, you may first uncompress the tarball with:

% `tar xvzf softwarename-n.m.tar.gz`

Then you may go into the folder named `softwarename-n.m`, and configure and compile the program with:

% `./configure`
% `make`

Depending on whether you have the root privilege, you may wish to use the compiled binary `softwarename` directly, or proceed further to generate a system-wide executable with

% `make install`

All the softwares are written in ANSI C language, and the compilation of the softwares assumes minimal dependence on the external libraries. Thus the least publically common library you need is the GSL Scientific Library, available at,

`http://www.gnu.org/software/gsl`

the CFITSIO, a FITS file subroutine library, available at,

`http://heasarc.gsfc.nasa.gov/fitsio`

and the FFTW for computing discrete Fourier transform, available at,

`http://www.fftw.org/`

A.2   Usage

The usage of my softwares follows similar style as those of E. Bertin's software, *e.g.* SEXTRACTOR. The basic syntax for the running is

% `softwarename` [`-c` *configuration file*] [*–keyword_1 value_1*] [*–keyword_2 value_2*] ...

The bracket parts are optional. The keywords are list in the configuration file for each software in sections below, and are in TYPEWRITTER font throughout this thesis. Each keyword appended to the executable after the configuration file overrides the corresponding default configuration with the following value(s). The format of the keyword value can be string, double, or boolean, either single valued or in array, according to the specification of the keyword. In case of values in array, they are separated by coma(s), and the user may want to quote the values with single or double quotation marks, to avoid messing up with shell command syntax. The advantage of the command syntax here is the flexibility to embed the configuration and running in a script, as well as to configure some of the keywords in command line.

By default, the software looks for a default configuration file named `softwarename.cfg` in the local directory. Optionally the configuration file can be specified in the command line after "`-c`". The default configuration can be dumped with,

% `softwarename -d`

In what follows, we will list the default configuration files for ExAM, Shuff and LensFilter, respectively.

A.3   configuration file of ExAM

```
    #-------------- In/Out -----------------------------------------------


RUN_MODE        MASK                # Running mode (MASK/GUESS/LEARN)
SEXCAT_IN       incat.sex           # Input sextractor catalogue
MASK_REG        mask.reg            # Output mask region name
SEXCAT_OUT      NONE                # Output sexcat name or NONE


#-------------- Guess -------------------------------------------------


GUESS_REG       guess.reg           # Output guess region name
GUESS_HNUM      1,10                # Guess at halo number (main/sub/...) (3)
GUESS_HRAD      1040,380            # Guess at halo radius (main/sub/...) (3)


#-------------- Learn -------------------------------------------------


LEARN_REG       learn.reg           # Output learn region name


#-------------- Aureole -----------------------------------------------


HALO_NUM        5                   # Number of most bright aureoles
HALOA_OFFC      10475.0,11620.0 # Aureole offset center (2 XY)
HALOA_OFFF      0.022               # Aureole offset factor (2 XY)
HALOA_RAD       990.0               # Aureole radius (2 AB)
```

```
HALOA_ANG       0.0                 # Aureole position angle (deg) if ellip.
HALOB_OFFC      1024,1024           # Sub-aureole Offset center (2 XY)
HALOB_OFFF      0.022               # Sub-aureole offset factor (2 XY)
HALOB_RAD       450.0               # Sub-aureole radius (2 AB)
HALOB_ANG       0.0                 # Sub-aureole position angle (deg) if ellip.
VOID_OFFC       7928.5,11550.2      # Void Offset center (2 XY)
VOID_OFFF       0.028               # Void offset factor (2 XY)
VOID_RAD        462.9,408.4         # Void radius (2 AB)
VOID_ANG        0.0                 # Void position angle (deg) if ellip.


#------------- Saturation and Spikes(max=2(R),4(D)) ----------------------

STAR_RADF       1.5                 # Stellar core region radius scaling
SPKR_TTYPE      PERI                # R-Spk thresh.type: PERI/AREA/MIN/MAX
SPKR_THRESH     18.0                # Readout spike threshold
SPKR_STYPE      PERI                # R-Spk scal.type: PERI/AREA/MIN/MAX (2 LW)
SPKR_SLEN       1.5                 # R-Spk length scaling (1:ALL; 2:HV; 4:ENWS)
SPKR_SWID       0.0                 # R-Spk width scaling (1:ALL; 2:HV)
SPKD_TTYPE      PERI                # D-Spk thresh.type: PERI/AREA/MIN/MAX
SPKD_THRESH     18.0                # Diffuse spike threshold
SPKD_STYPE      PERI                # D-Spk scal.type: PERI/AREA/MIN/MAX (2 LW)
SPKD_SLEN       1.5                 # D-Spk length scaling (max 4 Anticlock)
SPKD_SWID       1.5                 # D-Spk width scaling (max 4 Anticlock)
SPKD_ANG        0.0                 # D-Spk pos.ang.(max 4 Anticlock)


#------------- Regions ---------------------------------------------------

REG_SEXFLAG     8                   # Max FLAGS for regions
REG_SGUNSAT     0.8                 # Min CLASS_STAR for regions of unsat stars
REG_SGSAT       0.5                 # Min CLASS_STAR for regions of sat stars
REG_EXCLUDE     Y                   # Region property EXCLUDE/INCLUDE
REG_LABEL       Y                   # Label region with (PERI/AREA/SFLAG)
REG_COLOR       yellow              # Region color (in ds9 convention)


#------------- Flag image ------------------------------------------------

FLAG_TYPE       NONE                # Flag image type (NONE/ALL/WT/REG)
FLAG_NAME       flag.fits           # Output flag image
FLAG_TRUE       Y                   # Flag bad pixels with 1
FWT_TYPE        NONE                # Weight flag threshold type (NONE/ABS/QNT)
WT_NAME         weight.fits         # Input weight image
WT_SAMPLING     200,200             # Sampling of weight image (2)
WT_THRESH       0.005               # Threshold of weight value
FRG_TYPE        NONE                # Region flag type (NONE/INT/EXT)
EXT_REG         mask.reg            # External mask region name


#------------- Borders (max=4) -------------------------------------------

BORD_TYPE       NONE                # NONE, MANUAL(, AUTO)
```

```
BORD_MARGIN      200,200            # MANUAL border margin (1:ALL;2:HV;4:ENWS)


#------------- Miscellaneous --------------------------------------------------


VERBOSE_TYPE     NORM               # QUIET, NORM or FULL
```

A.4   configuration file of SHUFF

```
   #----------------------- In/Out Catalogs -------------------------------------


ICAT_LEN        lens.inp           # Input lens list
ICAT_GAL        gals.inp           # Input Stuff galaxy list
ICAT_LSS        plss.inp           # Input LSS kappa power spectrum
OCAT_LEN        lens.cat           # Output lens list (updated)
OCAT_GALI       gal0.cat           # Output unlensed galaxy list (updated)
OCAT_GALO       gal1.cat           # Output lensed galaxy list


#----------------------- Checks and Plots ------------------------------------


OMAP_KALL       kall.fits          # Output summed projected map
OMAP_ZMOD       FIX                # Output map source z mode (QNT/MAX/FIX)
OMAP_ZS         10.0               # Output map source z (Z_MODE=FIX,QNT)
OCAT_CHK        check.cat          # Output check list
REG_GALI        stuff.reg          # Output Stuff galaxy region file (input)
REG_GALO        shuff.reg          # Output Shuff galaxy region file (output)
REG_SCL         3.0                # Scaling of region galaxy contour size
CMAP_TYPE       NONE               # Other check maps for each LP, max.16
# Options: NONE/ALL/K/P/KR/GM1/GM2/GMM/
# A1/A2/AM/F/RG1/RG2/RGM/B1/B2/BM


#----------------------- Lens Controls ---------------------------------------


LNS_MODE        ALL                # Lens mode (ALL/GCL/LSS)
CLS_DMIN        1                  # Min dens contrast at max cluster extension
CLS_RMIN        10                 # Min flattern radius of cluster (kpc)
CLS_ZSFRAC      0.1                # Dds/Dd of min redshift to apply lensing
LSS_SEED        1                  # Random seed for LSS kappa random field
WL_KMAX         0.1                # Maximum kappa to for weak lensing
WL_RGMAX        0.1                # Maximum reduced shear to for weak lensing
IAE_MODE        LIN                # Intrin. Align. mode (OFF/LIN)
IAE_FACT        -0.0134            # Strength of IA (A_MODE=LIN/FIX[-1,1])
LP_DZMAX        0.1                # max dz between LPs (usu. =dz_lss)
LP_ZMAX         10.0               # Max redshift of lens plane (quick test)
LP_ZMIN         0.0                # Min redshift of lens plane (quick test)


#----------------------- Source Controls -------------------------------------


SRC_MODE        STF                # Mode of source galaxies (STF/MOC/MIX)
```

```
POS_MODE        RND             # Position dist. (RND/GRD) (S_MODE=MOC)
ELP_MODE        STF             # Ellipticity distribution (STF/RND/FIX)
ZSD_MODE        STF             # Redshift distribution (STF/FIX/LUD/JNB/YMK)
#   LUD: (z*1.4/a)b̂*exp(-(z*1.4/a)ĉ)
#   JNB: zâ/(zb̂+c)
#   YMK: (zâ+z^(ab))/(zb̂+c)
MOCK_ZPM        2.0             # Mock z parameters (zs or a,b,c) (max 3)
ZSD_SEED        1               # Random seed of redshift dist.
POS_SEED        1               # Random seed of uniform pos. dist.
ELP_SEED        1               # Random seed of gauss ellip. dist.
MOCK_DENS       30              # Mock source density (per arcmin2̂)
MOCK_ESIG       0.3             # Mock ellipticity dispersion (E_MODE=RND)
MOCK_BR         0.89            # Mock bulge axial ratio (E_MODE=FIX)
MOCK_BA         0.0             # Mock bulge pos. angle (deg) (E_MODE=FIX)
MOCK_DR         0.74            # Mock disk axial ratio (E_MODE=FIX)
MOCK_DA         0.0             # Mock disk pos. angle (deg) (E_MODE=FIX)
MOCK_M          23              # Mock single magnitude (-1=STUFF)
MOCK_BT         0.18            # Mock bulge/total mag ratio (-1=STUFF)
MOCK_GT         +1              # Mock galaxy type (-1=STUFF)
MOCK_BS         0.18            # Mock bulge size (arcsec) (-1=STUFF)
MOCK_DS         0.40            # Mock disk size (arcsec) (-1=STUFF)


#----------------------- Cosmology ----------------------------------------


COSMO_H0        0.714           # Hubble constant (100*km/s/Mpc)
COSMO_OM        0.262           # Matter density in critical density
COSMO_OL        0.738           # Cosmol constant in critical density


#----------------------- Map Dimensions -----------------------------------


SIZE_PIX        0.186           # pixel scale (arcsec/pixel)
SIZE_FOV        19500           # Width,[height] of the input fov
SIZE_MAP        256             # Width,[height] (even) of the output maps
SIZE_EXT        256             # Extended margin width
SIZE_PAD        256             # Zero padding margin width


#----------------------- Miscellaneous ------------------------------------


VERBOSE_TYPE    NORMAL          # QUIET, NORMAL or FULL
```

A.5   configuration file of LENSFILTER

```
   #----------------------- In/Out Catalogs -------------------------------
IDAT_P3D        p3d.inp         # Input 3d density power spectra
IDAT_GLS        gls.inp         # Input galaxy shear cat: x,y,e1,e2,w(,z)
#   if no z, only BG galaxies in input cat!
ODAT_P2D        p2d.out         # Output 2d shear power spectra
```

```
ODAT_PCL          pcl.out           # Output cluster shear profile
ODAT_PSM          psm.out           # Output 2d shear power spectra for SHUFF
#----------------------- Cosmology -------------------------------------
COSMO_H0          0.714             # Hubble constant (100*km/s/Mpc)
COSMO_OM          0.262             # Matter density in critical density
COSMO_OL          0.738             # Cosmol constant in critical density
#----------------------- Lens Controls --------------------------------
GCL_MODEL         NFW               # Halo density model (NFW/SIS)
GCL_Z             0.2               # Redshift of galaxy cluster
GCL_ZSFRAC        0.1               # Dds/Dd of min redshift to apply lensing
GCL_PARAM         1e0,6.0,200,1.0   # The params of clusters
#    NFW: M200(10^14Msun), c, Dvir, n
#    SIS: v(km/s)
GCL_KMAX          0.9               # Maximum kappa for weak lensing
GCL_RGMAX         0.9               # Maximum reduced shear for weak lensing
GCL_DMIN          1                 # Cluster boundary density contrast
GCL_TMIN          1e-16             # Radial sampling theta min (rad)
GCL_TMAX          1e16              # Radial sampling theta max (rad)
GCL_NT            1000              # Radial sampling number
GCL_NTP           1                 # Radial oneside zeropad/sampling ratio
#----------------------- Source Controls ------------------------------
SZD_MODE          LUD               # Source z dist. (LUD/JNB/YMK/FIX/BIN)
#    FIX: single source plane
#    LUD: (1.4*z/a)^b*exp(-(1.4*z/a)^c)
#    JNB: z^a/(z^b+c)
#    YMK: (z^a+z^(ab))/(z^b+c)
#    BIN: IDAT_GLS must contain z col.
#    !BIN: only BG galaxies in IDAT_GLS
SZD_NZPRM         0.64,2.0,1.5      # n(z) parameters (for zs or a,b,c above)
SZD_ZMIN          -1                # n(z) zmin cut (-1=zsmin)
SZD_ZMAX          5.0               # n(z) zmax cut e.g. 5.0
GBL_NBIN          500               # Global number of redshift bins
GBL_ZMIN          0.0               # Global min redshift bin
GBL_ZMAX          5.0               # Global max redshift bin
#----------------------- Noise Controls -------------------------------
PIX_SIZE          0.186             # Image pixel scale in arcsec/pixel
FOV_NPIX          19355             # Image pixel dimension in pixel [2]
FOV_RRA           180,0             # Reference point WCS coordinate (RA,DEC)
FOV_RDEC          0,0               # Reference point WCS coordinate (RA,DEC)
FOV_RPIX          9677.5            # Reference point pixel coordinate [2]
P2D_MODE          TEO               # 2d noise power spectra mode (TEO/SIM)
P2D_NN            3                 # Noise component (0-3) for filter
#    0: Gaussian filter
#    1: IE (intrin. ellip. disp.) only
#    2: IE + CS (cosmic shear)
#    3: IE + CS + IA (intrin. align.)
P2D_LMIN          2.0               # min ell for 2d power spectra
P2D_LMAX          1e7               # max ell for 2d power spectra
P2D_NL            100               # number of ells for 2d power spectra
```

```
P3D_MODE        NLN                 # Type of p3d (NLN/LIN) for p2d projection
GAL_ESIG        0.2                 # Intrin. dispersion of galaxy ellpticity
GAL_ETYP        Y                   # If input e=(Q11-Q22+2Q12*i)/(Q11+Q22+2A)
IA_FACT         -0.0134             # Linear IA model normal. factor
IA_KCUT         1.0                 # kmax for IA (h/Mpc)
#---------------------- Output Controls ------------------------------
MAP_NPIX        256                 # Mass map sampling dimension (even)
#---------------------- Miscellaneous --------------------------------
VERBOSE_TYPE    NORMAL              # QUIET, NORMAL or FULL
```

Appendix A

Discrete Fourier Transform with FFTW and Its Application in Convolution

A.1   Two dimensional DFT with FFTW

A function $f(\mathbf{x})$ defined in $\mathcal{R}^2$ and its Fourier transform $\hat{f}(\mathbf{k})$ are related with

$$\hat{f}(\mathbf{k}) \quad = \quad \int_{-\infty}^{\infty} \mathrm{d}^2 x \, f(\mathbf{x}) \, \mathrm{e}^{-\mathrm{i}\mathbf{k}\mathbf{x}} \,, \tag{A.1}$$

$$f(\mathbf{x}) \quad = \quad \frac{1}{(2\pi)^2} \int_{-\infty}^{\infty} \mathrm{d}^2 k \, \hat{f}(\mathbf{k}) \, \mathrm{e}^{+\mathrm{i}\mathbf{k}\mathbf{x}} \,. \tag{A.2}$$

The normalization factor is chosen such that when $f(\mathbf{x}) = 1$, $\hat{f}(\mathbf{k}) = (2\pi)^2 \, \delta(\mathbf{k})$, due to the properties of 2 dimensional Dirac function,

$$\int_{-\infty}^{\infty} \mathrm{d}^2 x \, \mathrm{e}^{-\mathrm{i}\mathbf{k}\mathbf{x}} \quad = \quad (2\pi)^2 \, \delta(\mathbf{k}) \,, \tag{A.3}$$

$$\int_{-\infty}^{\infty} \mathrm{d}^2 k \, \delta(\mathbf{k}) \, \mathrm{e}^{+\mathrm{i}\mathbf{k}\mathbf{x}} \quad = \quad 1 \,. \tag{A.4}$$

However, in practise, a function can never be fully sampled in $\mathcal{R}^2$, with infinity high resolution. So one has to sample the function within the finite range and with finite number of points, and Fourier transform of such a sampled function is called discrete Fourier transform (DFT). Since DFT assumes the function sampled contains the full information of the original function, which is only true when the sampling range contains a full period of a originally periodical function, and a sufficient number of data points are sampled so that no higher frequencies are missing. Thus, the sampling range and frequency are crucial to reconstruct the original function, and usually large sampling number and zeropadding to the samping range is needed.

For simplicity to formulate DFT, we start with one dimensional function $f(x)$, which is linearly sampled by M data points $x_m = m\Delta x$ ($m = 0, \ldots, M-1$) in range $x \in [0, P]$. The spaital resolution of the sampled function $f_m = f(x_m)$ is $\Delta x = P/M$. In Fourier space, the frequency resolution is limited by the finite sampling range P, $\Delta k = 2\pi/P$, and the highest frequency (Nyquist frequency) is limited by the finite resolution of sampling Δx, $k_{\max} = 2\pi/\Delta x = 2\pi \, M/P$. In other words, the Fourier transform $\hat{f}(k)$ is sampled at frequencies $k_j = j\Delta k$ ($j = 0, \ldots, M-1$) in range $k \in [0, 2\pi \, M/P]$. Thus discrete Fourier transform pair

reads,

$$\hat{f}_j = \Delta x \sum_{m=0}^{M-1} f_m \, e^{-i\,k_j x_m} = \frac{P}{M} \sum_{m=0}^{M-1} f_m \, e^{-i(2\pi/M)mj} \tag{A.5}$$

$$f_m = \frac{\Delta k}{2\pi} \sum_{j=0}^{M-1} \hat{f}_j \, e^{+i\,k_j x_m} = \frac{1}{P} \sum_{j=0}^{M-1} \hat{f}_j \, e^{+i(2\pi/M)mj} \tag{A.6}$$

The tranfrom becomes the continuous Fourier transform in the limit when $M \to \infty$. Also the periodicity can be seen from $f_{m+M} = f_m$ and $\hat{f}_{j+M} = \hat{f}_j$, as expected. Note that the Fourier transform $\hat{f}_j$ are generally complex numbers. If the original data f_m's are real, *e.g.* sampled from real signal, $\hat{f}_j$ have some symmetries due to the properties of complex conjugation, $\hat{f}_{M-j} = \hat{f}_j^*$. It is for this reason that, for the transform of a real function, only nearly half of the Fourier components need to be calculated, namely only $(M/2 + 1)$ $\hat{f}_j$'s with $j = 0, \ldots, M/2$.

In the case of two dimensional DFT, all those properties mentioned above can be easily generalized. Here we explicitly give these formulae,

$$\hat{f}_{jk} = \frac{P}{M}\frac{Q}{N} \sum_{m=0}^{M-1} \sum_{n=0}^{N-1} f_{mn} \, e^{-i\left(\frac{2\pi}{M}mj + \frac{2\pi}{N}nk\right)} \tag{A.7}$$

$$f_{mn} = \frac{1}{P}\frac{1}{Q} \sum_{j=0}^{M-1} \sum_{k=0}^{N-1} \hat{f}_{jk} \, e^{+i\left(\frac{2\pi}{M}mj + \frac{2\pi}{N}nk\right)} \tag{A.8}$$

where the new indice introduced for the second dimension can be understood analogously. In real and Fourier space, the sampling resolutions and maximum ranges read,

$$\Delta x_1 = \frac{P}{M}, \quad \Delta x_2 = \frac{Q}{N}; \qquad x_1^{\max} = \frac{2\pi}{\Delta k_1}, \quad x_2^{\max} = \frac{2\pi}{\Delta k_2};$$

$$\Delta k_1 = \frac{2\pi}{P}, \quad \Delta k_2 = \frac{2\pi}{Q}; \qquad k_1^{\max} = \frac{2\pi}{\Delta x_1}, \quad k_2^{\max} = \frac{2\pi}{\Delta x_2}. \tag{A.9}$$

The periodicity in two dimensional DFT can be easily shown as,

$$\hat{f}_{j,k} = \hat{f}_{j\pm M,k} = \hat{f}_{j,k\pm N} = \hat{f}_{j\pm M,k\pm N}. \tag{A.10}$$

If f_{mn}'s are real, the Fourier components follow the conjugation relations,

$$\hat{f}_{M-j,N-k} = \hat{f}_{j,k}^*. \tag{A.11}$$

There are two special cases that can be derived from the above conjugation relation.

- $j = 0$ and/or $k = 0$,
$$\hat{f}_{M-j,0} = \hat{f}_{j,0}^*, \quad \hat{f}_{0,N-k} = \hat{f}_{0,k}^*, \tag{A.12}$$
  from which three special Fourier components are found to be purely real,
$$\hat{f}_{0,0} = \hat{f}_{0,0}^*, \quad \hat{f}_{M/2,0} = \hat{f}_{M/2,0}^*, \quad \hat{f}_{0,N/2} = \hat{f}_{0,N/2}^*. \tag{A.13}$$

- $j = M/2$ and/or $k = N/2$,
$$\hat{f}_{M-j,N/2} = \hat{f}_{j,N/2}^*, \quad \hat{f}_{M/2,N-k} = \hat{f}_{M/2,k}^*, \tag{A.14}$$
  from which another special Fourier component is found to be purely real,
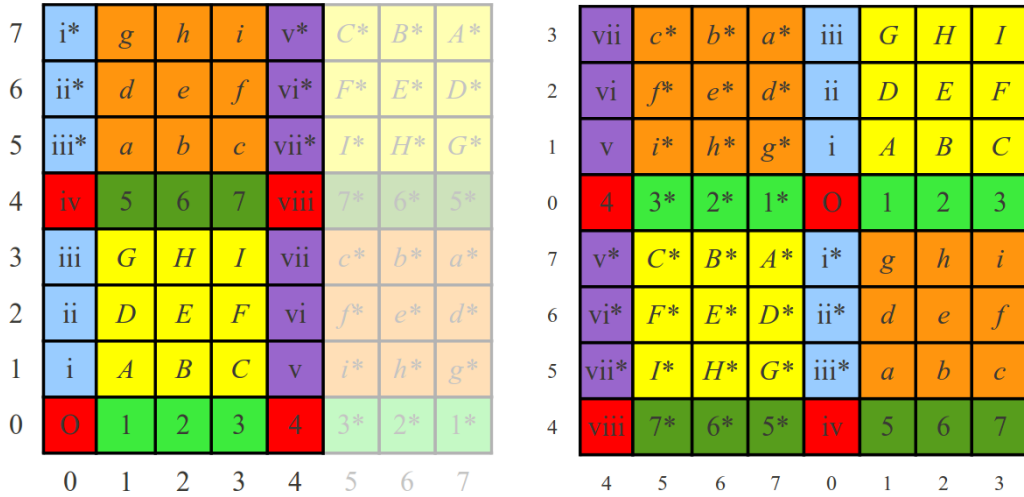$$\hat{f}_{M/2,N/2} = \hat{f}_{M/2,N/2}^*. \tag{A.15}$$

Figure A.1: The quadrant-swapped layout of Fourier domain in FFTW (*left plot*) compared with normal origin centered layout (*right plot*) for a Fourier transform of *real* 8×8 two dimensional array. The numbers outside of plots are the indice of pixel, or can be understood as the discrete sampling frequencies ℓ. Blocks in red are purely real, with **O** as the D.C. point and **viii** the Nyquist frequency. Other colorful blocks and letters therein indicates the complex conjugation relations. Due to the symmetry introduced by the complex conjugation, only slightly more than half of the Fourier components are calculated in FFTW, with the symmetric part in fade colors in the left plot.

Given that the original data is real, the relations above form the complete set of symmetry in two dimensinal DFT, which is illustrated in Fig.A.1

The DFT, implemented in the codes in the thesis work, is realized with FFTW[*], a public C library for computing discrete Fourier transform. Generally, any FFT library has its own convention in the normalization factor, arrangement of Fourier space quadrants, and symmetry in the defition of Fourier frequency range. As a reference, the special conventions used in FFTW are declared below.

- What FFTW really computes and the normalization convention. Similar to the formulism developed above, the exact formulae for forward (Real space to Fourier space) and backward (Fourier space to Real space) DFT implemented in FFTW read

$$\hat{f}_{jk} \;=\; \sum_{m=0}^{M-1}\sum_{n=0}^{N-1} f_{mn}\, \mathrm{e}^{-i\left(\frac{2\pi}{M}mj+\frac{2\pi}{N}nk\right)} \tag{A.16}$$

$$f_{mn} \;=\; \sum_{j=0}^{M-1}\sum_{k=0}^{N-1} \hat{f}_{jk}\, \mathrm{e}^{+i\left(\frac{2\pi}{M}mj+\frac{2\pi}{N}nk\right)} \tag{A.17}$$

  Thus, compared to the DFT formulae above, the data gets amplified by $M \times N$ after transformed first to Fourier space and then transformed back. Thus a normalization factor $1/(MN)$ needs to be applied after the backward transform.

- The swapping of frequency quadrants. FFTW computes the DFT of original data f_{mn} in frequency range $k_1 \in [0, (M-1)2\pi/P]$, $k_2 \in [0, (N-1)2\pi/Q]$, *i.e.* $\hat{f}_{jk}$ are sampled on

[*]http://www.fftw.org/

$M \times N$ grid in Fourier space, with $(0, 0)$ origin in the lower-left corner of the Fourier plane, or in the beginning of the complex data arrray. Compared with the $(0, 0)$-centered Fourier quadrants arrangement, the quadrant swapping convention is illustrated in Fig.(??). In short, due to the periodicity, the negative frequencies are just those positive ones but arranged in inversed order $\hat{f}_{-j,-k} = \hat{f}_{M-j,N-k}$.

- Fourier transform of real input data. In FFTW, input and output data are stored in "row-major" order. For example, one $M \times N$ two dimension array is stored row-by-row, *i.e.* starting from first row, filling each columns and then moving to the second row, etc. Thus a data point at (i, j) has the index $i + M \times j$. In FFTW, the dimension that is changing most frequently is dubbed the "last" dimension, in 2d case, x. When the input data f_{mn}'s are real, due to the symmtries in conjugation relation $\hat{f}_{M-j,N-k} = \hat{f}^*_{j,k}$, only slightly more than half of the Fourier domain is calculated in FFTW. Specifically, according to the "row-major" order, in the last dimension (x), only the first $(M/2 + 1)$ data points (columns) are calculated and stored with $i = 0, \ldots M/2$, while in the first dimension (y), all N rows are stored.

A.2   Convolution with FFTW

In mathematics, the convolution of two functions of two dimension $f(\mathbf{x})$ and $g(\mathbf{x})$ is defined as,

$$(f * g)(\mathbf{x}) = \int f(\mathbf{x}')g(\mathbf{x} - \mathbf{x}')\mathrm{d}^2x = \int f(\mathbf{x} - \mathbf{x}')g(\mathbf{x}')\mathrm{d}^2x . \tag{A.18}$$

Substitute $f(\mathbf{x})$ and $g(\mathbf{x})$ with their Fourier transform,

$$f(\mathbf{x}) = \frac{1}{(2\pi)^2} \int \mathrm{d}^2k \hat{f}(k)\mathrm{e}^{+i\,\mathbf{k}\mathbf{x}} , \tag{A.19}$$

$$g(\mathbf{x}) = \frac{1}{(2\pi)^2} \int \mathrm{d}^2k \hat{g}(k)\mathrm{e}^{+i\,\mathbf{k}\mathbf{x}} , \tag{A.20}$$

the convolution $(f * g)(\mathbf{x})$ can be rewritten as,

$$(f * g)(\mathbf{x}) = \frac{1}{(2\pi)^4} \int \mathrm{d}^2k \int \mathrm{d}^2k' \int \mathrm{d}^2x \hat{f}(\mathbf{k}')g(\mathbf{k})\mathrm{e}^{+i\,\mathbf{k}'\mathbf{x}'}\mathrm{e}^{+i\,\mathbf{k}\mathbf{x}}\mathrm{e}^{-i\,\mathbf{k}\mathbf{x}'}$$

$$= \frac{1}{(2\pi)^2} \int \mathrm{d}^2k \int \mathrm{d}^2k' f(\mathbf{k}')g(\mathbf{k})\delta(\mathbf{k} - \mathbf{k}')\mathrm{e}^{+i\,\mathbf{k}\mathbf{x}} \tag{A.21}$$

$$= \frac{1}{(2\pi)^2} \int \mathrm{d}^2k f(\mathbf{k})g(\mathbf{k})\mathrm{e}^{+i\,\mathbf{k}\mathbf{x}} , \tag{A.22}$$

which is just the Fourier transform of $\hat{f}(\mathbf{k})\hat{g}(\mathbf{k})$. Thus the Fourier transform of the convolution of two functions is the complex products of the Fourier transform of two functions, which is usually called the *convolution theorem*. Since the Fourier transform can be done with well developed algorithm in the public available libraries, *e.g.* FFTW, the computation of convolution can be greatly simplified.

In the discrete case, if we want to perform a convolution of the data D_{mn} with filter F_{mn}, both of which are $M \times N$ two dimensional data, with FFTW library we can proceed as follows. First, apply the Fourier transform of D_{mn} into Fourier domain $\hat{D}_{mn}$. From the definition of the convolution, it is easy to notice the asymmetry of two functions in the real space, *i.e.* one of the function is defined *w.r.t.* its origin as it involves $\mathbf{x} - \mathbf{x}'$. Here we choose the filter as the special one. In FFTW, due to the convention that the origin of data starts from the corner,

if the filter is built centered in the middle of the map, we need to swap the quadrants of the filter in real space as follows,

$$F'_{m'n'} = F_{m'n'} \quad \begin{cases} m > M/2 & ? \quad m' = m + M/2 \quad : \quad m' = m - M/2 \\ n > N/2 & ? \quad n' = n + N/2 \quad : \quad n' = n - N/2 \end{cases} . \tag{A.23}$$

After the swapping, we can Fourier transform F'_{mn}, and readily applied the complex (point-wise) product in the Fourier domain, and Fourier transform back to get the convolved data D'_{mn},

$$D'_{mn} = \frac{1}{MN} \sum_{j=0}^{M} \sum_{k=0}^{N} \hat{D}_{jk} \hat{F}'_{jk} e^{+i\left(\frac{2\pi}{M}mj + \frac{2\pi}{N}nk\right)} . \tag{A.24}$$

The normalization factor $1/(MN)$ is explained in the previous section.

Bibliography

Abramowitz, M. & Stegun, I. A. 1964, Handbook of Mathematical Functions with Formulas, Graphs, and Mathematical Tables, ninth dover printing, tenth gpo printing edn. (New York: Dover)

Andreon, S., Quintana, H., Tajer, M., Galaz, G., & Surdej, J. 2006, MNRAS, 365, 915

Andreon, S., Willis, J., Quintana, H., et al. 2004, MNRAS, 353, 353

Bartelmann, M. 1996, A&A, 313, 697

Bate, N. F., Fluke, C. J., Barsdell, B. R., Garsden, H., & Lewis, G. F. 2010, Nature, 15, 726

Bertin, E. 2009, Mem. Soc. Astron. Italiana, 80, 422

Bertin, E. & Arnouts, S. 1996, A&AS, 117, 393

Binggeli, B., Sandage, A., & Tarenghi, M. 1984, AJ, 89, 64

Blandford, R. D., Saust, A. B., Brainerd, T. G., & Villumsen, J. V. 1991, MNRAS, 251, 600

Brainerd, T. G., Blandford, R. D., & Smail, I. 1996, ApJ, 466, 623

Bridle, S., Balan, S. T., Bethge, M., et al. 2010, MNRAS, 405, 2044

Bridle, S. & King, L. 2007, New Journal of Physics, 9, 444

Brown, M. L., Taylor, A. N., Hambly, N. C., & Dye, S. 2002, MNRAS, 333, 501

Bryan, G. L. & Norman, M. L. 1998, ApJ, 495, 80

Bullock, J. S., Kolatt, T. S., Sigad, Y., et al. 2001, MNRAS, 321, 559

Comerford, J. M. & Natarajan, P. 2007, MNRAS, 379, 190

Coupon, J., Ilbert, O., Kilbinger, M., et al. 2009, A&A, 500, 981

de Jong, R. S. & Lacey, C. 2000, ApJ, 545, 781

Dodelson, S. 2003, Modern cosmology, ed. Dodelson, S.

Efstathiou, G., Ellis, R. S., & Peterson, B. A. 1988, MNRAS, 232, 431

Einstein, A. 1915, Sitzungsberichte der Königlich Preußischen Akademie der Wissenschaften (Berlin), Seite 844-847., 844

Eisenstein, D. J. & Hu, W. 1998, ApJ, 496, 605

Erben, T., Schirmer, M., Dietrich, J., et al. 2005, AN, 326, 432

Erben, T., van Waerbeke, L., Mellier, Y., et al. 2000, A&A, 355, 23

Finoguenov, A., Guzzo, L., Hasinger, G., et al. 2007, ApJS, 172, 182

Friedman, A. 1922, Zeitschrift fur Physik, 10, 377

Friedmann, A. 1924, Zeitschrift fur Physik, 21, 326

Golse, G. & Kneib, J. 2002, A&A, 390, 821

Haehnelt, M. G. & Tegmark, M. 1996, MNRAS, 279, 545

Hennawi, J. F. & Spergel, D. N. 2005, ApJ, 624, 59

Hetterscheidt, M., Erben, T., Schneider, P., et al. 2005, A&A, 442, 43

Heymans, C., Van Waerbeke, L., Bacon, D., et al. 2006a, MNRAS, 368, 1323

Heymans, C., Van Waerbeke, L., Bacon, D., et al. 2006b, MNRAS, 368, 1323

Hilbert, S., White, S., Metcalf, R., Hartlap, J., & Schneider, P. 2007, in Bulletin of the American Astronomical Society, Vol. 38, Bulletin of the American Astronomical Society, 941–+

Hirata, C. M. & Seljak, U. 2004, Phys. Rev. D, 70, 063526

Hoekstra, H., Franx, M., & Kuijken, K. 2000, ApJ, 532, 88

Hoekstra, H., Franx, M., Kuijken, K., & Squires, G. 1998, ApJ, 504, 636

Hoekstra, H., Franx, M., Kuijken, K., & Squires, G. 1998, ApJ, 504, 636

Huang, Z., Radovich, M., Grado, A., et al. 2010, A&A in submission

Joachimi, B. & Schneider, P. 2009, A&A, 507, 105

Joye, W. A. & Mandel, E. 2003, in Astronomical Society of the Pacific Conference Series, Vol. 295, Astronomical Data Analysis Software and Systems XII, ed. H. E. Payne, R. I. Jedrzejewski, & R. N. Hook, 489–+

Kaiser, N. 1992, ApJ, 388, 272

Kaiser, N. 1998, ApJ, 498, 26

Kaiser, N., Squires, G., & Broadhurst, T. 1995, ApJ, 449, 460

Kitching, T., Amara, A., Gill, M., et al. 2010, ArXiv e-prints

Kolb, E. W. & Turner, M. S. 1990, The early universe, ed. Kolb, E. W. & Turner, M. S.

Komatsu, E., Smith, K. M., Dunkley, J., et al. 2010, ArXiv e-prints

Kruse, G. & Schneider, P. 1999, MNRAS, 302, 821

Liddle, A. R. & Lyth, D. H. 2000, Cosmological Inflation and Large-Scale Structure, ed. Liddle, A. R. & Lyth, D. H.

Limber, D. N. 1953, ApJ, 117, 134

Luppino, G. A. & Kaiser, N. 1997, ApJ, 475, 20

Marzke, R. O., Geller, M. J., Huchra, J. P., & Corwin, Jr., H. G. 1994a, AJ, 108, 437

Marzke, R. O., Huchra, J. P., & Geller, M. J. 1994b, ApJ, 428, 43

Massey, R., Heymans, C., Bergé, J., et al. 2007a, MNRAS, 376, 13

Massey, R., Heymans, C., Bergé, J., et al. 2007b, MNRAS, 376, 13

Maturi, M., Meneghetti, M., Bartelmann, M., Dolag, K., & Moscardini, L. 2005, A&A, 442, 851

Maturi, M., Schirmer, M., Meneghetti, M., Bartelmann, M., & Moscardini, L. 2007, A&A, 462, 473

Meneghetti, M., Melchior, P., Grazian, A., et al. 2008, A&A, 482, 403

Merten, J., Cacciato, M., Meneghetti, M., Mignone, C., & Bartelmann, M. 2009, A&A, 500, 681

Mink, D. J. 2002, in Astronomical Society of the Pacific Conference Series, Vol. 281, Astronomical Data Analysis Software and Systems XI, ed. D. A. Bohlender, D. Durand, & T. H. Handley, 169–+

Miralda-Escude, J. 1991a, ApJ, 370, 1

Miralda-Escude, J. 1991b, ApJ, 380, 1

Monet, D. G., Levine, S. E., Canzian, B., et al. 2003, AJ, 125, 984

Navarro, J. F., Frenk, C. S., & White, S. D. M. 1997, ApJ, 490, 493

Pacaud, F., Pierre, M., Adami, C., et al. 2007, MNRAS, 382, 1289

Pace, F., Maturi, M., Meneghetti, M., et al. 2007, A&A, 471, 731

Padmanabhan, N., Seljak, U., & Pen, U. L. 2003, New Astronomy, 8, 581

Padmanabhan, T. 1993, Structure Formation in the Universe, ed. Padmanabhan, T.

Peacock, J. A. 1999, Cosmological Physics, ed. Peacock, J. A.

Peebles, P. J. E. 1993, Principles of physical cosmology, ed. Peebles, P. J. E.

Pierre, M., Pacaud, F., Duc, P., et al. 2006, MNRAS, 372, 591

Press, W. H. & Schechter, P. 1974, ApJ, 187, 425

Radovich, M., Puddu, E., Romano, A., Grado, A., & Getman, F. 2008, A&A, 487, 55

Rybicki, G. B. & Press, W. H. 1992, ApJ, 398, 169

Sandage, A., Freeman, K. C., & Stokes, N. R. 1970, ApJ, 160, 831

Schechter, P. 1976, ApJ, 203, 297

Schechter, P. L., Bailyn, C. D., Barr, R., et al. 1997, ApJ, 475, L85+

Schirmer, M. 2004, PhD thesis, Univ. of Bonn.

Schirmer, M., Erben, T., Schneider, P., Wolf, C., & Meisenheimer, K. 2004, A&A, 420, 75

Schneider, P. 1996, MNRAS, 283, 837

Schneider, P. & Bartelmann, M. 1997, MNRAS, 286, 696

Schneider, P., van Waerbeke, L., Jain, B., & Kruse, G. 1998, MNRAS, 296, 873

Schrabback, T., Hartlap, J., Joachimi, B., et al. 2010, A&A, 516, 63

Seitz, C. & Schneider, P. 1997, A&A, 318, 687

Skrutskie, M. F., Cutri, R. M., Stiening, R., et al. 2006, AJ, 131, 1163

Smail, I., Hogg, D. W., Yan, L., & Cohen, J. G. 1995, ApJ, 449, L105+

Smith, R. E., Peacock, J. A., Jenkins, A., et al. 2003, MNRAS, 341, 1311

Springel, V., White, S. D. M., Jenkins, A., et al. 2005, Nature, 435, 629

Tyson, J. A. & Seitzer, P. 1988, ApJ, 335, 552

Valtchanov, I., Pierre, M., Willis, J., et al. 2004, A&A, 423, 75

Weinberg, N. N. & Kamionkowski, M. 2002, MNRAS, 337, 1269

Wells, D. C., Greisen, E. W., & Harten, R. H. 1981, A&AS, 44, 363

Wiener, N. 1949, Wiley, New York

Wright, C. O. & Brainerd, T. G. 2000, ApJ, 534, 34

Zaroubi, S., Hoffman, Y., Fisher, K. B., & Lahav, O. 1995, ApJ, 449, 446